UNIVERSITY OF SOUTHAMPTON

FACULTY OF PHYSICAL SCIENCE AND ENGINEERING

Electronics and Computer Science

Nano Research Group

A MEMS Sensor For Stiffness Change Sensing Applications Based on Three Weakly Coupled Resonators

by

Chun Zhao

Thesis for the degree of Doctor of Philosophy

January 2016

UNIVERSITY OF SOUTHAMPTON

ABSTRACT

FACULTY OF PHYSICAL SCIENCE AND ENGINEERING
Electronics and Computer Science

Doctor of Philosophy

A MEMS SENSOR FOR STIFFNESS CHANGE SENSING APPLICATIONS BASED ON THREE WEAKLY COUPLED RESONATORS

by Chun Zhao

Micro-electro-mechanical (MEM) resonator devices have been widely used to sense small changes in the properties of the resonator, namely the stiffness and mass of the resonator. Among these, sensing devices that detect stiffness change have been employed for many applications, including accelerometers, strain sensors, pressure sensors and force gradient sensors for imaging microscopy. In recent years, a new sensing approach, which utilises 2 degree-of-feedom (DoF) weakly coupled resonators has been proposed. By measuring the mode shape changes instead of the frequency shifts, it has been shown that this type of sensing devices has: 1) orders of magnitude higher sensitivity than conventional single DoF resonator sensors; 2) common mode rejection capabilities.

This thesis introduces a novel structure, based on three weakly coupled resonators (i.e. a 3DoF system), in which the stiffness of the resonator in the middle is at least twice the value compared to the other two identical resonators. The device is intended for sensing a change in stiffness. With the 3DoF resonator sensing device, another order of magnitude improvement in the stiffness sensitivity could be demonstrated.

In addition to the novel 3DoF coupled resonator structure, we have also investigated a few practical aspects of the coupled resonator sensing devices that have not been addressed in previous research. These aspects include the damping, dynamic range, nonlinearity and output metrics of the sensor. We have also found a trade-off between the sensitivity and the dynamic range. To solve this dilemma, a bias operation point has also been proposed. By using the bias operation point, it was shown in theory that the linearity of the sensors can also be improved.

Finally, we have also theoretically estimated the vibrational amplitudes and phase delays of each individual resonators within the 3DoF system at the out-of-phase mode frequency. Furthermore, based on these estimations, we have proposed a feasible self-oscillating loop structure, which has the capability of automatically locking to the out-of-phase mode frequency.

Contents

List of Figures

List of Tables

Declaration of Authorship

I, Chun Zhao , declare that the thesis entitled *A MEMS Sensor For Stiffness Change Sensing Applications Based on Three Weakly Coupled Resonators* and the work presented in the thesis are both my own, and have been generated by me as the result of my own original research. I confirm that:

- this work was done wholly or mainly while in candidature for a research degree at this University;
- where any part of this thesis has previously been submitted for a degree or any other qualification at this University or any other institution, this has been clearly stated;
- where I have consulted the published work of others, this is always clearly attributed;
- where I have quoted from the work of others, the source is always given. With the exception of such quotations, this thesis is entirely my own work;
- I have acknowledged all main sources of help;
- where the thesis is based on work done by myself jointly with others, I have made clear exactly what was done by others and what I have contributed myself;
- parts of this work have been published as: [1], [2], [3], [4], [5], [6]

Signed:.....

Date:.....

Acknowledgements

First and foremost I would like to thank my supervisor Professor Michael Kraft. It has been a great honour to work with and learn from you. You have always been the excellent example for me to follow as a successful researcher: creative, dedicated and hard-working, but not lacking the sense of humour. I appreciate all the freedom for research you have given me during my pursuit of PhD at University of Southampton. Also, I am grateful for all your contributions of ideas and time in the project. I will never forget you!

I would also like to express my heartfelt thanks the other members of project. Graham Wood, I couldn't imagine what my PhD would be like without your microfabrication expertise, the constructive discussions or the tea/pizza breaks with you. Dr. Suan Hui Pu, I am lucky to have you as my second advisor, always thoughtful and insightful when it comes to technical discussions. Dr. Harold Chong, a true advisor and friend. You have always been supportive for me during my time at Nano Research Group.The others who have also contributed immensely to my research: Dr. Jianbing Xie, Dr. Honglong Chang, Chirenjeevi Krishnan, Dr. Kian S Kiang, Dr. Ioannis Zeimpekis, Dr. Ibrahim Sari, thank you all very much for the help in micro fabrication. I would also like to thank Dr Matt Himsworth for the suggestions on how to build a customized vacuum chamber. I also want to thank Delphine Cerica for the time reading my thesis and pointing out errors.

In addition, my time at Southampton was made more enjoyable thanks to my many friends. First of all, I would like to appreciate the faithful companion of mine, Jiaoyue Chen, you are the sunshine, my only sunshine; I would also like to pay tribute to my dearest friends and room mates in Southampton: Dr. Chaotan Sima, Dr. Jin Yao, Jingyu Zhang, Li Shen, Lingquan Zhou, Meng Tian, Shuojin Hang, , Sheng Ye, Wei Wang and Yangzi Guo, thank you all for the happy times together! My thanks also go to my good team mates in our football team "Southampton Common United". Thank you all for the good games on the football pitch.

Lastly, I would like to thank all my family. I can never thank enough my parents who have given me everything, for their love, support and encouragement in everything I do. I would also like to thank them for raising me with a love of science and technology, which leads me to a pursuit of the PhD. For all my grand parents, for your love you have given me since I was born. Thank you!

Chapter 1

Introduction

1.1 Motivation of research

Micro-Electro-Mechanical-Systems, MEMS, has attracted a lot of attention in recent years. Due to the increased miniaturization and the improved performance, comparing to conventional macroscopic systems, the use of MEMS devices have been extended from aerospace applications to everyday use (e.g. smart phones). The research interest in micro-mechanical resonant devices, among all MEMS devices, have been steadily increasing since the introduction of the first resonant gate transistor [7], due to their tunability [7], high Q-factor [8], as well as stability against temperature [9] and ageing [10].

Today, applications of the MEMS resonators span across a wide range of areas, including electronic signal filters [11, 12] and oscillators [13]. In addition to these, MEMS resonators have also been widely used in sensing applications, detecting mass and stiffness change [14]. For the purpose of mass detection, much research has been done [15, 16, 17, 18]. Stiffness change sensors have been developed for various applications, such as strain sensing [19, 20, 21], pressure monitoring [22, 23, 24], and the most widely used atomic force microscopy (AFM) [25, 26, 27]. In addition to these, stiffness change sensors have also been used to detect small forces, and some applications are magnetic field sensing (detecting weak Lorentz force) [28, 29], accelerometers (detecting inertial force) [30, 31], charge detection (electrostatic force) [32, 33] Due to the wide range of applications, the application for this research is set to be stiffness change sensing and thus force sensing.

However, the majority of research adopt a single Degree-of-freedom (DoF) resonator structure. Although it has been demonstrated that 1DoF resonator devices suit well with the aforementioned applications, they offer little flexibility [34]. As an example, for some communication applications, a two order response is not sufficient; instead,

higher order bandpass filters are usually more adequate due to their flatter passband, sharper rolloffs, as well as higher stopband rejections [35]. Therefore, a structure of a few resonators coupled together has been proposed accordingly. In recent years, coupled resonators have also gained research interest in sensing applications [36, 37, 38, 39, 40]. The common mode rejection ability [41] makes these sensors attractive. In addition, among these works, 2DoF resonator sensors [36, 39] utilizing a mode localization effect [42] have been demonstrated to be two orders of magnitude more sensitive than 1DoF resonator sensor with frequency shift as output.

It is worth noting that all these sensors mentioned above utilize identical resonators. It is evident that adding one more resonator to a single resonator sensor can improve the sensitivity. Attempts have also been made to couple more identical resonators together to achieve an enhanced sensitivity, namely 15 resonators [43]. But the improvement in sensitivity has only been another order of magnitude, indicating that adding a further 13 identical resonators is less effective than adding the first resonator. Hence, a more effective way of improving sensitivity is required.

In addition, there is no systematic investigation of the different output metrics and the choice of the output signal. Several different output metrics have been used in previous research, including eigenstate shift [36, 39], fundamental mode frequency shift [37, 40] and quotient of amplitudes of one mode to that of the same resonator of another mode [38]. There is also no comparison between different output metrics in terms of, for instance, sensitivity and linear range. Therefore, an optimum output for this type of sensor is necessary.

Furthermore, as one of the most important parameters to determine the vibrating behaviour of a resonator, damping is usually neglected in the theoretical analysis of a 2DOF resonating sensor. Although it is known from 1DoF resonator sensor theory that damping can affect the sensitivity [44], resolution [45] and long term stability [46] of a resonator sensor, the effect on a coupled resonator sensor is still unknown.

Another perspective that is lacking in the literature is the response of the sensor in a wider span of inputs. Currently, researchers have only focused on the response of the sensor around a random starting point [39]. With the full image of the output response of the sensor, we will be able to analyze the dynamic range and nonlinearity specification, in addition to obtain a more rational choice of bias point.

For coupled resonator sensors, these areas that have not been exploited previously require detailed theoretical insight. This motivates our research in a novel theoretical perspective of the coupled resonator sensors. Therefore, the purpose of this thesis is set to establish the theoretical foundations for future research utilising the 3DoF resonator system as an ultrasensitive sensor. To achieve this, we have proposed a analytical model based on transfer functions. From our theoretical analysis of a 3DoF resonator system using this model, we are able to solve the aforementioned problems by proposing a

novel structure. To verify the theoretical model, we have designed and fabricated proof-of-concept devices. Despite the fact that some attention has been paid to the design rationale of the proof-of-concept devices, namely the resonator structure, sensing and actuation transduction, nonlinearity and parasitic capacitance, the selection of dimensions of the devices is not optimized. Future work should focus on the optimization of the sensors for certain specifications and applications.

1.2 Objectives

Considering the current status of research in this field, the objectives of this research is listed below:

- Find an effective way to improve the sensitivity of coupled resonator sensors based on mode localization effect (mode-localized sensors);
- Examine the quantitative effect of damping in mode-localized sensors;
- Investigate the specifications of mode-localized sensors apart from sensitivity, such as dynamic range, linearity and noise;
- Compare different output signals of mode-localized sensors in terms of sensitivity, linearity and implementation complexity;
- Propose a self-oscillating loop structure for mode-localized sensors that is capable of locking to the mode frequency of interest.

1.3 Novelties

The novelties of this research is as follows:

- In this work, we have mainly proposed a novel structure of a resonator sensing device, which consists of three resonators, weakly coupled through electrostatic coupling to its neighbouring resonator(s), that can improve the sensitivity of stiffness change or tensile force by orders of magnitude.

  Currently, the majority of the resonator sensors are single DoF resonator utilizing frequency shift as an output signal, and 2DoF weakly coupled resonator devices adopting a mode-localized sensing scheme. Hence, a 3DoF is a novel structure itself, due to the enhancement in sensitivity. However, among the few 3DoF weakly coupled resonator sensors, the other's work used three identical resonators, and the improvement in sensitivity is limited. Our novel structure proposed in this research

utilizes two identical resonators on either side, and the resonator in the middle has a higher stiffness, typically at least two times higher than the other identical resonators. It has been shown by the theoretical analysis that this structure can improve the sensitivity even further, when compared to the 3DoF structures with three identical resonators.

- In addition to the novel structures, we have utilized the transfer function model, in conjunction with algebraic method to analyse a coupled resonator system for the first time. The two methods complements each other well: algebraic method provides the solutions of mode frequencies and mode localization for systems without any damping; whereas transfer function method helps describe the modal amplitude behaviour with damping, but need to inherit the mode frequencies solved for the case without damping. This approach helped us to achieve more novelties.

- It helps the understanding the effect of damping on mode-localized sensors, that is, the damping adds more nonlinearity to the amplitude ratio. Moreover, by using this approach, we have analysed the modal amplitude behaviour of the 3DoF weakly coupled resonator system in a wider span of stiffness perturbations. This led us to the understanding of the nonlinearity of the amplitude ratio in a wider span, as well as the dynamic range of the sensor, for the first time.

- As a consequence of using this approach based on transfer function model, we were also able to analyse the mechanical noise of the amplitude ratio using the transfer functions for the first time.

- It makes solving the amplitudes of three resonators possible, which then facilitates us to compare different output metrics, namely amplitude ratio, eigenstate shift and amplitude difference, as well as the mode frequency shift for the first time. Further, we have proposed the amplitude ratio as the optimum output metrics, in terms of linear sensitivity and linearity.

- Based on the transfer function model of the 3DoF coupled resonator system, we were able to propose a structure of self oscillating loop first time, which has been demonstrated to be feasible by circuit simulations.

1.4 Publications

Parts of the work presented in this thesis is either based on or to some extent related to the following list of publications that appear as peer-reviewed journal articles or proceedings of international conferences:

- *C. Zhao*, G. S. Wood, J. Xie, H. Chang, S. H. Pu, and M. Kraft, "A force sensor based on three weakly coupled resonators with ultrahigh sensitivity," Sensors and Actuators A: Physical, vol. 232, pp. 151-162, 2015;
- *C. Zhao*, G. Wood, J. Xie, H. Chang, S. Pu, and M. Kraft, "A three degree-of-freedom weakly coupled resonator sensor with enhanced stiffness sensitivity," Microelectromechanical Systems, Journal of, vol. PP, no. 99, pp. 1-14, 2015;
- *C. Zhao*, G. S. Wood, S. H. Pu, and M. Kraft, "Design of an ultra-sensitive MEMS force sensor utilizing mode localization in weakly coupled resonators," in 23$^{\text{rd}}$ Micromechanics and Microsystems Europe Workshop, 2012;
- *C. Zhao*, G. S. Wood, J. B. Xie, H. L. Chang, S. H. Pu, H. M. H. Chong, and M. Kraft, "A sensor for stiffness change sensing based on three weakly coupled resonators with enhanced sensitivity," in Micro Electro Mechanical Systems, 2015, 28$^{\text{th}}$ IEEE International Conference on, 2015;
- *C. Zhao*, G. S. Wood, J. B. Xie, H. L. Chang, S. H. Pu, , and M. Kraft, "Comparative study of different output metrics for a three weakly coupled resonator sensor," in Solid-State Sensors, Actuators and Microsystems, Transducers 2015, 18$^{\text{th}}$ International Conference on, 2015;
- *C. Zhao*, G. S. Wood, S. H. Pu, and M. Kraft, "A feasibility study for a self-oscillating loop for a three degree-of-freedom coupled mems resonator force sensor," Procedia Engineering, vol. 120, pp. 887-891, 2015 (29$^{\text{th}}$ Eurosensors, 2015).

1.5 Organization

This report is organized as follows:

Chapter 2 reviews the current MEMS resonators, in terms of resonator sensor architecture, resonator types, actuation and sensing technologies, as well as some unwanted factors of the resonators.

Chapter 3 look into the theoretical fundamentals of this work, including the basics of the dynamics of the MEMS resonator, capacitive actuator and sensing and the modelling of the MEMS resonators. These will be used in later research.

Chapter 4 analyses the vibrational behaviour of a three degree of freedom resonator, including the mode frequencies and mode shape changes (i.e. amplitude ratio). The theoretical results are verified with simulations of both electrical circuit equivalent of a 3 DOF resonator and finite element modelling.

Chapter 5 discusses the practical aspects of the 3DoF resonator sensors, such as non-linearity, dynamic range, output metrics and noise floor. In addition, a bias operation point is also proposed in this chapter.

Chapter 6 shows the experimental results from two microfabricated proof-of-concept devices. The experimental results generally agreed well with the theoretical predictions.

Chapter 7 proposes a feasible self-oscillating loop structure. The structure was verified by electrical circuit simulations.

Chapter 8 concludes the thesis and outlooks the future work of the research.

Chapter 2

Literature Review

2.1 Introduction to resonator sensors

A resonator is a device or system that vibrates with higher amplitudes at certain frequencies, i.e. fundamental mode frequencies, than the adjacent frequencies. The resonance frequency of a single resonator is directly determined by the physical properties of the resonator, e.g. stiffness and mass [14]. Therefore, when an external stimulus changes one of the properties of the resonator, the fundamental mode frequency of the resonator changes, making resonators attractive transducers for mass sensing. This is demonstrated in Figure 2.1.

Therefore, to measure the quantity of an external stimulus, one intuitive way is to observe the change in the fundamental frequency. One advantage of this approach is the quasi-digital output, thus minimizing the inaccuracies arising from generating an analog output and saving the effort of conversion to digital form [46]. This approach has been used in many applications, including AFM [27, 49], magnetic field sensing [28, 29] and mass sensing [47, 50].

An alternative amplitude-modulation approach to measure the quantity of an external perturbation was proposed in [44]. With this approach, a MEMS resonator sensor is excited at a fixed frequency ω_d near the resonant frequency ω_0 with a fixed amplitude, as shown in Figure 2.2. When the perturbation is for example stiffness, the resonant frequency shifts accordingly as described previously. Therefore, at the fixed driving frequency in vicinity to the resonant frequency, the amplitude response of the resonator changes a value of ΔA, as demonstrated in Figure 2.2.

Compared to a frequency shift as output signal, amplitude change has improved sensitivity given a high Q-factor. Since the sensitivity increases as the Q-factor gets larger, it appears to be more beneficial in terms of sensitivity for such sensors to maximize the Q-factor [27].

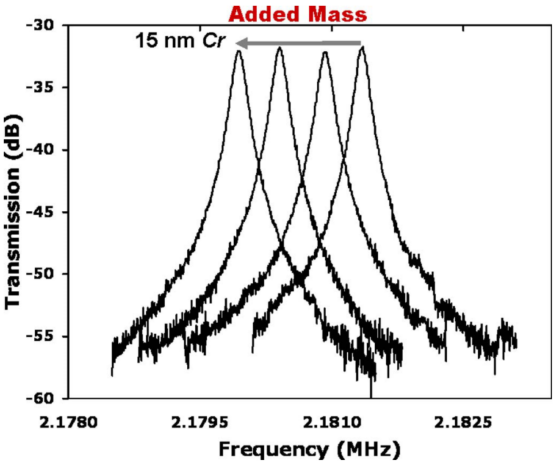

(a)

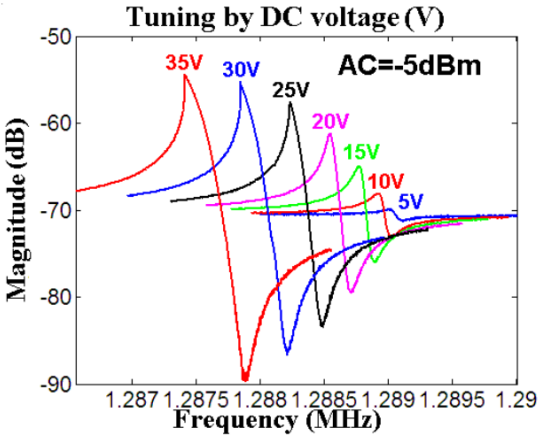

(b)

Figure 2.1: Demonstration of frequency shift: a) after the effective mass of the resonator changes due to the mass loading [47]; b) after the effective stiffness of the resonator changes due to change of DC voltage thus electrostatic spring stiffness [48].

However, high Q means longer time for the sensor to settle, as the time constant of the sensor is given by $\tau_s = 2Q/\omega_0$ [27]. Therefore, high Q-factor limits the bandwidth of the sensor. Another disadvantage of this sensor is that the slope of amplitude against frequency is not a constant, as the resonance frequency shifts further away from the point with maximum sensitivity, the sensitivity changes [51], consequently adding burdens to the calibration process.

Due to the high sensitivity, this approach has been employed in various works, especially in force microscopy applications, where sensitivity is more important and the disadvantages are not the main issues [44, 51, 52, 53].

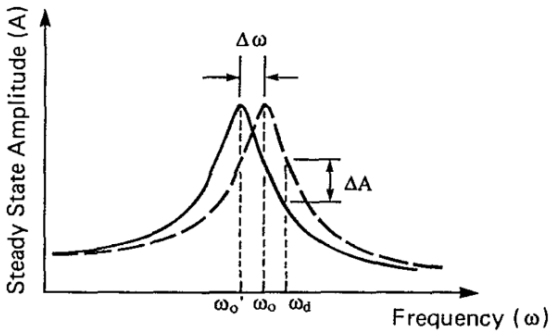

Figure 2.2: Demonstration of amplitude-modulation approach in a single resonator [27]. The drive signal is generated at a frequency of ω_d next to fundamental mode frequency ω_0. After a perturbation is introduced shifting the frequency to ω_0', the amplitude at drive frequency changes by ΔA.

2.2 Coupled resonator sensors

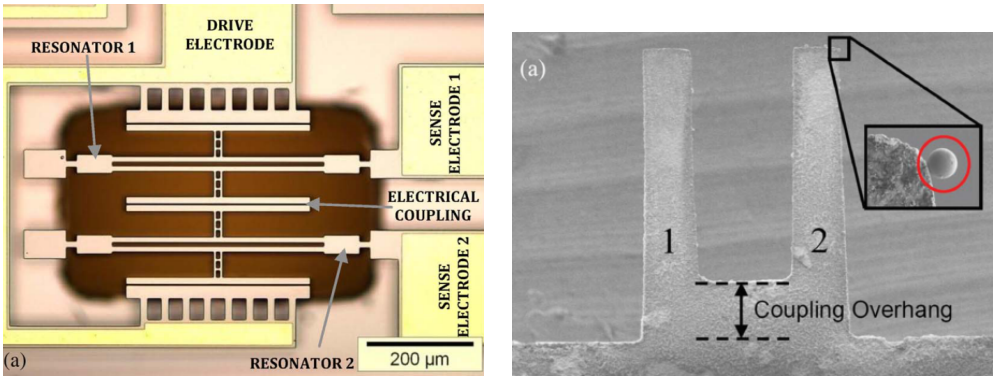

(a) (b)

Figure 2.3: Demonstration of coupled resonator sensors: a) with electrostatic coupling [39]; b) with mechanical coupling [36].

As the research and development of MEMS resonator sensors matures, the majority of sensors consist of only one resonator. In order to identify multiple analytes in certain applications [54, 55], an array of resonators is needed. With single DoF resonator, it requires a large number of connections to detect the motion of each resonator in the array [56]. To solve these potential problems, a new type of resonant sensors, where multiple resonators are coupled together through coupling, as shown in Figure 2.3, has been proposed [56, 57, 58]. This is useful for emerging biomedical applications such as chemical substances labelling [54] and DNA hybridization [59].

2.2.1 Sensitivity improvement

To compare the sensitivity, we use normalized sensitivity [60] as a figure of merit (FOM). If we define the normalized sensitivity with respect to the stiffness change of 1DoF

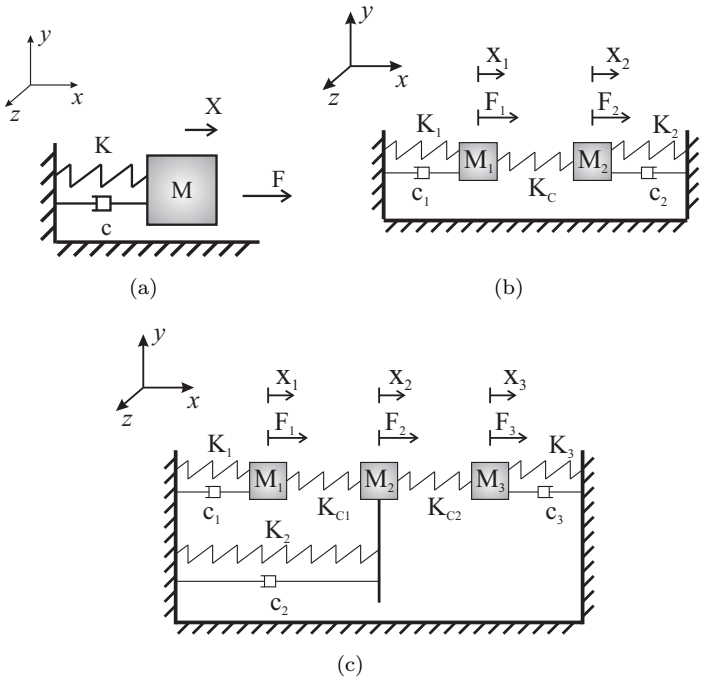

Figure 2.4: Demonstration of lumped element model of 1DoF, 2DoF and 3DoF resonators: a) 1DoF, b) 2DoF and c) 3DoF.

(Figure 2.4(a)), 2DoF (Figure 2.4(b)) and 3DoF (Figure 2.4(c)) as $\mathcal{S}_{1DoF}$, $\mathcal{S}_{2DoF}$ and $\mathcal{S}_{3DoF}$, respectively, the mathematical definitions are given below:

$$\mathcal{S}_{1DoF} = \frac{\text{Normalized output}_{\text{1DoF}}}{\Delta K/K} \tag{2.1}$$

$$\mathcal{S}_{2DoF} = \frac{\text{Normalized output}_{\text{2DoF}}}{\Delta K/K} \tag{2.2}$$

$$\mathcal{S}_{3DoF} = \frac{\text{Normalized output}_{\text{3DoF}}}{\Delta K/K} \tag{2.3}$$

Where ΔK and K denote change in stiffness and stiffness of the resonator, respectively.

Typically, for a 1DoF resonant sensor with a frequency shift, $\Delta\omega$, as an output signal, the normalized output is expressed as $\Delta\omega/\omega$, where ω is the fundamental resonant frequency. In the literature, it has been shown that the normalized sensitivity of 1DoF resonator $\mathcal{S}_{1DoF} \approx 1/2$ [61], assuming small stiffness change ($\Delta K \ll K$).

Among the coupled resonator sensors, one novel method that monitors the vibration amplitude change of the resonators is particularly interesting [36, 38, 39]. These sensors take advantage of a *mode localization* effect that was first predicted by Anderson's pioneering work [42]. When the theory of mode localization was first introduced, it inspired many works in the field of solid-state physics, consequently winning Anderson the Nobel prize in Physics in 1977. Later research [62] demonstrated that when a balance in a

weakly coupled vibrating structure was broken by an external perturbation, the mode shape changed accordingly. Despite of these important discoveries, it was only until recently was the theory applied to MEMS sensing applications.

By measuring the effect of mode localization in a 2DoF weakly coupled resonator system subject to external stimulus, the quantity of the stimulus can be sensed [36, 39]. It is also evident that the weaker the coupling strength compared to the stiffness of each resonator, the stronger mode localization can be observed [39]. The typical output signal of this type of coupled resonator sensor (mode-localized sensor) is the shift in eigenstate or eigenvector, Δu. The normalized output is therefore $\Delta u/u$, where u is the initial eigenstate. It has also been shown that, compared to conventional 1DoF resonator sensor with frequency shift as an output, $\mathcal{S}_{2DoF}$ is two to three orders of magnitude higher than $\mathcal{S}_{1DoF}$, hence, two to three orders of magnitude enhancement in sensitivity can be achieved [36, 39], makes it an alternative approach to improve the sensitivity.

To attenuate the energy propagation from one side of the chain to the other, it is natural to insert more energy-storing resonators in between the two identical resonators to increase the insertion loss. In this way, the sensitivity can be further improved compared to a 2DoF resonator system. One study introduced a total of 15 identical resonators [43], and the resulting sensitivity improvement is two to three orders of magnitude compared to that of a 2DoF resonator system. However, 15 identical resonators take a large chip area compared to a smaller number of resonators. Hence, it is imperative to find a more efficient way of improving the sensitivity even further, without adding too many resonators to increase the chip size. This leads to the main focus of this research.

As will be shown in later chapters, a 3DoF mode-localized resonant sensor will be reported in this thesis. The normalized output is an amplitude ratio, X_1/X_3, where X_1 and X_3 are the vibration amplitude of resonator 1 and 3, respectively. Through analytical calculations, we can derive:

$$\mathcal{S}_{3DoF} = \frac{X_1/X_3}{\Delta K/K} = \pm\gamma_3 \tag{2.4}$$

Where the positive or negative sign depending on the sign of ΔK and also mode of interest. Therefore, γ_3 *is the absolute value of normalized sensitivity with respect to normalized stiffness change for a 3DoF mode-localized sensor reported in this thesis.* In addition, since $\mathcal{S}_{1DoF} \approx 1/2$, fundamental mathematics can show that $2 \times \gamma_3$ are the sensitivity improvement of 3DoF mode-localized sensors when compared to 1DoF resonant sensor. For these reasons, γ_3 *is the most important parameter in this thesis.* The higher γ_3 value indicates a higher sensitivity of the 3DoF resonant sensor, and also a higher sensitivity improvement compared to the 1DoF counterpart.

2.2.2 Coupling

Structure-wise, to couple the resonators, one method is through the mechanical structure [35, 36, 56]. Although mechanical coupling is simple to implement, it has one disadvantage that it cannot be adjusted once fabricated. To solve this problem, another viable approach is electrostatic coupling spring [63], where the electrostatic spring constant can be easily adjusted by changing the coupling voltage, making the sensor more flexible.

2.2.3 Output metrics

As for the output metrics for these sensors, eigenstates shift has been employed [36, 39]. To calculate the eigenstate shift, according to [34], it is required to normalize the eigenstates from the measured amplitudes to unity magnitude, followed by subtraction of the initial eigenstates from the vector just calculated. This is a complicated mathematical calculation, hence, making the data processing hardware and software difficult to implement. However, it is still an innovative approach, which improves the sensitivity and common mode rejection ability compared to mode frequency shift as an output signal. It has been demonstrated that the sensitivity of the sensor to ambient conditions such as pressure and temperature is not as significant as that to single sided stimulus [36, 41]. Other researchers [38] employed the vibration amplitude quotient of one resonator at two different mode frequencies. This approach is novel in the sense that it only requires to measure the amplitude of one resonator. However, for this approach, it is necessary to find both resonant frequencies, which is more time consuming than finding only one resonant frequency for approaches such as eigenstate shift or frequency shift. It should be noticed that, the quasi-digital nature, as well as the high resolution of frequency signal makes it useful in some systems [37]. However, the moderate sensitivity compared to eigenstate shift or amplitude ratios at separate modes is one disadvantage for mode frequency shift as an output signal. Up to date, there is no systematic investigation of the advantages or disadvantages of particular output metrics, in terms of specification such as linear range. Hence, for this emerging technology of coupled resonator sensors, it is imperative to find a suitable output in order to optimize the performance. Also, for a particular type of output, there is little research on the dynamic range.

2.2.4 Damping

As for damping, Rayleigh's damping in particular, the effect on coupled resonator has been analyzed in [34]. It was shown in theory that the damping would have phase differences compared to the undamped system, but the impact on sensitivity is insignificant. However, no quantitative study of the effect of damping has been done so far. Without the quantitative study of the damping effect, it is difficult to optimize the damping of the sensor to achieve an optimized performance.

2.2.5 Other issues

Apart from these issues that need to be addressed, as a new technology, there are other shortcomings of coupled resonator sensors that need to be improved in the future. One obvious disadvantage is that the majority of this type of sensors up to date was operating in vacuum in order to improve the sensitivity of the device. The reason is that the operating mode frequencies are closer to each other as the coupling strength between the resonators decreases [34]. To distinguish the operating mode frequency, the anti-aliasing rule should be satisfied [64]. Because of this, the minimum coupling strength, which means maximum sensitivity for a specific design, is limited by the bandwidth of the mode. Therefore, it is necessary to use vacuum to maximize the sensitivity of the sensor. Another major disadvantages of this type of sensor is that, all the measurement of coupled resonator sensors up to date are not done in real-time, as frequency sweep is required to find the desired resonant mode frequency. On the contrary, self-oscillating loop structure used in single DoF resonator sensors is capable of automatically locking to the fundamental mode [31]. Due to this, the bandwidth of input measurement this type of resonators were not yet investigated. This inability for real-time measurement has become a huge obstacle for implementing coupled resonator sensors in commercial applications.

2.3 Types of resonators

For sensing applications, different types of resonators have been used in the literature to serve for the purpose of maximizing the performance, such as sensitivity. Generally, resonators can be divided into two categories, with or without proof mass.

2.3.1 Resonator with proof mass

Typically this type of resonator consists of a proof mass suspended by compliant beams which act as the springs, as shown in Figure 2.5. Therefore for this type of resonator, the effective mass is dominated by the proof mass. And the suspension beams contribute the most to the effective spring constant, since the proof mass can be regarded as a rigid body. The vibration mode of this type of sensors is usually in-plane flexural mode.

Although not very commonly used in conventional resonators sensors with frequency or amplitude shift, this type of sensors have been successfully employed in the inertia sensing applications, namely for gyroscopes [65, 66, 67, 68, 69]. This is due to the fact that for an angular rate, a larger proof mass gives an increased Coriolis force, and therefore an enhanced sensitivity. This type of sensor has also been used in AFM applications [51].

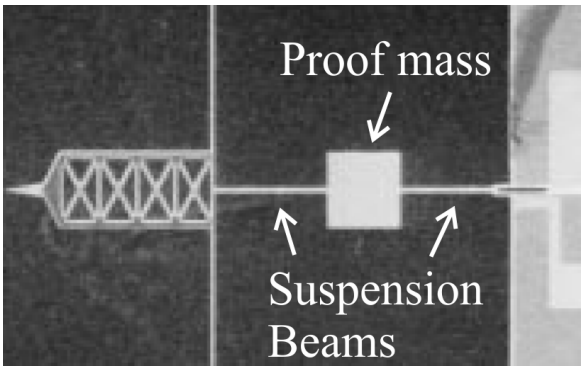

Figure 2.5: Demonstration of a resonator with proof mass [51].

Generally resonators with proof masses have lower fundamental frequency, due to large effective mass value. For identical effective stiffness, a proof mass 100 times larger means 1/10 of the original resonant frequency. Furthermore, the resonance frequency is insensitive to small mass variations. On one hand this particular trait makes this type of resonator less attractive for mass sensing applications; on the other hand, it makes the resonance frequency stable even in presence of small mass variations, for example, during stiffness change monitoring process.

This type of resonators can be easily integrated with capacitive drive [65, 66] and sensing [65, 66], as well as piezoresistive sensing [51].

2.3.2 Resonators without proof mass

A less intuitive design of resonators are vibrating structures without clearly distinguished mass or springs. This type of resonators can be further categorized in terms of vibration modes, such as flexural, lateral and bulk mode. However, despite the fact that lateral [70] and bulk [47, 71] modes have been used for mass and force sensing, and they typically have high Q-factor even in air, generally they have very high frequency (>1MHz), which would complicate interface electronics design. Moreover, lateral resonator sensors [70] require a network analyzer for standing wave measurement, which is not suitable for commercial use. Therefore, in this section, these resonators are not elaborated in detail.

2.3.2.1 Cantilevers

One of the most commonly used resonator types utilizing the flexural mode is the cantilever as shown in Figure 2.6. Due to the simplicity of structure and a wide range of mode frequencies, in addition to relatively small mechanical nonlinearities and high Q-factor, it has been widely used in mass [16, 18, 73, 74] and stiffness change sensing applications, predominantly AFM [25, 26, 27].

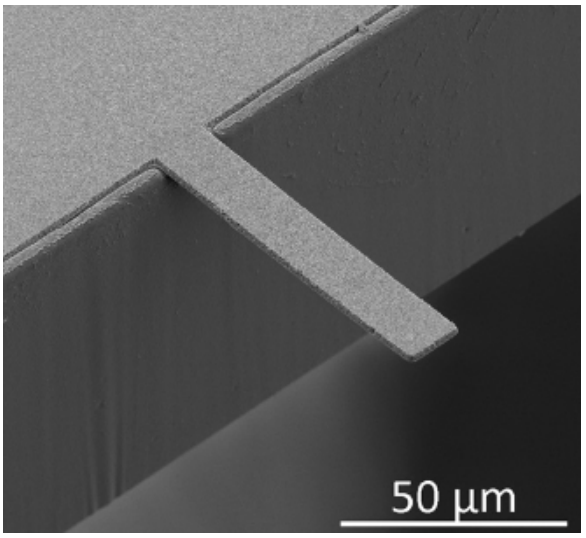

Figure 2.6: Demonstration of a MEMS cantilever resonator [72].

It is worth noting that among the mass sensors, the majority of the sensors utilize the first fundamental mode of the cantilever, while some work also used higher modes [73]. Due to the improved Q-factor and decreased effective mass of the higher modes, the sensor exhibites higher sensitivity.

Typically cantilevers are actuated piezoelectrically [25], and their motions are observed optically [73]. However, the simple structure means that it can also be easily incorporated with many other actuation and sensing techniques, including thermal [75] or capacitive [74] actuation, as well as capacitive [74] and piezoresistive [76] sensing.

2.3.2.2 Fixed-fixed beam

Another widely used structure of resonator for flexural mode is fixed-fixed beam, as shown in Figure 2.7(a). Due to the high longitudinal stiffness, it can provide two orders of magnitude improvement in stability to the large force gradient compared to cantilevers [51]. Therefore, it has been favoured for force sensing applications that require high stability in the presence of large force gradient [79].

Furthermore, another variant of fixed-fixed beam widely used is double-ended tuning fork (DETF), as shown in Figure 2.7(b). Due to the increased balance in vibration, DETFs usually have enhanced Q-factors [46]. It has been used to gauge modulated strain in different applications, including a strain sensor [20], electrometer [78], accelerometer [31] and pressure sensor [80].

Typically fixed-fixed beam resonators have high fundamental mode frequencies and high mechanical nonlinearities, due to a relatively high first order effective stiffness.

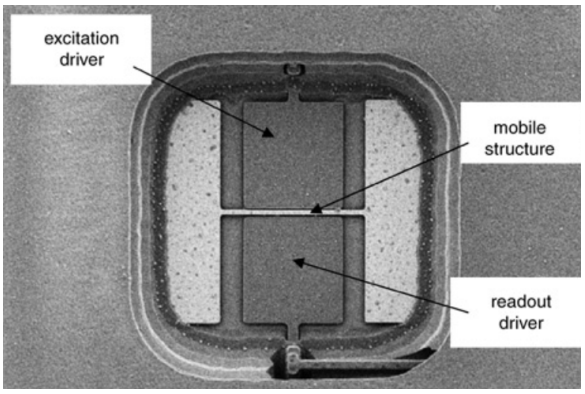

(a)

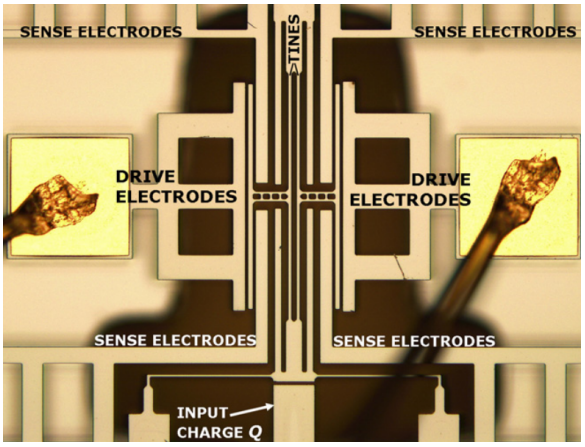

(b)

Figure 2.7: Examples of a MEMS fixed-fixed beam resonators: a) standard fixed-fixed beam [77]; b) a double-ended tuning fork (DETF) [78].

For actuation and motion pick-up, capacitive schemes have been most widely used [20, 78], while piezoresistive detection approach has also been used [19]. In what follows, the choice of actuation and motion pick-up techniques is discussed.

2.4 Transducer technologies

A transducer is a device or structure that transfers energy from one domain to another, e.g. electrical to mechanical domain. As for MEMS resonators, actuating the micro resonators mechanically using electrical energy, as well as detecting the mechanical vibration of the resonators with easy-to-process electronic signals, requires transducers that converts the energy between electrical and mechanical domains. A common type of transducer, the capacitive transducer, is shown in Figure 2.8.

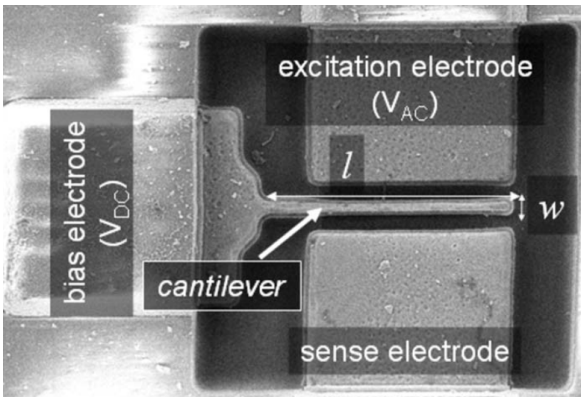

(a)

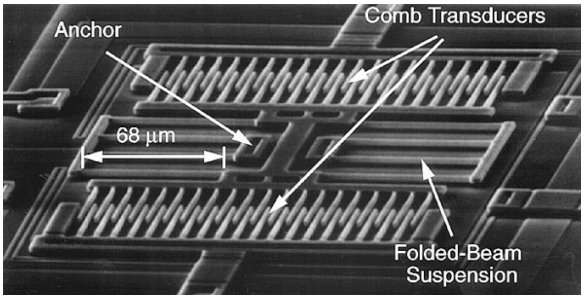

(b)

Figure 2.8: Demonstration of capacitive transducers: (a) parallel plate transducer [74] and (b) comb transducer [81].

2.4.1 Actuation

Due to the small dimensions of MEMS resonators, a large excitation force could break the structure, or take the resonator to strongly non-linear region. Therefore, it is natural to actuate a MEMS resonator with a well controlled weak force, usually converted from another energy domain. The common actuators to drive the resonators include: capacitive, thermal and piezoelectric actuation.

For piezoelectric actuation, an externally applied electric field changes the shape of the piezoelectric material, thereby actuating the resonator in the desired direction. Using piezoelectric approach, it is able to drive the resonators without any DC voltage, thereby providing instantaneous AC forces in response of alternating electric field [82]. This is one distinctive advantage over capacitive method. However, piezoelectric actuation requires extra piezoelectric materials in the device, e.g. AlN [83], thus complicating the fabrication process and adding extra cost. Moreover, large voltages are usually necessary to obtain a sufficient actuation [82].

Thermal actuation is based on the property of a material that is subject to thermal extension or compression when heated or cooled. This approach is easy to implement, only consume low voltages compared to piezoelectric actuation [82]. But the long time constant for heating or cooling in thermal actuation, in the range of μs [84] ultimately

limits the response of the resonators. Because of this, the commercial success of thermal actuation scheme is relatively limited compared to academia research.

Thanks to its simplicity to fabricate without extra materials, capability to integrate with interface electronics systems, and low cost, the most popular method in MEMS devices is capacitive actuation, or electrostatic force actuation. It has the drawbacks such as nonlinear forces, pull-in instability [85] and an AC force could appear at double frequency. However, the performance of a capacitive transduction can normally be optimized, with careful design, the negative effects can be negligible.

There are two ways of implementing capacitive actuation. One is parallel plate, the other is the comb finger (Figure 2.8(a) and Figure 2.8(b)). The plates move in different directions for these two geometries: parallel plates move vertically to the plate, whereas comb fingers move parallel to the plate. Both techniques have been used in various resonator sensing applications, e.g. using parallel plate [31, 78] and comb drives [86]. Although comb fingers are capable of providing the weaker nonlinear force, thus allowing a few time improvement in maximum displacements [87], parallel plate actuators are more favourable in applications where large actuation forces are required for limited device size, due to larger actuation forces provided by parallel plate actuator with an equal volume and capacitor gap [82].

2.4.2 Motion pick-up

Sensing of the mechanical vibration of the resonator using electrical instruments, is essentially the reverse process of energy conversion from electrical to mechanical domain.

Currently, methods to monitor the vibrating motion of resonators, such as piezoelectric [70], optical [73] exist in the literature. However, due to the complexity of construction, it shall not be discussed in this section. The simple-to-implement approaches include capacitive and piezoresistive sensing.

It is known that the dimensions of a structure change due to mechanical stress applied. For a conducting material, the change in dimensions results in a change of electrical resistance. Utilizing this effect, piezoresistors are embedded to the support of resonators to monitor the stress at the support of vibrating resonators where the change of stress is the most significant. The main advantage of piezoresistive sensing is that it doesn't require complex interface circuitry compared to capacitive sensing. Therefore it has been widely used in various resonator applications [51, 76]. However, due to the noisy, temperature dependent nature of resistors, it is not suitable for applications where high resolution and temperature stability is essential.

For capacitive sensing, the basic principle is to measure the change in capacitance due to the displacement of the resonator. Despite of the same problems as capacitive actuation, such as nonlinearity and pull-in instability (see Section 2.5.1), in addition to parasitic capacitances [88], capacitive sensing has been a popular choice to detect the displacement of MEMS resonators [78, 81], because of the improved noise performance, power consumption it offers and its simplicity of implementation [82].

As capacitive actuation, there are two ways of implementing capacitive motion sensing, parallel plate and comb fingers. Figures 2.8(a) and 2.8(b) show micro-fabricated resonators with capacitive pick-up using parallel plate and comb fingers, respectively. Similar to capacitive actuation, parallel plate capacitive motion pick-up has distinctive disadvantages such as nonlinearity compared to comb fingers. However, normally the gap between the plates is one fraction of the overlap length ($\sim 1/10$), assuming the same initial value of capacitance, parallel plates offer higher response (~ 10 times) to the same displacement.

2.5 Nonidealities of MEMS resonator

Practical MEMS resonators have, sometimes undesired, nonidealities associated, such as instabilities [89, 90], nonlinearities [91] and parasitics [92].

2.5.1 Instabilities

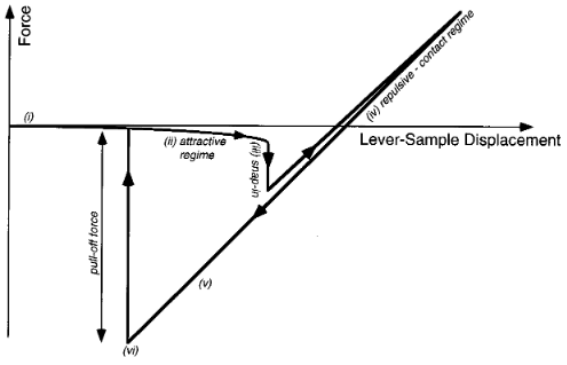

Figure 2.9: The figure shows the lever-sample displacement versus the force between the sample and the cantilever tip [93]. The lever-sample displacement increases as the cantilever gets closer to the sample surface. After an attractive regime for normal force sensing, a "snap-in" or "jump-to-contact" occurs in region (iii) where the force gradient exceeds the spring constant of the cantilever. In this region, the force abruptly changes, due to a sudden change in the distance between the tip and the sample, therefore indicating the tip jumps to contact with the surface.

There is a "jump-to-contact" [89] effect in dynamic AFM applications, where the restoring stiffness of the cantilever is not sufficient to overcome the downward atomic force (Van der Waals force) gradient, the tip jumps to the surface of the sample [93], as shown in Figure 2.9. When this happens, the vibration of the resonator stops, thus the measurement has to be interrupted. This instability also happens in capacitive actuation and sensing, as known as the "pull-in" effect [90].

To avoid the "jump-to-contact" phenomenon, one approach is to change the orientation of the resonator, so that the resonator is vertical to the sample surface rather than the conventional parallel [94]. Using this approach, the force gradient is applied on the longitudinal direction of the vibrating beam. Due to the larger longitudinal stiffness compared to the lateral stiffness, the instability is alleviated [51, 79, 95].

The electrostatic force instability can be circumvented by making sure that the electrostatic force is always smaller than the restoring force of the resonator. To achieve this, it is imperative to keep the DC voltage value smaller than the pull-in voltage, which is given by (for a parallel plate actuator) [7]:

$$V_{\mathrm{PI}} = \sqrt{\frac{8}{27}\frac{K_{\mathrm{eff}} d^3}{\varepsilon_0 A}} \tag{2.5}$$

where K_{eff} is the effective mechanical stiffness, d is the zero voltage gap between parallel plate, A is the area of the plate, ε_0 is the permittivity of free space.

In addition to this, it is essential to ensure that the electrostatic force gradient, which is inversely proportional to $(d-x)^3$ (x being the maximum amplitude), is smaller than the effective mechanical stiffness of the resonator [82]. In this regard, it is also necessary to use small amplitude compared to the spacing d to prevent pull-in.

2.5.2 Nonlinearities

Nonlinearities exist in electrostatically actuated microresonators in two forms, a) mechanical nonlinearity and b) electrostatic nonlinearity [91]. Due to the nature of the nonlinearities, it can also be divided into two groups, a) spring-hardening nonlinearity and b) spring-softening nonlinearity [96], as shown in Figure 2.10. It can be shown that mechanical nonlinearity is typically a spring-hardening nonlinearity, whereas the electrostatic nonlinearity is generally spring-softening [97].

As demonstrated in Figure 2.10, both nonlinearities become more severe as the maximum amplitude increases, and can potentially lead to instabilities in some frequency region. Therefore, the nonlinearities ultimately sets the maximum stable amplitude of the MEMS resonator. This conflicts the desire of high amplitude for higher sensitivity

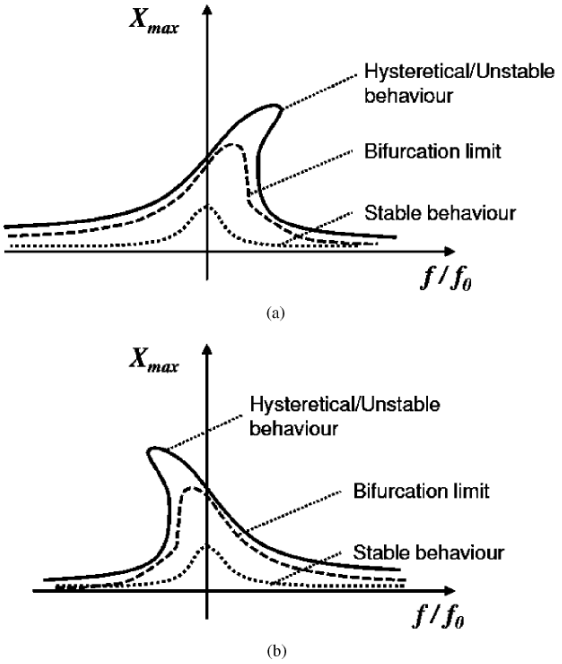

Figure 2.10: The figure shows two types of nonlinearities of MEMS resonators: a) spring-hardening nonlinearity, where the spring is "hardened" as the amplitude increases, thus tilting the resonance peak towards a higher frequency; b) spring-soften nonlinearity, where the spring is "softened" with increasing amplitudes, hence pushing the resonance peak to a lower frequency [96].

for resonator sensor with amplitude change as output. Hence, the nonlinearities should be minimized for some sensing applications.

To reduce the nonlinearity or enhancing the maximum linear amplitude, two approaches have been proposed [96]. One way is to use "L-shaped" beams instead of "I-shaped" beams. It is demonstrated in [96] that the "L-shaped" beams allow more flexibility and stress release at one support, thus improving the maximum linear amplitude compared to "I-shaped" beams. Another viable method is to use appropriate DC voltage, so that the spring-softening nonlinearity introduced by capacitive actuation can cancel out the spring-hardening nonlinearity, thus improving the linearity.

2.6 Parasitics

Electrical characterization of MEMS resonators working at high frequencies becomes increasingly complicated at higher operating frequencies due to the parasitic elements [98]. Without proper control of the parasitics, the electrical signals through the parasitic elements can sometimes dominate the electrical measurements, as shown in Figure 2.11(b).

The most significant of the parasitic elements at lower frequency is the feedthrough capacitance, marked as C_0 in Figure 2.11(a). The sources of the feedthrough capacitance

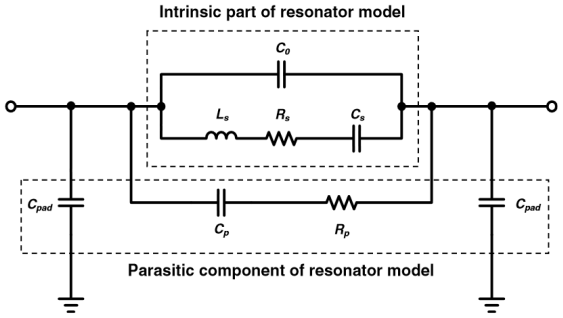

(a)

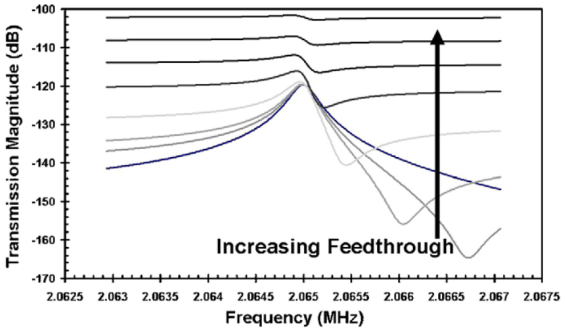

(b)

Figure 2.11: Demonstration of parasitic elements and their effects: (a) Equivalent electrical model of MEMS resonator with parasitic components [92]. and (b) effect of increasing feedthrough capacitance for MEMS resonators, potentially swamping the motion of the resonator [98].

include the capacitance of the capacitive transducer, interconnects and electrical packaging [98]. Therefore, it is impossible to completely eliminate the feedthrough capacitance.

To reduce the effect of the feedthrough capacitance, one method is to decrease the capacitive overlapping area [99]. An alternative method is to compensate the feedthrough current using a capacitor with the same value as the feedthrough capacitance. It was reported that this can be achieved by either using a twin resonator [98] or an unreleased resonator [100]. Another viable method is to measure two sets of data, with and without DC bias [48]. It was demonstrated that the measured admittance of the MEMS resonator can calculated as the admittance with DC bias subtracted from that without DC bias, thus the effect of parasitic feedthrough capacitance can be cancelled.

Apart from the feedthrough capacitance, another parasitic element that is worth noticing is the C_{pad} in Figure 2.11(a). For electrical characterization of the resonator, the output of the resonator is directly connected to a preamplifier. Therefore, the parasitic C_{pad} contributes to the total input capacitance of the amplifier. This in effect lowers the flat band noise gain of the amplifier, hence deteriorates the stability and the maximum bandwidth of a stable preamplifier [101].

2.7 Summary

In this chapter, MEMS resonator sensors are reviewed. The working principles of different types of resonator sensors are also described, including single resonator sensors and coupled resonator sensors. Previous literature have demonstrated that mod-localized coupled resonator sensors are more sensitive than single resonator sensors. In addition, we have shown that γ_3 is the most important parameter for the 3DoF mode-localized sensor in this thesis, as it indicates the normalized sensitivity, as well as the improvement in sensitivity compared to the 1DoF resonant sensors. Further, types of micromechanical resonators, transducer technologies for actuation and sensing of the motion of the resonator, as well as nonidealities of MEMS resonators in sensors in literature are also reviewed. These would provide insight into the design rationale of our resonator sensors.

In Chapter 3, we will cover the fundamental theories of the MEMS resonator sensors, especially the fundamental theory of coupled resonator sensors.

Chapter 3

Fundamental Theory

3.1 MEMS resonator dynamics

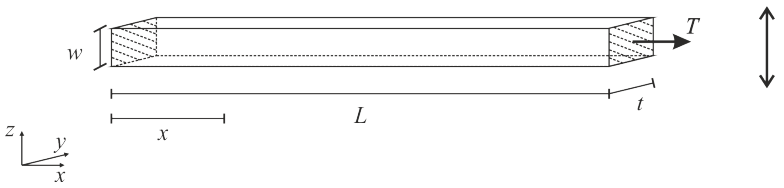

Figure 3.1: Fixed-fixed beam model with parameters

To understand the physics and working principle of a MEMS resonator sensor, we will start with the dynamics of micro-resonators. Among various build of MEMS resonator in the literature discussed in Chapter 2, the most common type is bending beams with uniform rectangular cross-section, shown in Figure 3.1.

The dominant differential equation of motion for a transversally vibrating beam, without external force, is given by [102]:

$$\frac{\partial^2}{\partial x^2}[EI\frac{\partial^2 d(x,t)}{\partial x^2}] + \xi\frac{\partial d(x,t)}{\partial t} + \frac{\partial}{\partial x}[T\frac{\partial d(x,t)}{\partial x}] + \rho A\frac{\partial^2 d(x,t)}{\partial t^2} = 0 \tag{3.1}$$

In Equation 3.1, $d(x)$ is the deflection of the beam at the position of x $(0 \leq x \leq L)$ in the z-axis, E is the young's modulus of the material, ξ is the damping, T is the axial tension applied to the beam (including residual stress), ρ is the density of the material, A is the constant beam cross-sectional area, $A = wt$ in this case, $P(x)$ is the transverse load applied. It is worth noting that I is the moment of inertia of the beam, which is dependant of the direction of vibration. If it is defined that the resonator only moves in the z-axis as shown in Figure 3.1, $I = w^3t/12$.

The solution of Equation 3.1 can be transformed into the form of an equation of motion in the z-axis of an unforced spring-damper-mass system given by [103]:

$$M\frac{\partial^2 z(t)}{\partial t^2} + c\frac{\partial z(t)}{\partial t} + Kz(t) = 0 \tag{3.2}$$

where the equivalent effective mass and spring constant are given by [104]:

$$M_{\text{eff}} = \int_0^L \rho A u^2(x)\mathrm{d}x \tag{3.3a}$$

$$K_{\text{eff}} = \int_0^L EI\left(\frac{\partial^2 u(x)}{\partial x^2}\right)^2 \mathrm{d}x + \int_0^L T\left(\frac{\partial u(x)}{\partial x}\right)^2 \mathrm{d}x \tag{3.3b}$$

Therefore, a beam with transversal vibrations can be modelled as a single DoF spring-damper-mass system.

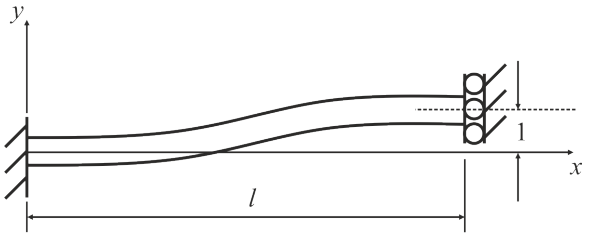

Figure 3.2: Beam with one end fixed and the other end subject to vertical movement.

For a given boundary conditions of two ends of the beam, the mode shape $u(x)$ is a given function [105]. For instance, for a resonator with proof mass (as shown in Figure 2.5), the suspension beam has one end fixed and the other end subject to vertical movement, as shown in Figure 3.2. The fundamental mode shape is given by [105]:

$$u(x) = \frac{3x^2}{L^2} - \frac{2x^3}{L^3}, 0 < x < L \tag{3.4}$$

Substituting Equation 3.4 into Equation 3.3, we are able to obtain the effective mass and spring constant of this type of beam for the fundamental mode:

$$M_{\text{eff}} = 0.371\rho wtL \tag{3.5a}$$

$$K_{\text{eff}} = \frac{Ew^3t}{L^3} + \frac{1.2T}{L} \tag{3.5b}$$

As described in the previous chapter, nonlinearities exist in suspension beams. Taking the nonlinearities into consideration, the equation of motion of a resonator without any force applied becomes [104]:

$$M_{\text{eff}}\frac{\partial^2 z(t)}{\partial t^2} + c_{\text{eff}}\frac{\partial z(t)}{\partial t} + K_{\text{eff}} z(t) + \left(\frac{EA}{2L}\left(\int_0^L \left(\frac{\partial u(x)}{\partial x}\right)^2 \mathrm{d}x\right)^2\right) z^3(t) = 0 \tag{3.6}$$

If we define the third order nonlinear spring constant $K_{\text{eff},3}$ as:

$$K_{\text{eff},3} = \frac{Ewt}{2L}\left(\int_0^L \left(\frac{\partial u(x)}{\partial x}\right)^2 \mathrm{d}x\right)^2 \tag{3.7}$$

For a suspension beam with one end fixed and the other end subject to vertical movement, $K_{\text{eff},3}$ becomes:

$$K_{\text{eff},3} = \frac{0.72Ewt}{L^3} \tag{3.8}$$

With the fundamental mode shapes of cantilevers and fixed-fixed beams given in [82], we are able to calculate the coefficients for the effective mass, spring constant and third order nonlinear spring constant of the three types of beams, as listed in Table 3.1.

Coefficients of	Fixed-fixed beam	Cantilever beam	Suspension beam for resonator with proof mass
Effective mass ($\times \rho wtL$)	0.40	0.25	0.37
Effective spring constant without tension ($\times \frac{Ew^3t}{L^3}$)	198	3	12
Modification of spring constant by tension ($\times \frac{T}{L}$)	4.9	1.2	1.2
Third order nonlinear spring constant ($\times \frac{Ewt}{L^3}$)	11.90	0.68	0.72

Table 3.1: Calculated coefficients for the first resonant mode of different types of beams based on the mode shapes given in [82]

Given the same dimensions of the beam and material, thus Young's modulus, from the table, it can be seen that fixed-fixed beam has the highest effective mass and spring constant, while the cantilever beam has the lowest. If the beams are subject to an identical tensile force, the fixed-fixed beam has the lowest normalized stiffness change, while cantilever beam has the highest.

As for the mechanical nonlinearity, the fixed-fixed beam has the strongest mechanical nonlinearity, whereas cantilever and suspension beam for resonator with proof mass have more than 10 times weaker mechanical nonlinearity than that of the fixed-fixed beam. It was demonstrated that by employing a stress releasing tether, the nonlinearities of a fixed-fixed beam can be reduced [96].

3.2 Capacitive transducer

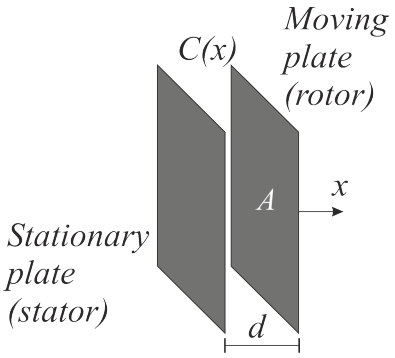

Figure 3.3: Demonstration of parallel plate capacitive transducer.

In Chapter 2, different transduction techniques are discussed and compared. Due to the simplicity of implementation, low cost, as well as low noise and power consumption, capacitive transduction is the choice for our research. For the implementation, we chose parallel plate actuator and motion pick-up because of its larger actuation force and motional current, respectively. The effect of nonlinearity will be reduced using double-sided parallel plate and differential sensing, as will be discussed later.

3.2.1 Capacitive actuator

For capacitive actuation, the actuation force is essentially an electrostatic force, which is given by [82]:

$$F = \frac{1}{2}V^2\frac{\mathrm{d}C}{\mathrm{d}x} \tag{3.9}$$

where V, C, d, x are the voltage difference on the opposite plates, capacitance, gap between the parallel plates and displacement, respectively. Suppose that an AC voltage with an angular frequency of ω and an amplitude of v_{ac} is applied to the stator, and that a DC voltage of V_{dc} is applied to the rotor, so that $V = v_{ac}\sin\omega t - V_{dc}$. Equation 3.9 then becomes:

$$\begin{aligned} F &= \frac{1}{2}\left(V_{dc} - v_{ac}\sin\omega t\right)^2 \frac{\mathrm{d}C}{\mathrm{d}x} \\ &= \frac{1}{2}(V_{dc}^2 - 2V_{dc}v_{ac}\sin\omega t + v_{ac}^2\sin^2\omega t)\frac{\mathrm{d}C}{\mathrm{d}x} \\ &= \frac{1}{2}\left[(V_{dc}^2 + \frac{1}{2}v_{ac}^2) - 2V_{dc}v_{ac}\sin\omega t + \frac{1}{2}v_{ac}^2\cos 2\omega t)\right]\frac{\mathrm{d}C}{\mathrm{d}x} \end{aligned} \tag{3.10}$$

It can be seen that in addition to a force component at desired driving frequency of ω, there is also a DC force component, as well as an AC force component at twice the driving frequency, 2ω. The DC part sets the quiescent point of the resonator. To minimize the double frequency component, $v_{ac} \ll V_{dc}$ is assumed, so that the second order harmonic part can be neglected compared to the force components at ω and DC. In the analysis followed, the double frequency component will be neglected under this assumption.

For parallel plate actuators with given cross-sectional area of A, air gap of d and dielectric constant in air of ε_0, if the stator remains stationary and the rotor has a small displacement x in the x-axis, the capacitance is:

$$C = \frac{\varepsilon_0 A}{d + x} \tag{3.11}$$

Therefore,

$$\begin{aligned} \frac{\mathrm{d}C}{\mathrm{d}x} &= -\frac{\varepsilon_0 A}{(d+x)^2} \\ &= -\frac{\varepsilon_0 A}{d^2} + \frac{2\varepsilon_0 A}{d^3}x - \frac{3\varepsilon_0 A}{d^4}x^2 + \frac{4\varepsilon_0 A}{d^5}x^3 - \cdots \end{aligned} \tag{3.12}$$

Assuming that $v_{ac} \ll V_{dc}$, the total actuation force can be obtained from Equations 3.10 and 3.12:

$$\begin{aligned} F_{\text{total}} &\approx \left(\frac{V_{dc}^2}{2} - V_{dc}v_{ac}\sin\omega t\right)\frac{\mathrm{d}C}{\mathrm{d}x} \\ &\approx -\frac{V_{dc}^2}{2}\frac{\varepsilon_0 A}{d^2} + V_{dc}\frac{\varepsilon_0 A}{d^2}v_{ac}\sin\omega t \\ &+ \frac{V_{dc}^2}{2}\left(\frac{2\varepsilon_0 A}{d^3}x - \frac{3\varepsilon_0 A}{d^4}x^2 + \frac{4\varepsilon_0 A}{d^5}x^3 - \cdots\right) \end{aligned} \tag{3.13}$$

Here a *transduction factor*, $\eta = V_{dc}(\mathrm{d}C/\mathrm{d}x)$, is defined as the AC force to AC voltage ratio. For different types of actuation geometries, the transduction factor is different.

It can be seen from Equation 3.13 that the electrostatic actuation force is a constant AC force superimposed by a DC force and displacement-x-dependent forces. As mentioned above, DC force sets the operating point of the resonator. However, a sufficiently large DC force will cause pull-in instability [82]. We shall leave the DC force for now and analyse the other two components in what follows.

The AC actuation force equals to:

$$F_{ac} = V_{dc}\frac{\varepsilon_0 A}{d^2}v_{ac}\sin\omega t \equiv \eta_{A,P}v_{ac}\sin\omega t \tag{3.14}$$

We shall define $\eta_{A,P}$ as the actuation transduction factor [82], which is essentially the coefficient of the transformation from electrical energy to mechanical energy, as shown in Equation 3.14. Therefore the actuation transduction factor of parallel plates is:

$$\eta_{A,P} = V_{dc}\frac{\varepsilon_0 A}{d^2} \tag{3.15}$$

As for the forces dependent on the displacement x, it shows that the parallel plate actuator can also act like a spring, a nonlinear spring in particular, due to higher order terms with respect to x. Neglecting terms with order higher than 3, the behaviour of a nonlinear spring can be mathematically approximated by [106]:

$$F_e \approx -K_e x(1 + K_{2e}x + K_{3e}x^2) \tag{3.16}$$

The equivalent linear spring constant is therefore:

$$K_e = -\frac{V_{dc}^2\varepsilon_0 A}{d^3} \tag{3.17}$$

It can be seen that a parallel plate capacitive actuator has a negative spring constant, therefore, by using a parallel plate actuator to drive a MEMS resonator, effectively it will reduce the total stiffness.

In addition, the nonlinear terms are:

$$K_{2e} = \frac{3}{2d} \tag{3.18a}$$

$$K_{3e} = \frac{2}{d^2} \tag{3.18b}$$

We shall analyze these nonlinear terms further in later sections.

3.2.2 Capacitive motion pick-up

For a parallel plate motion pick-up, as shown in Figure 3.3, when a DC voltage difference of V is applied across the parallel plates, the displacement of the moving plate will cause a change in capacitance. Consequently, the charge across the capacitor changes, resulting in a current. If we define the motional current as the current resulting from the motion of the moving plate, supposing a positive DC voltage is applied on the moving plate, while the stationary plate is virtually grounded, this motional current caused by the charge alternation on the stationary plate is expressed as:

$$\begin{aligned} i &= -\frac{\partial Q}{\partial t} = -\frac{\partial (CV)}{\partial t} = -V\frac{\partial C}{\partial t} \\ &= -V\frac{\partial C}{\partial x}\frac{\partial x}{\partial t} \\ &= -V\left(-\frac{\varepsilon_0 A}{d^2} + \frac{2\varepsilon_0 A}{d^3}x - \frac{3\varepsilon_0 A}{d^4}x^2 + \frac{4\varepsilon_0 A}{d^5}x^3 - \cdots\right)\dot{x} \end{aligned} \tag{3.19}$$

Neglecting the nonlinear terms, the motional current can be approximated as:

$$i \approx V\frac{\varepsilon_0 A}{d^2}\dot{x} \equiv \eta_{S,P}\dot{x} \tag{3.20}$$

Here we define the sensing transduction factor, $\eta_{S,P}$, which is the quotient of the motional current divided by the velocity of the moving plate, and can be expressed as:

$$\eta_{S,P} = V\frac{\varepsilon_0 A}{d^2} \tag{3.21}$$

In addition to the motional current, the electrostatic force present between the sensing electrodes will also introduce an electrostatic spring as discussed in Section 3.2.1. If it is used to sense the motion of a MEMS resonator, the parallel plate motion pick-up will also lower the effective stiffness.

To minimize the nonlinear motional current generated by the parallel plates, one way is to use differential sensing based on a symmetrical parallel plates structure, as shown in Figure 3.4.

Suppose a DC voltage V is applied on the moving plate, while the stationary plates are grounded, and the plates are all identical, it is not difficult to find that the differential current cancels out the odd order terms of x, thus reducing the nonlinearity.

Another advantage of differential sensing is that it can reduce the common mode effect, such as feedthrough signal through parasitic capacitance [107], and also increase the signal to noise ratio.

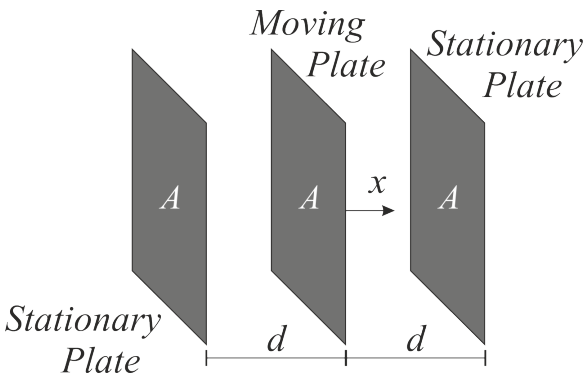

Figure 3.4: Demonstration of symmetrical differential capacitive motion pick-up. The cross sectional areas are identical for three plates, so are the gaps in between.

3.2.3 Electrostatic coupling

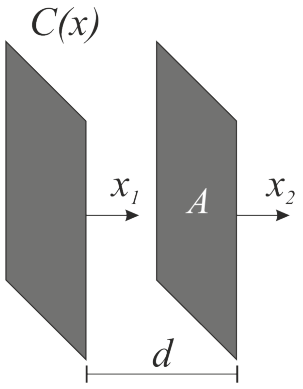

Figure 3.5: Demonstration of parallel plate electrostatic coupling.

As demonstrated in Section 3.2.1, the electrostatic force between a parallel plate actuator behave like a spring restoration force. Therefore, it was demonstrated that the electrostatic coupling could be used to couple the resonators [39, 63, 108]. To realize the electrostatic coupling, only a DC voltage is applied across the parallel plate. An electrostatic coupling utilising parallel plate structure is shown in Figure 3.5.

For both parallel plates are moving as shown in Figure 3.5, the total force exerted to the plate on the left can be obtained using previous results, neglecting terms with order higher than 3:

$$\begin{aligned} F_{\text{total}} \approx & \frac{V_{dc}^2}{2}\frac{\varepsilon_0 A}{d^2} \\ & + \frac{V_{dc}^2}{2}\left[\frac{2\varepsilon_0 A}{d^3}(x_1 - x_2) + \frac{3\varepsilon_0 A}{d^4}(x_1 - x_2)^2 + \frac{4\varepsilon_0 A}{d^5}(x_1 - x_2)^3\right] \end{aligned} \tag{3.22}$$

It can be seen from the mathematical expression that the linear coupling spring constant can be written as:

$$K_c = -\frac{V_{dc}^2 \varepsilon_0 A}{d^3} \tag{3.23}$$

It is also worth noticing that, when the dimensions are the same, and the same DC voltage is applied, the DC electrostatic force from the actuator and the coupling are the same but have the opposite sign. In addition, the second order terms in Equations 3.13 and 3.24 have the opposite signs. In situations when $x_2 \ll x_1$, the second order terms have approximately the same magnitude.

3.2.4 Symmetrical double sided capacitor structure

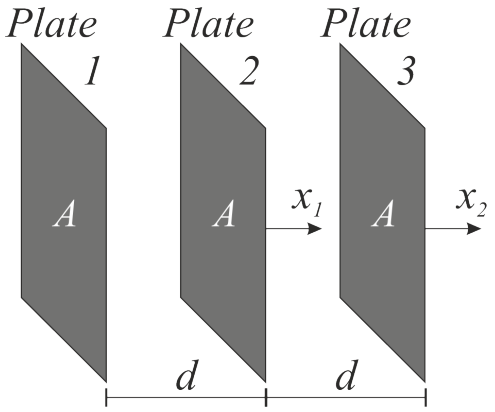

Figure 3.6: Demonstration of symmetrical double sided capacitor structure. The cross sectional areas are identical for three plates, so are the gaps in between.

From the theoretical analysis in previous sections, we can analyze the total force exerted to plate 2 for a symmetrical double sided capacitor structure as shown in Figure 3.6. Suppose a V_{dc} is applied on plate 2, a sinusoidal voltage $v_{ac} \sin \omega t$ with $v_{ac} \ll V_{dc}$ is applied on plate 1 and plate 3 is grounded. The total force on plate 2 can be approximated as:

$$\begin{aligned} F_{\text{total}} \approx{}& \eta_{A,P} v_{ac} \sin \omega t + \frac{\varepsilon_0 V_{dc}^2 A}{d^3} x_1 \\ &+ \frac{\varepsilon_0 V_{dc}^2 A}{d^3}(x_1 - x_2) - \frac{3\varepsilon_0 V_{dc}^2 A}{2d^4}[x_1^2 - (x_1 - x_2)^2] + \frac{2\varepsilon_0 V_{dc}^2 A}{d^5}[x_1^3 + (x_1 - x_2)^3] \end{aligned} \tag{3.24}$$

It becomes clear that a symmetrical structure as shown in Figure 3.6 will provide distinctive advantages for the plate 2. For instance, the DC force cancels out, so that

the maximum displacement to reach pull-in state is increased. This had already been demonstrated in [109].

Another advantage is that the dominating second order nonlinearity from the actuator is reduced. Consequently, reducing the total nonlinearities. In special cases where $x_2 \ll x_1$, the second order term is negligible, the third order term becomes dominant.

3.3 Modelling of MEMS resonators

To understand the linear response to the external actuation, it is helpful to model the MEMS resonator with a simple model, neglecting the nonlinearities. As demonstrated in Section 3.1, a linear MEMS resonator can be modelled as a lumped spring-damper-mass system, as shown in Figure 3.7.

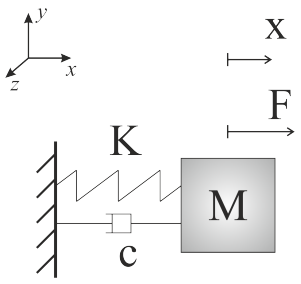

Figure 3.7: Spring-damper-mass system of a single resonator.

Based on this system, we can model the resonator using a transfer function model and an equivalent electrical circuit model. The transfer function modelling is a good tool to analytically solve the differential equations for coupled resonators; whereas the electrical circuit model is suitable for simulations, and it provides insight for integration of MEMS resonators with electrical measurement systems.

3.3.1 Transfer function model

Consider a linear resonator, with M, c and K as the effective mass, damping and stiffness of the resonator, respectively, and F as the external force. The equation of motion can be written as:

$$M\ddot{x} + c\dot{x} + Kx = F \tag{3.25}$$

Suppose the resonator is driven by a parallel plate capacitive actuator with a transduction factor of $\eta_{A,P}$, the actuation force is $F = \eta_{A,P} v \sin \omega t$. Performing Laplace transformation, Equation 3.25 can be rewritten as:

$$(Ms^2 + cs + K)x(s) = F(s) = \eta_{A,P}v(s) \tag{3.26}$$

where $x(s)$ is the vibration amplitude of displacement in the s-domain. Let $s = j\omega$, the transfer function is:

$$\frac{x(j\omega)}{v(j\omega)} = \frac{\eta_{A,P}}{M(j\omega)^2 + cj\omega + K} \tag{3.27}$$

If the output is the amplitude of velocity $U(j\omega)$ instead of the amplitude of displacement $x(j\omega)$, then the transfer function is:

$$\frac{U(j\omega)}{v(j\omega)} = \frac{\eta_{A,P}j\omega}{M(j\omega)^2 + cj\omega + K} \tag{3.28}$$

If this resonator employs capacitive sensing, with a transduction factor of $\eta_{S,P}$, then the transfer function from AC voltage input to motional current is:

$$\frac{i(j\omega)}{v(j\omega)} = \frac{(\eta_{A,P})(\eta_{S,P})j\omega}{M(j\omega)^2 + cj\omega + K} \tag{3.29}$$

This equation demonstrates the mechanical characteristics of the MEMS resonator. This leads to the modelling of the mechanical resonator in the electrical domain.

3.3.2 Electrical modelling of MEMS resonators

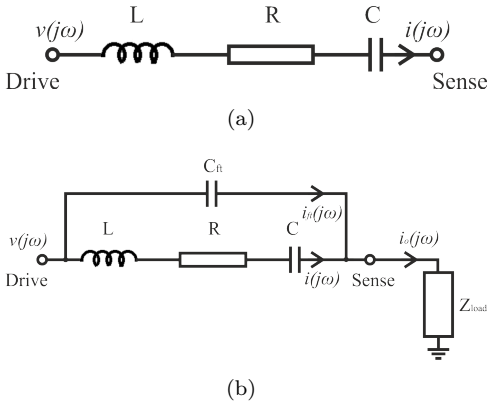

Figure 3.8: Equivalent RLC circuit model for MEMS resonator: a) simple equivalent circuit model for MEMS resonator; b) a more complex equivalent circuit model for MEMS resonator with feedthrough capacitor and load impedance.

Equation 3.29 can be rewritten as:

$$\begin{aligned} Y_R = \frac{i(j\omega)}{v(j\omega)} &= \frac{(\eta_{A,P})(\eta_{S,P})j\omega}{M(j\omega)^2 + cj\omega + K} \\ &\equiv \frac{1}{L_{\text{eff}}j\omega + R_{\text{eff}} + 1/(j\omega C_{\text{eff}})} \end{aligned} \tag{3.30}$$

where, Y_R is the admittance of the resonator. And L_{eff}, R_{eff} and C_{eff} are defined as:

$$\begin{aligned} L_{\text{eff}} &= \frac{M}{(\eta_{A,P})(\eta_{S,P})} \\ R_{\text{eff}} &= \frac{c}{(\eta_{A,P})(\eta_{S,P})} \\ C_{\text{eff}} &= \frac{(\eta_{A,P})(\eta_{S,P})}{K} \end{aligned} \tag{3.31}$$

This demonstrates that the MEMS resonator is equivalent to a series RLC circuit with components value of $L_{\text{eff}}, R_{\text{eff}}$ and C_{eff}. The simple equivalent RLC model is shown in Figure 3.8(a).

However, due to the parasitic capacitance between the drive node to the sense node, some current runs parallel to the MEMS resonator. Furthermore, the input impedance of the interfacing circuitry, as well as parasitic capacitance from the sense node to the ground, becomes the load of the RLC circuit. Taking these into consideration, a more complex model of the equivalent circuit is shown in Figure 3.8(b).

3.3.2.1 Feedthrough capacitance

From the equivalent circuit model, it can be seen that the feedthrough capacitor brings an extra zero into the total admittance, therefore usually an anti-resonance can be discovered [98]. To ensure minimum effect of the feedthrough capacitance, the following conditions should be satisfied:

$$R_{\text{eff}}C_{\text{ft}} \ll \frac{1}{\omega_0} \tag{3.32a}$$

$$C_{\text{ft}} \ll C_{\text{eff}} \tag{3.32b}$$

Condition 3.32a ensures that the phase is roughly 0° at main resonant frequency ω_0. Condition 3.32b ensures that the anti-resonance frequency is much higher than the fundamental mode frequency of the resonator, thus reducing the effect of anti-resonance.

3.3.2.2 Load impedance

We neglect the effect of feedthrough capacitance for the analysis of load impedance. The load is normally a preamplifier with resistive and capacitive components. Therefore, the load impedance will not have any impact on the inductance part of the resonator. However, the resistive component of the load increases the dissipation, which leads to higher damping coefficient and therefore lower quality factor, as well as higher power dissipation. Therefore, a type of preamplifier with negligible input resistance is necessary.

Furthermore, the capacitive components of the load is in series with the equivalent capacitance of the resonator, making the effective capacitance lower than that of the unloaded resonator, which causes the resonant frequency to be higher than unloaded resonator. However, the input capacitance is usually in the order of pF, while the equivalent capacitance is usually lower than fF, therefore, the effect of the capacitive load can be neglected.

3.4 Summary

In this chapter, fundamental theories of MEMS resonators, including resonator dynamics, transduction technologies (including electrostatic coupling) and resonator modelling are covered. We have laid the theoretical foundations for future analysis of a 3DoF coupled resonator sensor. We have also demonstrated three different types of beams used for resonator structures, and compared certain specifications such as stiffness and mechanical nonlinearity of these beams. In addition, capacitive transduction, as well as electrostatic coupling are discussed. We have also demonstrated the advantages of differential motion pick-ups and double sided structures, such as reducing the electrostatic nonlinearities. Finally, we have covered two models for the physical modelling of a MEMS resonator.

Chapter 4

Vibrational Behaviour Analysis of 3DOF Coupled Resonator System

4.1 Introduction

It was demonstrated that by employing mode localization effect in a weakly coupled resonator sensor, substantial improvement in sensitivity of the sensor [36, 39, 108] can be observed compared to single resonator with frequency shift as output. Therefore, an intuitive approach is to use a 3DoF resonator system to improve the sensitivity further from a 2DoF system. The intuition is that by adding one more energy storage component, the insertion loss of the component attenuates the energy propagation down the chain, making the energy more confined when perturbations are introduced. Hence, intuitively, adding more resonators makes the mode localization stronger than a 2DoF system.

Before proceeding to employ a 3DoF resonator system for sensing applications, it is necessary to study the modal behaviour of a 3DoF resonator system, i.e. mode frequencies and amplitudes. It should be pointed out that the amplitudes are proportional to the drive forces of the resonators. Hence, for the sake of generality, to gauge the change in mode amplitudes, we used amplitude ratios, eliminating the factor of the drive forces.

To theoretically analyze the modal behaviour of a 3DoF system, two methods are used in this chapter. One is a method using a basic algebraic method. The mathematics for this method is tedious for analysis with damping, therefore it is suitable for analysing ideal systems without any damping.

The other is a novel approach utilising transfer function model of the MEMS resonator as demonstrated in Chapter 3, which, according to the author's knowledge, has not been used in previous analysis of a coupled resonator system. Opposed to the algebraic approach or the matrix approach used in [34] without damping, this approach necessitates

the inclusion of damping, otherwise the maximum vibration amplitude will not converge. This enables the analysis of a more practical coupled resonator systems. In addition, the transfer function model also allows the mechanical noise analysis. Furthermore, this approach also enables system level analysis including feedback, as shall be seen in later chapters. The theoretical results are verified by simulation.

4.2 3DoF coupled resonator behaviour analysis without damping

To analyze the behaviour of a 3DoF resonator system, the algebraic method is used in this section.

4.2.1 Unperturbed case

First consider an ideal, undamped, 3DoF weakly coupled resonator system as shown in Figure 4.1. The masses are totally identical, $M_1 = M_2 = M_3 = M$, spring constants satisfy $K_1 = K_3 = K, K_{c1} = K_{c2} = K_c$, and $K_2 \geq 2K$. Thus the resonator in the middle is different from its neighbouring resonators in terms of stiffness. In addition, we assume that no force is applied, $F_1 = F_2 = F_3 = 0$.

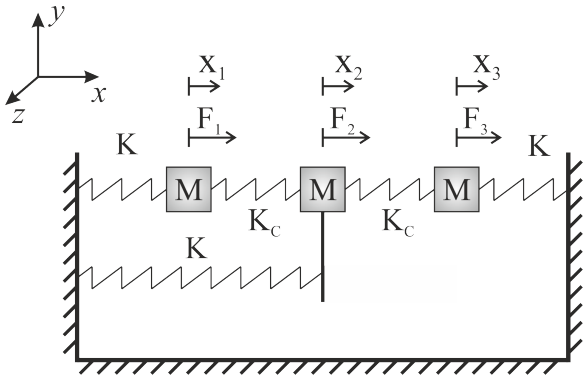

Figure 4.1: A spring-mass model of a 3DoF system.

With $\ddot{X}_i = -\omega^2 X_i$ $(i = 1, 2, 3)$, Equations of motion can be written as:

$$-M_1\omega^2 X_1 = -(K + K_c)X_1 + K_c X_2 \tag{4.1a}$$

$$-M_2\omega^2 X_2 = -(K_2 + 2K_c)X_2 + K_c X_1 + K_c X_3 \tag{4.1b}$$

$$-M_3\omega^2 X_3 = -(K + K_c)X_3 + K_c X_2 \tag{4.1c}$$

To analyze the behaviour of the system, the equations shall be solved. However, the system is underdetermined with 4 unknowns and only 3 equations. It can be found that $X_i \neq 0, i = 1$ and 3, therefore, we can define the following:

$$r_1 = \frac{X_2}{X_1}, \quad r_2 = \frac{X_2}{X_3} \tag{4.2}$$

It is not difficult to obtain the following from Equations 4.1a to 4.1c:

$$K_c r_1 [K_c r_1^2 + (K_2 - K + K_c) r_1 - 2K_c] = 0 \tag{4.3}$$

and

$$M\omega^2 = K + K_c - K_c r_1 \tag{4.4}$$

Using basic algebra, it can be seen that there are three solutions of r_1 to Equation 4.3, one negative, one zero and one positive. These solutions correspond to three solutions of ω, meaning that there are three distinctive modes of the system:

- The positive solution of r_1 corresponds to the first mode with the lowest frequency. It is not difficult to find that the three resonators vibrate in-phase at this frequency;
- The solution $r_1 = 0$ corresponds to the second mode with resonator 2 remains stationary while the resonators on either sides vibrate out-of-phase, having a phase difference of 180°;
- The negative solution of r_1 corresponds to the third mode having the highest resonant frequency. At this frequency, each resonator is out-of-phase with its neighbouring resonator, so resonators 1 and 3 are in phase, but out-of-phase with resonator 2.

This conclusion matches with the description of vibration modes of a 3DoF vibratory system in [35]. If we assume weak coupling as the following:

$$|K_c| < \frac{K}{10} \leq \frac{K_2 - K}{10} \tag{4.5}$$

Once Equation 4.5 is satisfied, the vibration amplitudes of resonators 1 and 3 are trivial compared to that of resonator 2 for the third mode. Therefore, the modes of interest for the purpose of this work are the first two modes, which we will refer to as the in-phase and out-of-phase modes, respectively.

Due to the symmetry of Equations 4.1a and 4.1c, $X_1 = X_3$ for the in-phase mode and $X_1 = -X_3$ for the out-of-phase mode.

4.2.2 Perturbed case with stiffness perturbation to resonator 3

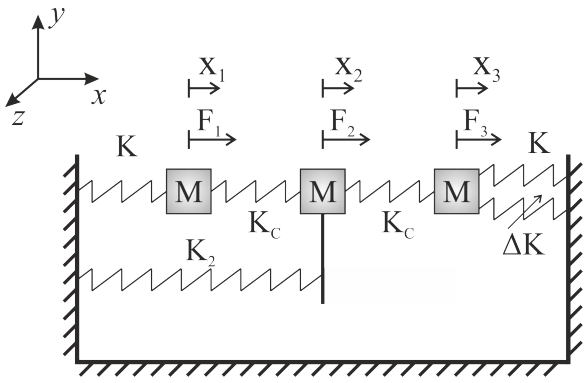

Figure 4.2: A spring-mass model of a perturbed 3DoF system, with perturbation occurring to resonator 3.

First we consider a case with a negative perturbation occurring to resonator 3 with $\Delta K < 0$, the equations of motion become:

$$-M_1\omega^2 X_1 = -(K + K_c)X_1 + K_c X_2 \tag{4.6a}$$

$$-M_2\omega^2 X_2 = -(K_2 + 2K_c)X_2 + K_c X_1 + K_c X_3 \tag{4.6b}$$

$$-M_3\omega^2 X_3 = -(K + \Delta K + K_c)X_3 + K_c X_2 \tag{4.6c}$$

To solve Equations 4.6a to 4.6c for weak coupling (satisfying Equation 4.5), using the defined ratios (Equation 4.2), divide Equation 4.6a by X_1 and Equation 4.6c by X_3. Subtracting the resulting equations, we can obtain:

$$r_2 = r_1 + \frac{\Delta K}{K_c} \tag{4.7}$$

It can be seen from Equations 4.6a to 4.6c that the amplitudes do not equal zero, $X_i \neq 0, i = 1, 2, 3$. Therefore $r_{1,2} \neq 0$. Substituting Equation 4.7 into Equations 4.6a and Equation 4.6b, and eliminating $M\omega^2$, we can obtain:

$$\begin{aligned} & K_c r_1[K_c r_1^2 + (K_2 - K + K_c)r_1 - 2K_c] \\ + \quad & \Delta K[K_c r_1^2 + (K_2 - K + K_c)r_1 - K_c] \quad = 0 \end{aligned} \tag{4.8}$$

Before proceeding to solve the cubic equation, it is important to find the loci of the possible roots of Equation 4.8 with changing $\Delta K < 0$. We are able to plot the root loci [110] for Equation 4.8 as shown in Figure 4.3:

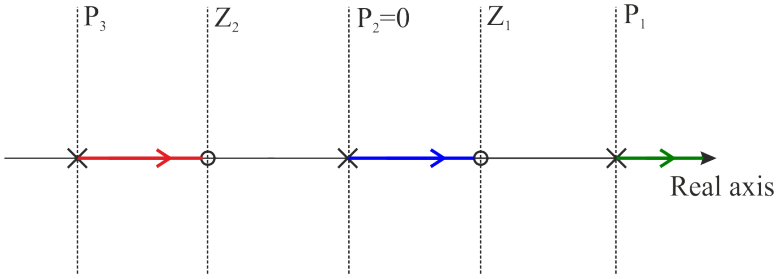

Figure 4.3: Root locus of r_1 for $\Delta K < 0$.

where $Z_{1,2}$ are the solution to equation:

$$K_c r_1^2 + (K_2 - K + K_c) r_1 - K_c = 0 \tag{4.9}$$

and $P_{1,2,3}$ are the solution to equation:

$$r_1 (K_c r_1^2 + (K_2 - K + K_c) r_1 - 2K_c) = 0 \tag{4.10}$$

To verify this, a Matlab simulation is run. For the simulation, $K_2 = 2K$ and $K = 50K_c$. The root locus of r_1 is shown in Figure 4.4. It can be seen that the simulation results agree with the theoretical predictions.

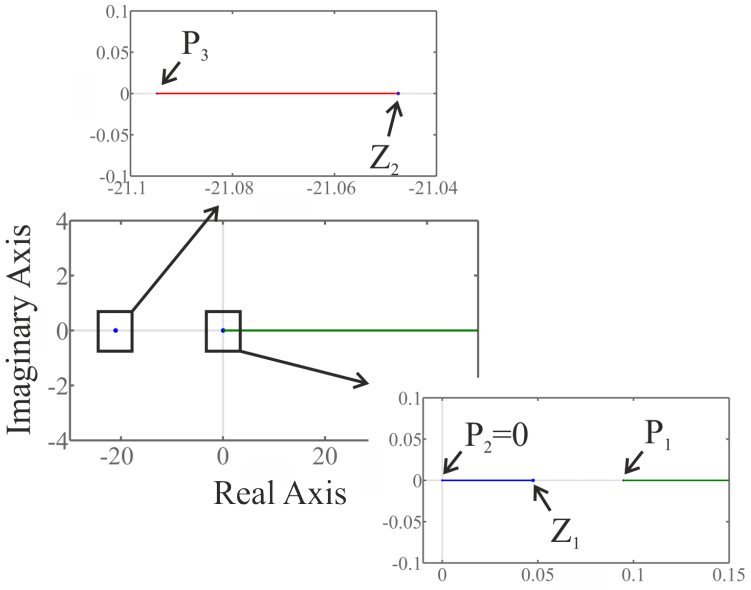

Figure 4.4: Matlab simulated root locus of r_1 with for $\Delta K < 0$.

Three separate segments of root locus indicate that there are always three distinctive solutions of r_1 for Equation 4.8. It can also be seen in the figure that all three solutions for r_1 with any $\Delta K < 0$ are real numbers.

a) Out-of-phase mode: for a solution $r_{1,\mathrm{op}}$ of Equation 4.8 on the blue segment of the root locus (shown in Figure 4.4, $0 < r_{1,\mathrm{op}} < Z_1$), corresponding to a real $\Delta K < 0$, there must be a real value $\mathcal{R}_{\mathrm{op}}$ that satisfies:

$$\Delta K = K_c r_{1,\mathrm{op}} \mathcal{R}_{\mathrm{op}} \quad \mathcal{R}_{\mathrm{op}} < 0 \text{ for } K < 0 \tag{4.11}$$

Substituting Equation 4.11 into Equation 4.8, it can be seen that for $r_{1,\mathrm{op}}$, the following condition should also be satisfied:

$$\mathfrak{F}(r_{1,\mathrm{op}}) = r_{1,\mathrm{op}}^2 + \frac{K_2 - K + K_c}{K_c} r_{1,\mathrm{op}} - \frac{2 + \mathcal{R}_{\mathrm{op}}}{1 + \mathcal{R}_{\mathrm{op}}} = 0 \tag{4.12}$$

It can be concluded from fundamental theorems for a quadratic function $\mathfrak{F}$ that, for a $0 < r_{1,\mathrm{op}} < Z_1$ that satisfies $\mathfrak{F}(r_{1,\mathrm{op}}) = 0$ to exist, $\mathfrak{F}(0)\mathfrak{F}(Z_1) < 0$ should be satisfied. We are able to find the resulting range of $\mathcal{R}_{\mathrm{op}} < -2$. This indicates that $0 < (2+\mathcal{R}_{\mathrm{op}})/(1+\mathcal{R}_{\mathrm{op}}) < 1$.

Assumption weak coupling, expressed in mathematical form as:

$$|K_c| < \frac{K}{10} < \frac{K_2 - K}{10} \tag{4.13}$$

Solving Equation 4.12, the following relationship between r_1 and $\mathcal{R}_{\mathrm{op}}$ can be found:

$$r_{1,\mathrm{op}} \approx \frac{\mathcal{R}_{\mathrm{op}} + 2}{\mathcal{R}_{\mathrm{op}} + 1} \frac{K_c}{K_2 - K + K_c} \tag{4.14}$$

Substitute Equation 4.14 into Equation 4.11, we can obtain:

$$\Delta K = \mathcal{R}_{\mathrm{op}} K_c r_{1,\mathrm{op}} \approx \frac{\mathcal{R}_{\mathrm{op}}^2 + 2\mathcal{R}_{\mathrm{op}}}{\mathcal{R}_{\mathrm{op}} + 1} \frac{K_c^2}{K_2 - K + K_c} \tag{4.15}$$

Solving $\mathcal{R}_{\mathrm{op}}$ from Equation 4.15, we are able to obtain $\mathcal{R}_{\mathrm{op}}$ as a function of ΔK:

$$\mathcal{R}_{\mathrm{op}} \approx \frac{-2 + \gamma_3 \delta K - \sqrt{(\gamma_3 \delta K)^2 + 4}}{2} \quad (\Delta K < 0) \tag{4.16}$$

where,

$$\gamma_3 = \frac{K(K_2 - K + K_c)}{K_c^2}, \quad \text{absolute normalized sensitivity} \tag{4.17a}$$

$$\delta K = \frac{\Delta K}{K}, \quad \text{normalized stiffness perturbation} \tag{4.17b}$$

Here we have obtained the mathematical expression of the normalized sensitivity γ_3 first time in the thesis. Equation 4.17a is *the most important* expression in the thesis, and will be used throughout the thesis.

From Equation 4.7, it can be shown that:

$$\frac{r_{2,\text{op}}}{r_{1,\text{op}}} = 1 + \mathcal{R}_{\text{op}} \tag{4.18}$$

Substitute Equation 4.16 into Equation 4.18, it can be found that:

$$\left.\frac{X_1}{X_3}\right|_{\text{op}} = \frac{r_{2,\text{op}}}{r_{1,\text{op}}} = 1 + \mathcal{R}_{\text{op}} \approx \frac{\gamma_3 \delta K - \sqrt{(\gamma_3 \delta K)^2 + 4}}{2} \tag{4.19}$$

For $\Delta K < 0$, it is not difficult to see that at this mode, $X_3/X_1 < 0$. Thus this solution corresponds to the out-of-phase mode. With the $\mathcal{R}_{\text{op}}$ solved, $r_{1,\text{op}}$ can also be obtained using Equation 4.11. The angular frequency for the out-of-phase mode can therefore be deduced from Equation 4.4:

$$\omega_{\text{op}} \approx \sqrt{\frac{1}{M}\left[K + K_c + \frac{1}{2}(\Delta K - \alpha + \sqrt{\Delta K^2 + \alpha^2})\right]} \tag{4.20}$$

where

$$\alpha = \frac{2K_c^2}{K_2 - K + K_c} \tag{4.21}$$

Following the same process, the amplitude ratio and mode frequency for $\Delta K > 0$ can also be calculated. It can be demonstrated that Equations 4.19 and 4.20 are also valid for positive perturbations provided that $|\Delta K| \ll K_2 - K + K_c$.

b) In-phase mode: as for this mode, similar procedure for deriving the out-of-phase mode frequency can be applied. We are able to approximate the in-phase mode frequency as:

$$\omega_{\text{ip}} \approx \sqrt{\frac{1}{M}\left[K + K_c + \frac{1}{2}(\Delta K - \alpha - \sqrt{\Delta K^2 + \alpha^2})\right]} \tag{4.22}$$

Provided that $|\Delta K| \ll K_2 - K + K_c$ is satisfied. At the in-phase mode frequency:

$$\left.\frac{X_1}{X_3}\right|_{\text{ip}} = \frac{r_{2,\text{ip}}}{r_{1,\text{ip}}} = 1 + \mathcal{R}_{\text{ip}} \approx \frac{\gamma_3 \delta K + \sqrt{(\gamma_3 \delta K)^2 + 4}}{2} \tag{4.23}$$

Alternatively, we can model the 3DoF resonator system using matrix form, then the amplitude ratios and the mode frequencies can be obtained by solving the corresponding eigenvalue problem [34]. Matlab can solve the eigenvalue problems using "eig" function. Hence, by modelling the system using matrix, we can then obtain the eigenvalues and amplitude ratios using a Matlab programme (an example code is attached in Appendix C). Comparing the solution of the Matlab programme to our derived results, we can then verify the mode frequencies and amplitude ratios. First the matrix mathematical form of the 3DoF resonator can be written as:

$$\lambda \begin{bmatrix} X_1 \\ X_2 \\ X_3 \end{bmatrix} = \begin{bmatrix} \frac{K+K_c}{M} & -\frac{K_c}{M} & 0 \\ -\frac{K_c}{M} & \frac{K_2+2K_c}{M} & -\frac{K_c}{M} \\ 0 & -\frac{K_c}{M} & \frac{K+\Delta K+K_c}{M} \end{bmatrix} \begin{bmatrix} X_1 \\ X_2 \\ X_3 \end{bmatrix} \tag{4.24}$$

where λ is the eigenvalue of the 3×3 matrix on the right hand side of the equation, from which the mode frequency ω can be obtained ($\omega = \sqrt{\lambda}$). The amplitude ratios can be obtained from the eigenstates ($[X_1\ X_2\ X_3]^{\text{T}}$).

The values used for the Matlab simulation are listed in Table 4.1. These values are used for the simulation because they are very close to the design values of one of the tested devices. From the simulated results using Matlab, it can be demonstrated that our solution using the algebraic approach is very accurate, with maximum relative error lower than 1.2% for amplitude ratio and 4×10^{-6}% for mode frequencies.

Table 4.1: Values used in the Matlab simulation

Component	Value
K	57.62N/m
K_c	-0.69N/m
K_2	199.55N/m
M	6.94μg

4.2.3 Perturbed case with stiffness perturbation to resonator 1

Now we consider the situation where a perturbation is introduced to the spring of resonator 1. Due to the symmetry of the system about resonator 2, we are able to directly

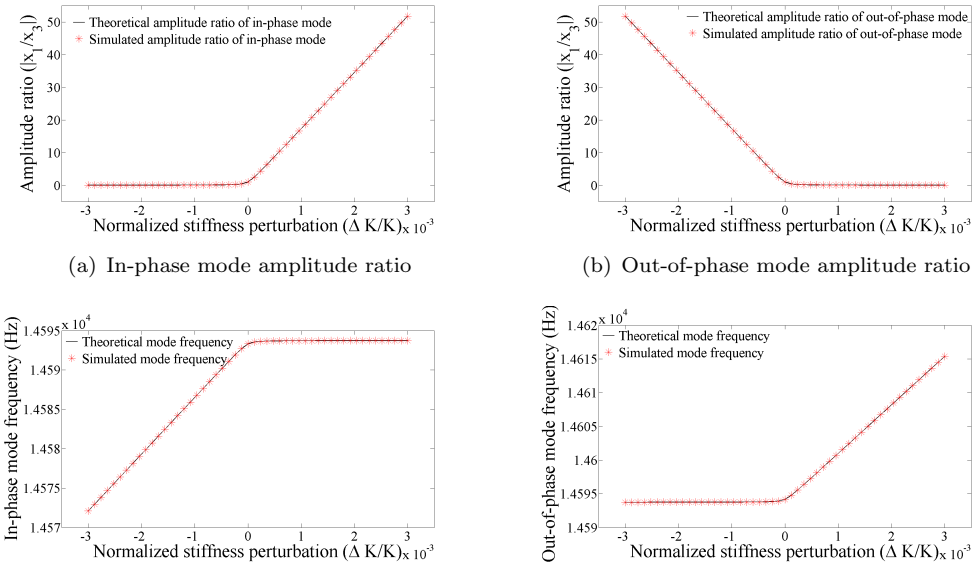

(a) In-phase mode amplitude ratio

(b) Out-of-phase mode amplitude ratio

(c) In-phase mode frequency

(d) Out-of-phase mode frequency

Figure 4.5: Comparison between theoretically estimated values using algebraic method (black) and Matlab simulated values (red) of amplitude ratios and mode frequencies, for stiffness perturbations to resonator 3: a) in-phase mode amplitude ratio, b) out-of-phase mode amplitude ratio, c) in-phase mode frequency and d) out-of-phase mode frequency.

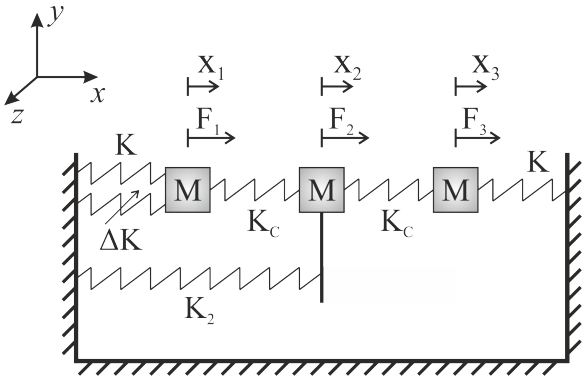

Figure 4.6: A spring-mass model of a perturbed 3DoF system, with perturbation occurring to resonator 1.

use the results derived previously, provided that $|\Delta K| \ll K_2 - K + K_c$ is satisfied.

a) Out-of-phase mode: for the out-of-phase mode, the mode frequency is:

$$\omega_{\text{op}} \approx \sqrt{\frac{1}{M}\left[K + K_c + \frac{1}{2}(\Delta K - \alpha + \sqrt{\Delta K^2 + \alpha^2})\right]} \tag{4.25}$$

Amplitude ratio at this frequency is:

$$\left.\frac{X_3}{X_1}\right|_{\text{op}} \approx \frac{\gamma_3\delta K - \sqrt{(\gamma_3\delta K)^2+4}}{2} \tag{4.26}$$

Therefore,

$$\left.\frac{X_1}{X_3}\right|_{\text{op}} \approx \frac{2}{\gamma_3\delta K - \sqrt{(\gamma_3\delta K)^2+4}} \approx \frac{-\gamma_3\delta K - \sqrt{(\gamma_3\delta K)^2+4}}{2} \tag{4.27}$$

b) In-phase mode: for the in-phase mode, the mode frequency is:

$$\omega_{\text{ip}} \approx \sqrt{\frac{1}{M}\left[K + K_c + \frac{1}{2}(\Delta K - \alpha - \sqrt{\Delta K^2+\alpha^2})\right]} \tag{4.28}$$

At the in-phase mode:

$$\left.\frac{X_3}{X_1}\right|_{\text{ip}} \approx \frac{\gamma_3\delta K + \sqrt{(\gamma_3\delta K)^2+4}}{2} \tag{4.29}$$

Therefore,

$$\left.\frac{X_1}{X_3}\right|_{\text{ip}} \approx \frac{2}{\gamma_3\delta K + \sqrt{(\gamma_3\delta K)^2+4}} \approx \frac{-\gamma_3\delta K + \sqrt{(\gamma_3\delta K)^2+4}}{2} \tag{4.30}$$

It can be seen that in terms of amplitude ratios, by comparing Equation 4.27 to Equation 4.19 and Equation 4.30 to Equation 4.23, mathematically, a positive perturbation $\Delta K > 0$ in resonator 1 is equivalent to a negative perturbation $-\Delta K < 0$ in resonator 3, vice versa.

However, as far as the mode frequency is concerned, the same perturbation in resonator 1 or 3 has the same effect.

Combining these two reasons, amplitude ratio detection has the capability of detecting the position of the perturbation, whereas frequency shift detection does not. This conclusion can be helpful in future research for which knowing the position of the perturbation is important.

To verify these expressions, Matlab calculations without any assumptions were performed. The parameters for the simulation were identical to the calculations in the previous section (shown in Table 4.1), except that the perturbations was stiffness perturbations to resonator 1. The theoretical results (Equations 4.25, 4.28, 4.27 and 4.30) are compared to the Matlab calculated results, and plotted in Figure 4.7. It can be seen from the theoretical results agreed well with the Matlab simulation results.

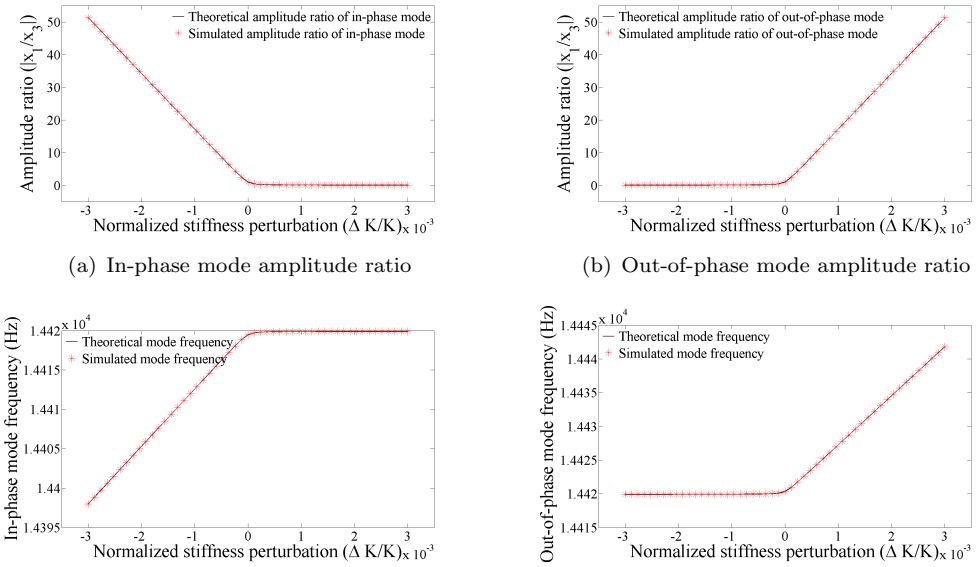

(a) In-phase mode amplitude ratio

(b) Out-of-phase mode amplitude ratio

(c) In-phase mode frequency

(d) Out-of-phase mode frequency

Figure 4.7: Comparison between theoretically estimated values using algebraic method (black) and Matlab simulated values (red) of amplitude ratios and mode frequencies, for stiffness perturbations to resonator 1: a) in-phase mode amplitude ratio, b) out-of-phase mode amplitude ratio, c) in-phase mode frequency and d) out-of-phase mode frequency.

4.2.4 Perturbed case with stiffness perturbation to resonators 1 and 3

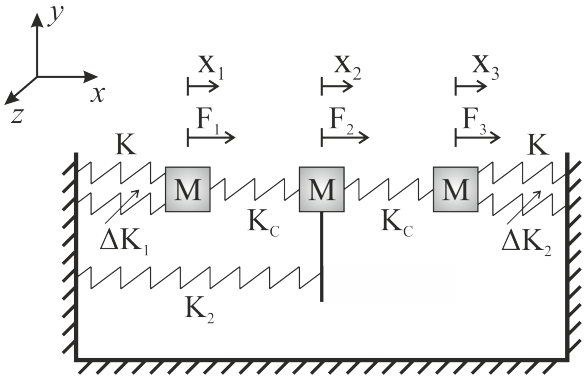

Figure 4.8: A spring-mass model of a perturbed 3DoF system, with perturbation occurring to both resonator 1 and 3.

Consider the 3DoF system is perturbed by two perturbations at the same time, as shown in Figure 4.8. We shall now define $K' = K + \Delta K_1$. Hence the effective stiffness perturbation to resonator 3 is $\Delta K' = \Delta K_3 - \Delta K_1$.

Now substitute K' for K and $\Delta K'$ for ΔK into the equations of motion (Equations 4.6a to 4.6c), and follow the same procedure as shown in section 4.2.2, assuming $\Delta K_{1,2} \ll K$,

we can obtain:

$$\left.\frac{X_1}{X_3}\right|_{\text{op}} \approx \frac{\gamma_3\delta K' - \sqrt{(\gamma_3\delta K')^2+4}}{2} \tag{4.31a}$$

$$\omega_{\text{op}} \approx \sqrt{\frac{1}{M}\left[K' + K_c + \frac{1}{2}(\Delta K' - \alpha + \sqrt{\Delta K'^2+\alpha^2})\right]} \tag{4.31b}$$

$$\left.\frac{X_1}{X_3}\right|_{\text{ip}} \approx \frac{\gamma_3\delta K' + \sqrt{(\gamma_3\delta K'^2)+4}}{2} \tag{4.31c}$$

$$\omega_{\text{ip}} \approx \sqrt{\frac{1}{M}\left[K' + K_c + \frac{1}{2}(\Delta K' - \alpha - \sqrt{\Delta K'^2+\alpha^2})\right]} \tag{4.31d}$$

where

$$\delta K' = \frac{\Delta K'}{K} = \frac{\Delta K_2 - \Delta K_1}{K} \tag{4.32}$$

To verify Equations 4.31a to 4.31d, Matlab simulations using the values listed in Table 4.1 were run. A constant stiffness perturbation $\Delta K_2 = -0.0346$ was introduced to resonator 3, while the varying stiffness perturbations was introduced to resonator 1. Hence in the following figures, the normalized stiffness perturbations $\Delta K/K$ was in fact $\Delta K_1/K$. It can be seen that Equations 4.31a to 4.31d can be regarded as accurate estimations of the amplitude ratios and mode frequencies.

It can be seen from Equations 4.31a and 4.31c that the amplitude ratios are functions of perturbation difference $\Delta K_2 - \Delta K_1$. Whereas it can also be seen from Equations 4.31d and 4.31d that the mode frequencies change with both perturbations. This indicates that the amplitude ratios have the capability of common mode rejection compared to the frequency shifts, which was also concluded in other similar research [36, 41].

Another significance of Figures 4.9(a) and 4.9(b) is that, it demonstrated that the amplitude ratio curves can be translated, hence the starting point for the varying stiffness perturbations can be biased. It should also be noticed that the biased starting point can be altered by changing ΔK_2. This shall be used later.

4.2.5 Summary

It has been demonstrated that with the balance broken, two modes of interest are disturbed; i.e. both the mode shapes and frequencies change, while the order of the modes

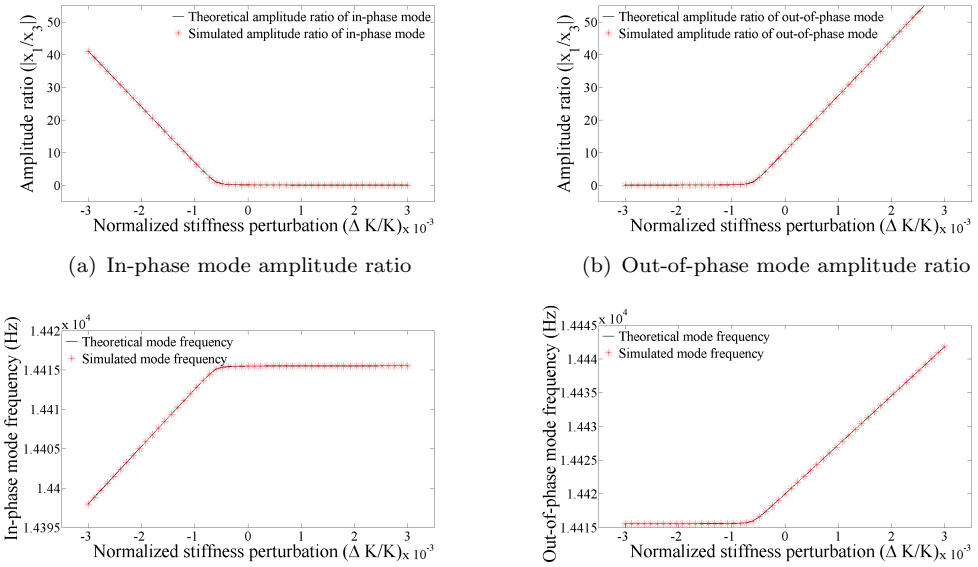

(a) In-phase mode amplitude ratio

(b) Out-of-phase mode amplitude ratio

(c) In-phase mode frequency

(d) Out-of-phase mode frequency

Figure 4.9: Comparison between theoretically estimated using algebraic method and Matlab simulated values of amplitude ratios and mode frequencies, for stiffness perturbations to both resonators 1 and 3: a) in-phase mode amplitude ratio, b) out-of-phase mode amplitude ratio, c) in-phase mode frequency and d) out-of-phase mode frequency.

in frequency domain remain unchanged due to frequency veering [62], so called *mode localization* occurs [62].

From the analysis, it can be shown that the amplitude ratios have two advantages compared to frequency shifts: (a) they can be used to detect the position of the perturbation; (b) they have the capability of common mode rejection.

4.3 3DoF coupled resonator behaviour analysis with damping

The previous analysis using algebraic approach provides no information regarding how the system would respond if damping is present. Furthermore, the algebraic analysis assumed no external driving forces, which is not practical in MEMS resonator systems. Combining the two reasons, a more complete analysis of the behaviour of a 3DoF coupled resonator system using transfer function model is necessary.

4.3.1 Coupled resonator models

The spring-mass-damper model of a damped 3DoF coupled resonator system is shown in Figure 4.10.

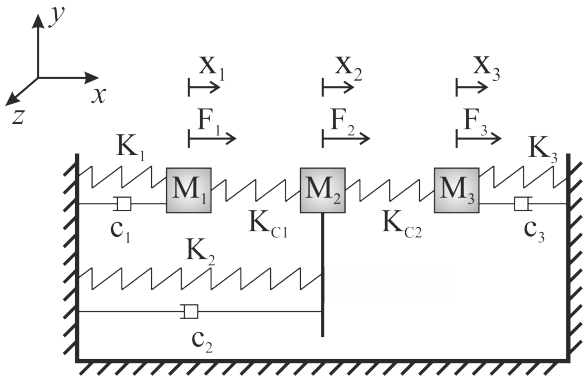

Figure 4.10: A spring-mass-damper model of a damped 3DoF resonator system, with external forces applied

Assuming that all the springs are linear, the equations of motion can be written as:

$$M_1\ddot{X}_1 + c_1\dot{X}_1 + (K_1 + K_{c1})X_1 - K_{c1}X_2 = F_1 \tag{4.33a}$$

$$M_2\ddot{X}_2 + c_2\dot{X}_2 + (K_2 + K_{c1} + K_{c2})X_2 - K_{c1}X_1 - K_{c2}X_3 = F_2 \tag{4.33b}$$

$$M_3\ddot{X}_3 + c_3\dot{X}_3 + (K_3 + K_{c2})X_3 - K_{c2}X_2 = F_3 \tag{4.33c}$$

Performing Laplace transform in all of the equations above, and rearranging:

$$[M_1s^2 + c_1s + (K_1 + K_{c1})]X_1(s) = K_{c1}X_2(s) + F_1(s) \tag{4.34a}$$

$$[M_2s^2 + c_2s + (K_2 + K_{c1} + K_{c2})]X_2(s) = K_{c1}X_1(s) + K_{c2}X_3(s) + F_2(s) \tag{4.34b}$$

$$[M_3s^2 + c_3s + (K_3 + K_{c2})]X_3(s) = K_{c2}X_2(s) + F_3(s) \tag{4.34c}$$

According to the Equations 4.34a, 4.34b and 4.34c, we are able to sketch the block diagram of the forced and damped 3DoF coupled resonator, as displayed in Figure 4.11.

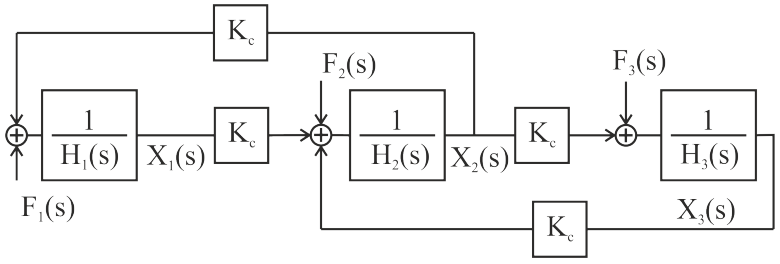

Figure 4.11: The block diagram of a forced 3DoF system

The s dependant gains are defined to be:

$$H_1(s) \equiv M_1s^2 + c_1s + (K_1 + K_{c1}) \tag{4.35a}$$

$$H_2(s) \equiv M_2 s^2 + c_2 s + (K_2 + K_{c1} + K_{c2}) \tag{4.35b}$$

$$H_3(s) \equiv M_3 s^2 + c_3 s + (K_3 + K_{c2}) \tag{4.35c}$$

Let $s = j\omega$, we are able to obtain the transfer functions in the matrix form:

$$\begin{bmatrix} X_1(j\omega) \\ X_2(j\omega) \\ X_3(j\omega) \end{bmatrix} = \mathbf{H} \begin{bmatrix} F_1(j\omega) \\ F_2(j\omega) \\ F_3(j\omega) \end{bmatrix} \tag{4.36}$$

where

$$\mathbf{H} = \begin{bmatrix} H_{11}(j\omega) & H_{12}(j\omega) & H_{13}(j\omega) \\ H_{21}(j\omega) & H_{22}(j\omega) & H_{23}(j\omega) \\ H_{31}(j\omega) & H_{32}(j\omega) & H_{33}(j\omega) \end{bmatrix} \tag{4.37}$$

By applying Mason's rule [111] to the block diagram shown in Fig. 4.11, we are able to obtain the following transfer functions:

$$H_{11}(j\omega) = \frac{H_2(j\omega)H_3(j\omega) - K_c^2}{D(j\omega)} \tag{4.38a}$$

$$H_{22}(j\omega) = \frac{H_1(j\omega)H_3(j\omega)}{D(j\omega)} \tag{4.38b}$$

$$H_{33}(j\omega) = \frac{H_1(j\omega)H_2(j\omega) - K_c^2}{D(j\omega)} \tag{4.38c}$$

$$H_{12}(j\omega) = H_{21}(j\omega) = \frac{H_3(j\omega)K_c}{D(j\omega)} \tag{4.38d}$$

$$H_{23}(j\omega) = H_{32}(j\omega) = \frac{H_1(j\omega)K_c}{D(j\omega)} \tag{4.38e}$$

$$H_{13}(j\omega) = H_{31}(j\omega) = \frac{K_c^2}{D(j\omega)} \tag{4.38f}$$

where

$$D(j\omega) = H_1(j\omega)H_2(j\omega)H_3(j\omega) - [H_1(j\omega) + H_3(j\omega)]\, K_c^2 \tag{4.39}$$

As described in Chapter 3, a single resonator can be modelled into an RLC circuit. By applying the transfer functions, we can build an electronic RLC circuit equivalent to a 3DoF coupled resonator system, as demonstrated in Figure 4.12.

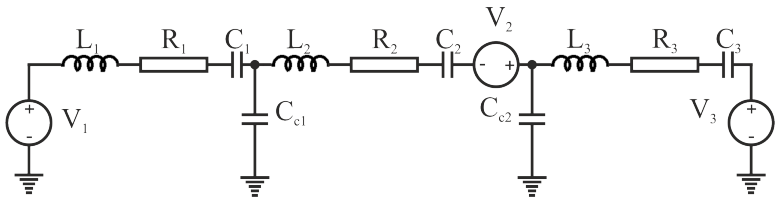

Figure 4.12: The electronic circuit model of a forced 3DoF system

Like the single resonator, the masses are modelled as inductors, damping as resistors and springs as capacitors. The three voltage sources are forces sources. The effective value can be calculated from Equation 3.31. This is a similar to the model of a 3DoF resonator system proposed by [35].

4.3.2 Perturbed case with stiffness perturbation to resonator 3

4.3.2.1 Frequency response

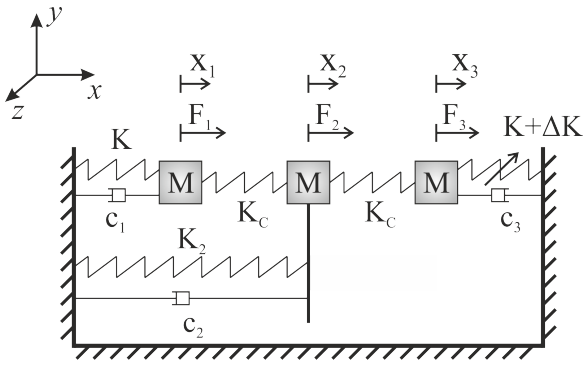

Figure 4.13: A spring-mass-damper model of a balanced 3DoF resonator system perturbed by a stiffness perturbation to resonator 3.

Consider a balanced 3DoF resonator system perturbed with a stiffness perturbation to resonator 3, with $M_1 = M_2 = M_3 = M$, $K_1 = K, K_2 \geq 2K, K_{c1} = K_{c2} = K_c$ and $K_3 = K + \Delta K$, $|\Delta K| \ll K$, as shown in Figure 4.13. Also suppose that the resonator system is weakly coupled, thus Equation 4.5 is satisfied, and is only driven by F_1, and $F_2 = F_3 = 0$.

As for the damping, since the perturbation is weak with $|\Delta K| \ll K$, while the mass is identical, we can assume that the damping of resonator 1 and 3 is the same, $c_1 = c_3 = c$. In addition, it can be demonstrated by equivalent circuit model simulations that the damping of resonator 2 has a negligible effect on the frequency response, i.e. mode frequencies and Q-factor of the in-phase and out-of-phase modes. The values used for the simulation are listed in Table 4.2 and the equivalent circuit model for this simulation in PSpice is presented in Figure 4.14. The schematic is identical to Figure 4.12, except that only V_1 was used as assumed, and that large resistors were used in parallel to $C_{1,2,3}$

for convergence of the simulation. The coupling capacitors used were negative so that the electrostatic coupling can be modelled.

Table 4.2: Values and conditions for the simulations varying damping of resonator 2

Component	Values	Mechanical model equivalent
L	0.489MH	M
C	0.254fF	K
C_2	84.8aF	$K_2/K = 3$
C_c	-19.07fF	$K/K_c = -75, \gamma_3 = 11174$
R	0.44MΩ	c, $Q = 100$k
R_2	0.44MΩ 44MΩ	$c_2 = c$ $c_2 = 100c$
ΔC	0fF -0.25pF	$\Delta K = 0$ $\Delta K/K = -1 \times 10^{-3}$

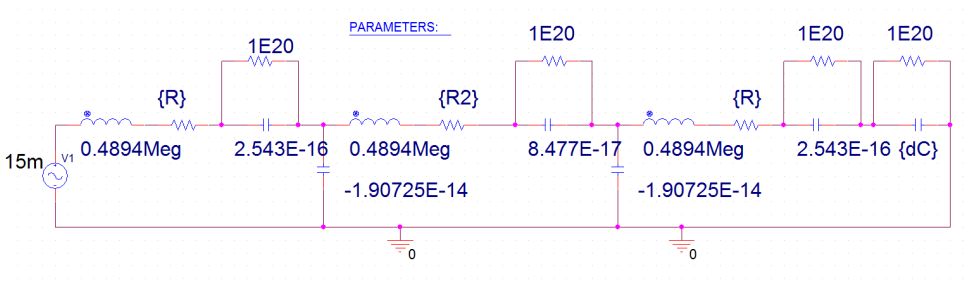

Figure 4.14: Equivalent circuit model schematic used for simulation in PSpice for simulations with perturbations to resonator 3.

It can be seen from Figure 4.15 that by increasing the damping of resonator 2 by two orders of magnitude, the change in the mode frequencies and the Q-factors are less than 1%, which can be neglected. Therefore, for the simplicity of the following analysis, we shall assume that $c_1 = c_2 = c_3 = c$. The transfer functions can be written as:

$$H_1(s) = Ms^2 + cs + (K + K_c) \tag{4.40}$$

$$H_2(s) = Ms^2 + cs + (K_2 + 2K_c) \tag{4.41}$$

$$H_3(s) = Ms^2 + cs + (K + K_c + \Delta K) \tag{4.42}$$

Due to damping, the quality factor will be a finite value, hence leading to a finite bandwidth of each mode. When one mode is in close vicinity to the other, the modes will interfere with each other, therefore mode aliasing occurs. To illustrate the effect of mode aliasing, a simulation using the RLC equivalent circuit as shown in Figure 4.12 was run. A quality factor of the modes of $Q = 5000$ in vacuum was assumed; this is a conservative estimation compared to similar resonant devices [39, 112]. The conditions and values

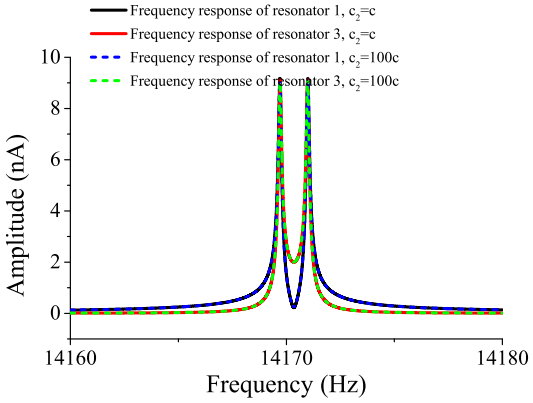

(a) $\Delta K/K = 0$

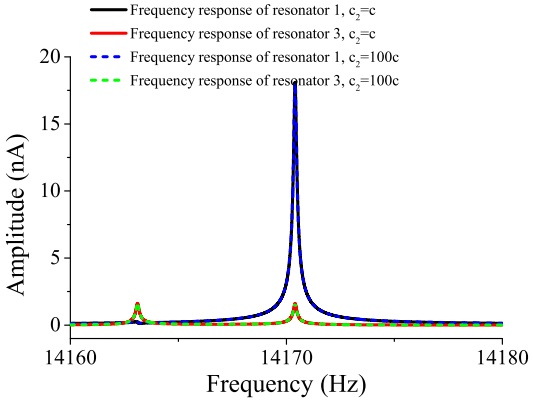

(b) $\Delta K/K = -1 \times 10^{-3}$

Figure 4.15: Demonstration that the damping of resonator 2 has a negligible effect on the frequency response of the in-phase and out-of-phase modes: a) without perturbation; b) with stiffness perturbation to resonator 3, $\Delta K/K = -1 \times 10^{-3}$. It can be seen that increasing the damping of resonator 2 by 100 times does not significantly change the frequency responses of resonators 1 and 3 of the in-phase and out-of-phase modes.

used for the simulations are listed in Table 4.3. Four simulations were performed for varying values of $\gamma_3, K/K_c$ and $\Delta K/K$; the frequency response of the resonators 1 and 3 measured by the motional currents with 15mV driving voltage are shown in Fig. 4.16. Comparing Fig. 4.16(a), 4.16(b), 4.16(c) and 4.16(d), it is noticed that when the mode frequency difference decreases, the mode aliasing becomes more severe, eventually resulting in merged modes for one resonator (Fig. 4.16(b)) and both resonators (Fig. 4.16(c)). The difficulty in identifying the mode of interest, i.e. the out-of-phase mode, in case of severe mode aliasing (e.g. as shown in Fig. 4.16(c)) can lead to the sensor being unable to operate as intended. To avoid severe mode aliasing, an anti-aliasing condition should be satisfied:

$$\Delta\omega > 2 \times \Delta\omega_{3\text{dB}} \tag{4.43}$$

Table 4.3: Values and conditions for the simulations demonstrating mode aliasing

Simulation	Component values	Mechanical model equivalent
a) to d)	$L = 0.489$MH $C = 0.254$fF $C_2 = 84.8$aF $R = 8.77$MΩ	M K $K_2/K = 3$ $Q = 5000$
a)	$C_c = -3.81$fF, $\Delta C = 0$fF	$K/K_c = -15$, $\gamma_3 = 435$, $\Delta K/K = 0$
b)	$C_c = -12.72$fF, $\Delta C = 0$fF	$K/K_c = -50$, $\gamma_3 = 4950$, $\Delta K/K = 0$
c)	$C_c = -19.07$fF, $\Delta C = 0$fF	$K/K_c = -75$, $\gamma_3 = 11174$, $\Delta K/K = 0$
d)	$C_c = -19.07$fF, $\Delta C = -0.17$pF	$K/K_c = -75$, $\gamma_3 = 11174$, $\Delta K/K = -1.5 \times 10^{-3}$

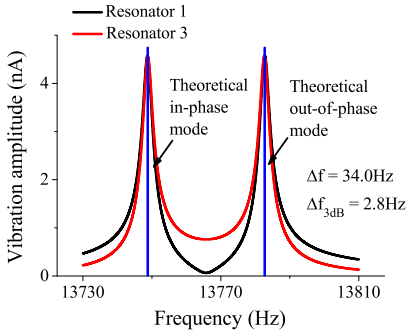

(a) $\gamma_3 = 435$, $\Delta K/K = 0$

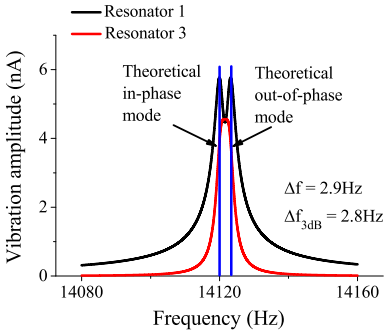

(b) $\gamma_3 = 4950$, $\Delta K/K = 0$

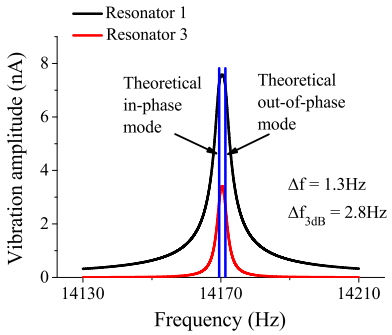

(c) $\gamma_3 = 11174$, $\Delta K/K = 0$

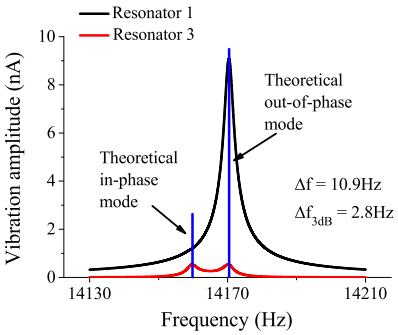

(d) $\gamma_3 = 11174$, $\Delta K/K = -1.5 \times 10^{-3}$

Figure 4.16: Simulated frequency responses resonators 1 and 3 using and equivalent electrical RLC network model (as shown in Figure 4.12) with a quality factor of 5000 and varying parameters: a) $\gamma_3 = 435$, $\Delta K/K = 0$, b) $\gamma_3 = 4950$, $\Delta K/K = 0$, c) $\gamma_3 = 11174$, $\Delta K/K = 0$, d) $\gamma_3 = 11174$, $\Delta K/K = -1.5 \times 10^{-3}$. The theoretically calculated frequency difference and the 3dB bandwidth of the modes are also shown in the figure. The mode distortion caused by the mode aliasing effect can be seen in b) and c); this is due to the relatively small frequency difference between the in-phase and out-of-phase modes. The mode aliasing effect reduces for larger mode frequency differences.

Once the anti-aliasing condition is fulfilled, and assuming weak coupling (Equation 4.13), the mode frequencies with damping can be approximated using Equations 4.20 and 4.22.

This is verified by simulations using equivalent RLC circuit. The values used for the simulation are listed in Table 4.4.

Table 4.4: Values used in the simulation to demonstrate the mode frequencies with damping

Component	Value	Mechanical model equivalent
L	0.489MH	M
C	0.254fF	K
C_2	84.8aF	$K_2/K = 3$
C_c	-19.07fF	$K/K_c = -75$, $\gamma_3 = 11174$
R	8.77MΩ	$Q = 5000$

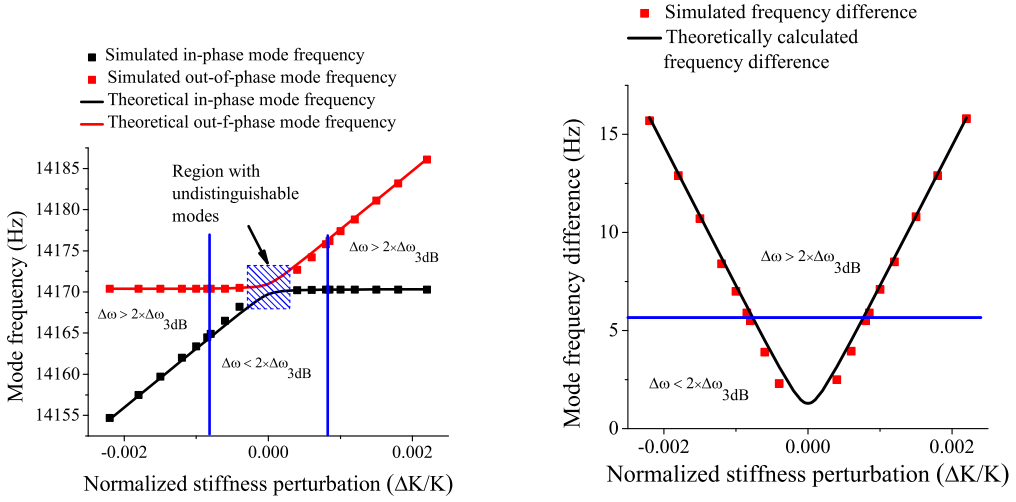

(a) Mode frequency with damping

(b) Mode frequency difference with damping

Figure 4.17: Simulation results showing the in-phase and out-of-phase mode frequencies as a function of normalized stiffness: a) simulated with a quality factor of 5000, and theoretically calculated mode frequencies using Equations 4.20 and 4.22; b) simulated and calculated mode frequency difference, $\Delta\omega = \omega_{op} - \omega_{ip}$. The blue lines in both figures mark the boundary of $\Delta\omega = 2 \times \Delta\omega_{3dB}$. Regions where the anti-aliasing condition is satisfied are marked in both figures. The blue shaded area in a) shows the region where mode aliasing is so severe that the in-phase and out-of-phase modes cannot be differentiated. The theoretically calculated mode frequencies match well with simulated values, however, the error tends to grow when the frequency difference decreases in value.

As demonstrated in Fig. 4.17, Equations 4.20 and 4.22 can still be regarded as accurate estimations of mode frequencies for $\Delta\omega \geq 2 \times \Delta\omega_{3dB}$, with relative errors less than 25ppm. Therefore, for the following analysis, we shall use Equations 4.20 and 4.22 for the out-of-phase and in-phase mode frequencies.

4.3.2.2 Mode localization

For the case with damping, the symmetry of the amplitude ratios at the in-phase and out-of-phase mode frequencies, shown in Figure 4.5 is still valid. This can be demonstrated in Figure 4.18. Hence, without loss of generality, we shall analyse the amplitude ratio of the out-of-phase mode in this section. In addition, for sensors to achieve high sensitivity, a branch with higher slope is chosen, in this case, $\Delta K < 0$ as shown in Figure 4.18.

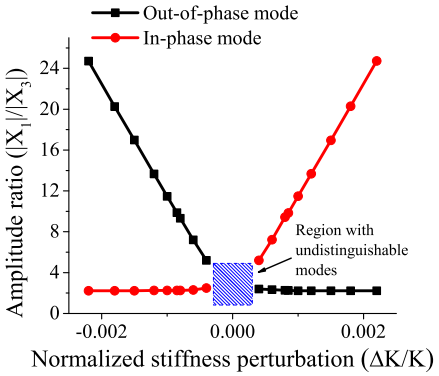

Figure 4.18: Demonstration of the symmetry of the amplitude ratios at the in-phase and out-of-phase mode frequencies.

Suppose the system is driven only by F_1 and $F_2 = F_3 = 0$, when the anti-aliasing condition (Equation 4.43) and weak coupling assumption (Equation 4.13) is satisfied, we can approximate the displacement and velocity amplitude ratio at the out-of-phase mode frequency, for negative $\Delta K < 0$, as:

$$\begin{aligned}\left|\frac{U_1(j\omega_{\text{op}})}{U_3(j\omega_{\text{op}})}\right| = \left|\frac{X_1(j\omega_{\text{op}})}{X_3(j\omega_{\text{op}})}\right| = \left|\frac{H_{11}(s)}{H_{31}(s)}\right| = \left|\frac{H_2(s)H_3(s) - K_c^2}{K_c^2}\right| \\ \approx \left|\frac{\gamma_3(\Delta K/K) - \sqrt{\gamma_3^2(\Delta K/K)^2 + 4}}{2} + j\frac{\gamma_3}{Q}\right|\end{aligned} \tag{4.44}$$

To verify Equation 4.44, the same simulation as in the previous section was run, with electrical circuit parameters listed in Table 4.5. The stiffness perturbations are chosen so that the condition of anti-aliasing is fulfilled.

It can be seen from Fig. 4.19 that the simulated results agree well with Equation 4.44, with relative error smaller than 1%. Therefore, Equation 4.44 can be considered as an accurate estimation of amplitude ratio with damping when the anti-aliasing condition is satisfied.

It can be seen from the mathematical expression that the amplitude ratio with damping is larger than that without any damping. Furthermore, the phase difference between the two resonators can be modified by the finite Q-factor because of damping. However,

Table 4.5: Values used in the simulation to demonstrate the amplitude ratios with damping

Component	Value	Mechanical model equivalent
L	0.489MH	M
C	0.254fF	K
C_2	84.8aF	$K_2/K = 3$
C_c	-12.72fF	$K/K_c = -50$, $\gamma_3 = 4950$
	-19.07fF	$K/K_c = -75$, $\gamma_3 = 11174$
R	8.77MΩ	$Q = 5000$

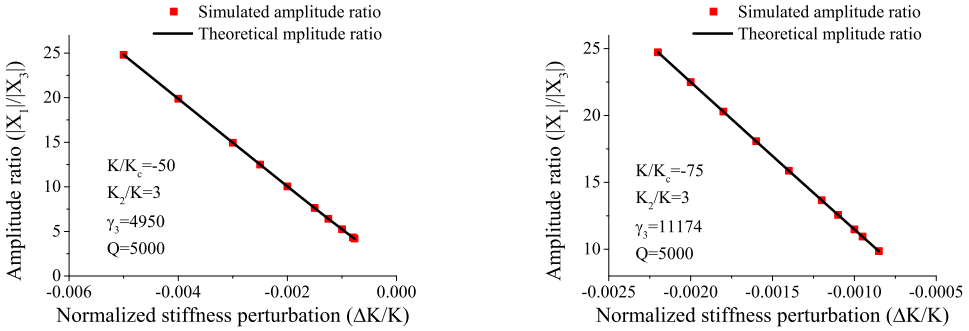

(a) $\gamma_3 = 4950$ (b) $\gamma_3 = 11174$

Figure 4.19: Simulated amplitude ratios together with the amplitude ratios calculated according to Equation 4.44 and a quality factor of $Q = 5000$.

it can be noticed that the effect of a given damping can be reduced by increasing the amplitude ratio value without damping. This will be elaborated in later chapters.

4.3.3 Other perturbed cases

a) Stiffness perturbation to resonator 1: due to the symmetry of resonator 1 and 3, the behaviour of the system of the perturbed case with a negative stiffness perturbation $\Delta K < 0$ introduced to resonator 1, and driven only by F_3, $F_1 = F_2 = 0$ can be analysed by a similar approach. The mode frequencies can still be approximated by Equations 4.20 and 4.22. When anti-aliasing condition is satisfied, the amplitude ratio of the out-of-phase mode, for the negative $\Delta K < 0$ can be approximated by:

$$\begin{aligned}\left|\frac{U_3(j\omega_{\text{op}})}{U_1(j\omega_{\text{op}})}\right| = \left|\frac{X_3(j\omega_{\text{op}})}{X_1(j\omega_{\text{op}})}\right| = \left|\frac{H_{33}(s)}{H_{13}(s)}\right| = \left|\frac{H_1(s)H_2(s) - K_c^2}{K_c^2}\right| \\ \approx \left|\gamma_3(\Delta K/K) - \frac{\sqrt{\gamma_3^2(\Delta K/K)^2 + 4}}{2} + j\frac{\gamma_3}{Q}\right|\end{aligned} \tag{4.45}$$

b) Stiffness perturbation to both resonators 1 and 3: now consider the balanced 3DoF resonator system is perturbed with ΔK_1 to resonator 1, and a negative perturbation $\Delta K_3 < 0$ to resonator 3. A similar approach as shown in Section 4.2.4 by defining $K' = K + \Delta K_1$ is used. Hence the effective stiffness perturbation to resonator 3 is $\Delta K' = \Delta K_2 - \Delta K_1$.

Now substitute K' for K and $\Delta K'$ for ΔK into the transfer functions (Equations 4.40 to 4.42), and follow the same procedure as shown in Section 4.3.2, assuming $|\Delta K_1| < |\Delta K_2| \ll K$ and anti-aliasing condition is satisfied, we can obtain the mode frequencies and the amplitude ratio at the out-of-phase mode frequency:

$$\omega_{\text{op}} \approx \sqrt{\frac{1}{M}\left[K' + K_c + \frac{1}{2}(\Delta K' - \alpha + \sqrt{\Delta K'^2 + \alpha^2})\right]} \tag{4.46a}$$

$$\omega_{\text{ip}} \approx \sqrt{\frac{1}{M}\left[K' + K_c + \frac{1}{2}(\Delta K' - \alpha - \sqrt{\Delta K'^2 + \alpha^2})\right]} \tag{4.46b}$$

$$\left|\frac{U_1(j\omega_{\text{op}})}{U_3(j\omega_{\text{op}})}\right| = \left|\frac{X_1(j\omega_{\text{op}})}{X_3(j\omega_{\text{op}})}\right| \approx \left|\frac{\gamma_3(\Delta K'/K) - \sqrt{\gamma_3^2(\Delta K'/K)^2 + 4}}{2} + j\frac{\gamma_3}{Q}\right| \tag{4.46c}$$

where

$$\delta K' = \frac{\Delta K'}{K} = \frac{\Delta K_2 - \Delta K_1}{K} \tag{4.47}$$

To verify the modal behaviour of the 3DoF weakly coupled resonator system (Equations 4.46b, 4.46b and 4.46c), a simulation with equivalent RLC circuit model was run. The values used in the simulation were the same as listed in Table 4.4. In addition, a constant stiffness perturbation $\Delta K_2/K = -0.001$ was introduced to resonator 3. The stiffness perturbation to resonator 1 $\Delta K_1/K$ was varied, and was in fact identical to the normalized stiffness perturbations in the following figures. The mode frequencies and amplitude ratios were depicted in Figure 4.20(a) and Figure 4.20(b), respectively. It can be seen from the figures that the theoretical estimations can be regarded accurate, with relative errors smaller than 0.2% for amplitude ratios and 0.003% for mode frequencies.

It can be seen from the simulations with damping that the concept of setting the operating point, as discussed in Section 4.2.4, can also be used for practical cases with damping. It should be pointed out that by intentionally introducing a bias stiffness perturbation, ΔK_2 to resonator 3 in this case, the regions with undistinguishable modes was translated (comparing Figure 4.20(a) to Figure 4.17(a)), allowing the extension of the dynamic range. This will be discussed further later in Section 6.5.2.

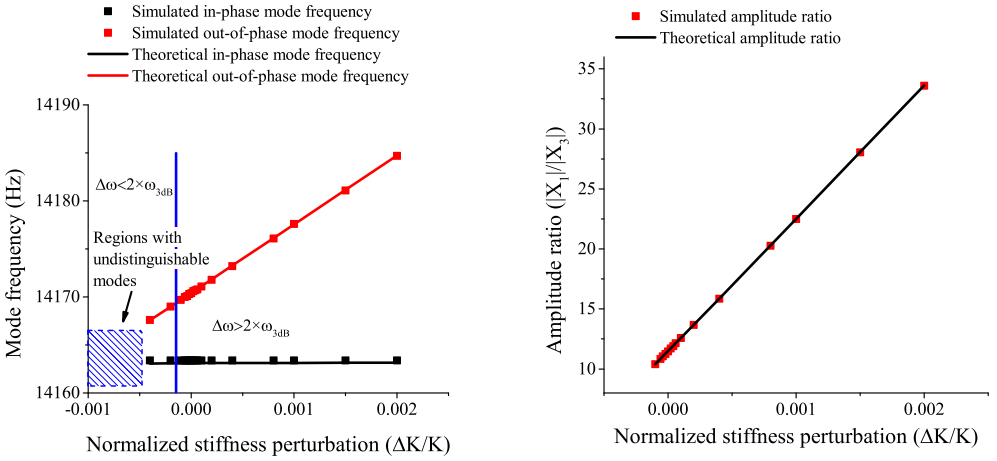

(a) Mode frequencies (b) Amplitude ratios

Figure 4.20: Simulated values together with the theoretical values calculated according to Equations 4.46b, 4.46b and 4.46c, for stiffness perturbations to both resonator 1 and 3, of: a) mode frequencies and b) amplitude ratios.

4.4 FEM simulations

To verify the theoretical calculations for MEMS resonators, a 3DoF weakly coupled resonator device was built and simulated in Coventorware. The 3DoF resonator device used in the simulation is demonstrated in Figure 4.21.

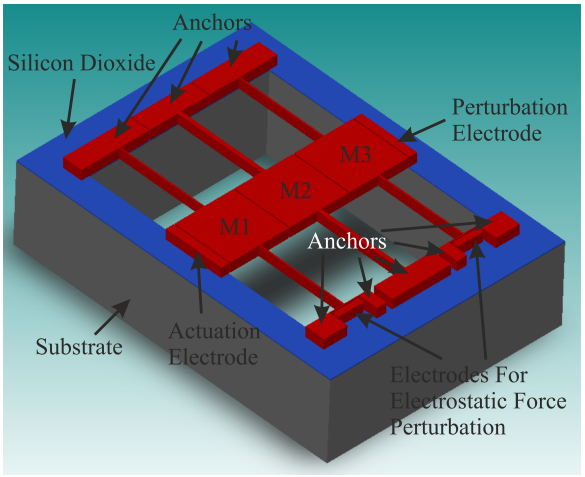

Figure 4.21: A 3DoF resonator device used in the FEM simulations. M1, M2 and M3 indicate three proof masses of three resonators separated by air gaps. The coupling is realized through electrostatic springs, and actuation is realized through capacitive forces.

For this verification purpose, the choice of the design parameters of the device were arbitrary. The parameters of the device is listed in Table 4.6.

Table 4.6: Dimensions of the device

Parameter	Design Value	Unit
Device layer thickness	50	μm
Suspension beam lengths (resonator 1, 2 and 3)	450	μm
Suspension beam width (resonator 1 and 3)	7	μm
Suspension beam width (resonator 2)	19	μm
Gaps between resonators	6	μm
Gaps between resonator and electrode	6	μm
Proof mass	300×300	$(\mu m)^2$
Tether length	150	μm
Electrode for force perturbation overlap	130	μm

In the simulations, nonlinearity of the mechanical springs was excluded to ensure linear springs. To couple the resonators, a DC voltage of 80V was applied to resonators 1 and 3, while resonator 2 was grounded. This created a $K/K_c \approx 15$, satisfying weak coupling conditions.

Stiffness perturbation was realized through two ways, one is axial electrostatic force, as shown by Equation 3.5b; the other one is spring softening by applying a DC voltage on the perturbation electrode. This is to demonstrate that the stiffness perturbation can be introduced by both approaches.

4.4.1 Mode localization

To demonstrate the mode localization, a mode analysis was performed. For this simulation, an extra pulling electrostatic force was applied to resonator 1, so that a $\Delta K > 0$ was introduced to resonator 1. Before applying the electrostatic force, resonators 1 and 3 are completely identical. At the out-of-phase mode frequency, as shown in the balanced situation in Figure 4.22, the vibration amplitudes of resonators 1 and 3 are identical. After applying the electrostatic force to resonator 1, the elastic energy was localized to resonator 1, leading to a larger vibration amplitude of resonator 1 compared to resonator 3, mode localization occurred, as shown in the Figure 4.22.

4.4.2 Modal behaviour without damping

To demonstrate the vibration behaviour of the resonators without damping of a 3DoF weakly coupled MEMS resonator device, an extra electrostatic force was applied to

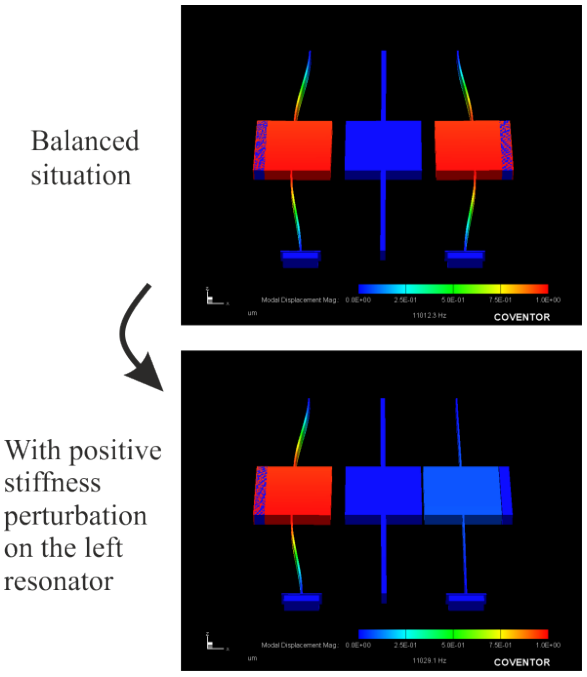

Figure 4.22: Demonstration of mode localization effect of a 3DoF resonator device in FEM simulations. After introducing an electrostatic tensile force to resonator 1, the balance of the 3DoF device was broken, leading to energy localization to resonator 1, mode localization occurred.

resonator 1 to introduce a positive $\Delta K > 0$ to resonator 1. The simulated vibration amplitude ratio X_1/X_3, as well as mode frequencies of the in-phase and out-of-phase modes, as a function of the normalized stiffness perturbation are plotted in Figures 4.23(a) and 4.23(b), respectively. The theoretical amplitude ratios, out-of-phase and in-phase mode frequencies were calculated using Equation 4.27, Equation 4.26 and Equation 4.28, respectively, and plotted in the figures as well.

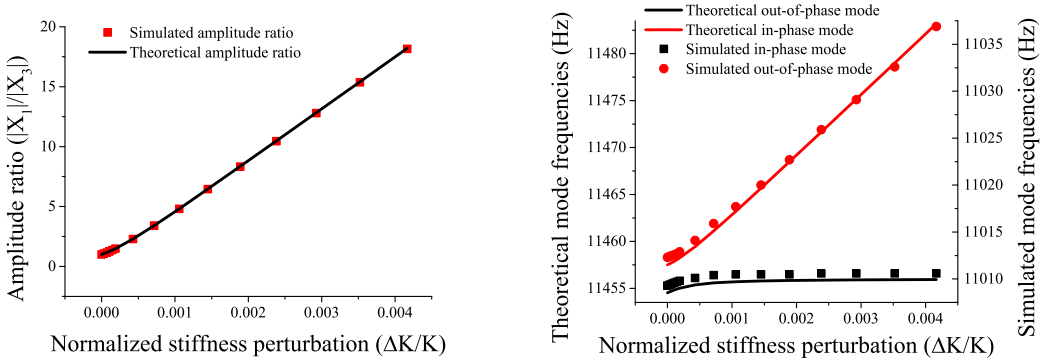

(a) Amplitude ratio

(b) Mode frequencies

Figure 4.23: Simulated amplitude ratio and mode frequencies together with the theoretically calculated values assuming no damping, as a function of positive stiffness perturbations to resonator 1.

It can be seen from Figure 4.23 that the simulated results agreed well with the theoretical calculations, with relative errors less than 1% for amplitude ratios and 4% for mode frequencies, indicating that the theoretical estimations are accurate. It should be noticed that the mode frequencies simulated by FEM tool were smaller than theoretical values. This may be caused by the elastic energy stored in the anchor.

From the simulations, it can be seen that for a normalized stiffness perturbation of $\Delta K/K \approx 0.0042$, which corresponded to an electrostatic force of 46μN, the change in the out-of-phase mode frequency was approximately $24.6/11012.3 = 0.22\%$, while the change in amplitude ratio was 18.15, which was over three orders of magnitude more drastic than the change in mode frequency. Therefore it can be concluded that by using amplitude ratio as output, for this device, the improvement in sensitivity can reach three orders of magnitude. Therefore, it can be seen that this resonator device can be used for high sensitivity force sensing applications.

4.4.3 Modal behaviour with damping

For this simulation, no extra electrostatic force was applied in the axial direction of the beam. Instead, a DC voltage was applied to the perturbation electrode, causing a softening stiffness perturbation $\Delta K < 0$ to resonator 3. In addition, damping was introduced, leading to a $Q = 5000$, identical to the previous simulations using an electrical RLC circuit.

Due to the limited bandwidth of the modes, mode aliasing should occur if the mode frequency difference does not satisfy the anti-aliasing condition. To demonstrate this, a frequency response was simulated. An arbitrary AC drive voltage was applied to the actuation electrode. The simulated frequency response is shown in Figure 4.24.

After ensuring mode aliasing was insignificant by altering the DC voltage on the perturbation electrode, amplitude ratio and mode frequencies as a function of normalized stiffness perturbation were plotted in Figures 4.25(a) and 4.25(b), respectively. Theoretical amplitude ratios, mode frequencies of the out-of-phase and in-phase modes were calculated using Equation 4.44, Equation 4.26 and Equation 4.28, respectively, and plotted in Figure 4.25 for comparison.

It can be seen that outside of the area with strong mode aliasing, the simulated results agreed well with the theoretical calculations, indicating accurate theoretical estimations. Similar to the previous simulations, it was demonstrated that, for the same stiffness perturbation, the change in amplitude ratio was three orders of magnitude more responsive than the mode frequency shifts. For instance, as shown in Figure 4.25(b), for a change in $\Delta K/K$ of 0.00175, the change of normalized frequency $(\Delta\omega/\omega)$ is approximately

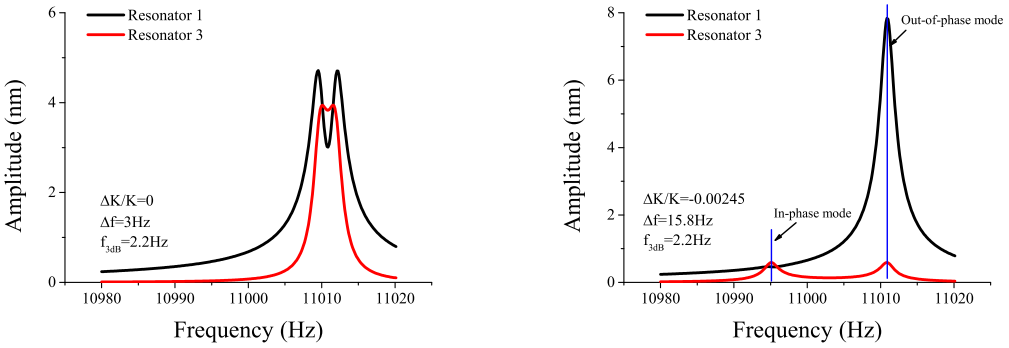

(a) $\Delta K/K = 0$ (b) $\Delta K/K = -0.00245$

Figure 4.24: Simulated frequency responses: a) without stiffness perturbation; b) with negative $\Delta K/K = -0.00245$ stiffness perturbation to resonator 3. It can be seen that without any stiffness perturbation, strong mode aliasing occurred since $\Delta f < 2f_{3\text{dB}}$, out-of-phase mode and in-phase mode were difficult to distinguish; whereas when mode aliasing was reduced with $\Delta K/K = -0.00245$, out-of-phase mode can be distinguished, since anti-aliasing condition $\Delta f > 2f_{3\text{dB}}$ was satisfied.

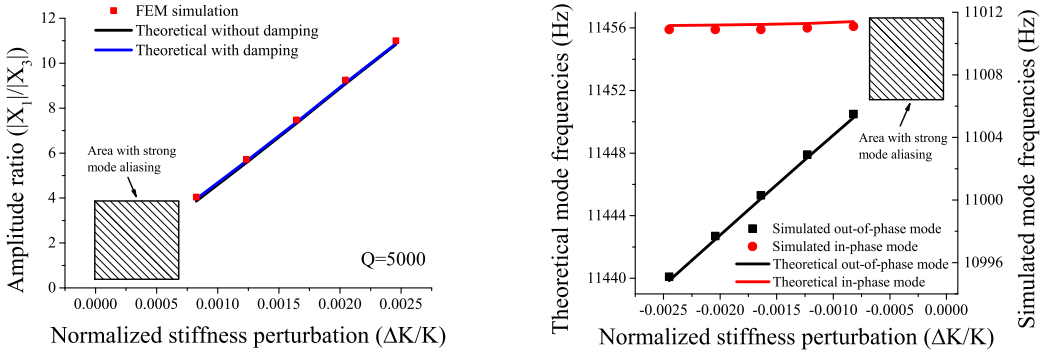

(a) Amplitude ratio (b) Mode frequencies

Figure 4.25: Simulated amplitude ratio and mode frequencies together with the theoretically calculated values with limited Q-factor of $Q = 5000$, as a function of negative stiffness perturbations to resonator 3.

9.18×10^{-4}; whereas for the same amount of change in $\Delta K/K$, the change in normalized output (amplitude ratio X_1/X_3) is approximately 7.5, as shown in Figure 4.25(a). Hence, the improvement in normalized sensitivity is over three orders of magnitude.

4.5 Summary

In this chapter, we have analysed the vibrational behaviour of a 3DoF resonator systems in theory, with and without damping. For the analysis without damping, we have

used algebraic method; whereas for the analysis with damping, we have used a transfer function method.

As can be seen from the analysis, when a stiffness perturbation is introduced into the system, namely to resonator 1 or/and 3, the mode frequencies and the amplitude ratio of the in-phase and out-of-phase modes changes with the stiffness perturbation. The changes in mode frequencies and amplitude ratios can be accurately predicted by our theoretical formulas provided that weak coupling is satisfied.

In addition, it can be concluded from the discussion in this chapter, that amplitude ratios have the following advantages: (a) ability to detect the position of the perturbation and (b) capability of common mode rejection.

Furthermore, damping was included in the analysis. It was demonstrated that mode aliasing can occur when the in-phase and out-of-phase modes are too close to each other. This should be avoided for sensor implementation, as strong mode aliasing can potentially lead to inability of identifying the mode of interest. It was also demonstrated that the mode aliasing was reduced as the frequency difference between the two modes increased. This will aid us in the MEMS sensor design to minimize mode aliasing.

Chapter 5

3DoF Weakly Coupled Resonators as a Sensor

5.1 Introduction

From the vibrational behaviour analysis, it was shown that the amplitude ratio change was more significant compared to the mode frequency shifts, when a stiffness perturbation was introduced to a 3DoF weakly coupled resonator device. In addition, in the discussion in Chapter 4, we have demonstrated, in theory, the common mode rejection and position detection capabilities by measuring mode shape changes instead of frequency shift. This demonstrated that a 3DoF resonator device, as shown in Figure 5.1 as an example, could be an alternative to the conventional single resonator sensor, but with much improved sensitivity, common mode rejection and position detection capabilities.

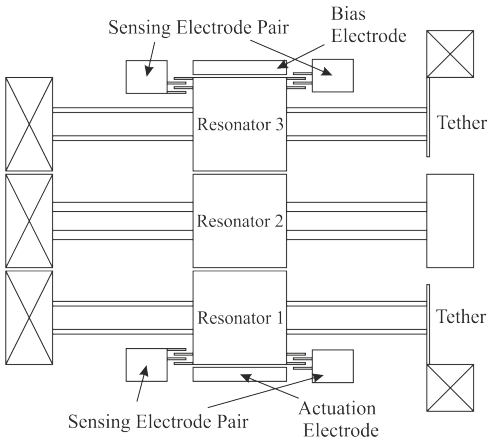

Figure 5.1: An example 3DoF weakly electrostatically coupled resonator sensor.

However, the output metrics have not yet been compared, thus an optimum output is yet to be proposed. Furthermore, other important performance specifications have not been discussed for this type of sensor, such as dynamic range. Therefore, in this chapter,

we shall discuss in theory the output metrics, in addition to the practical specification of the sensor, namely the dynamic range, linear sensitivity, nonlinearity and noise floor. The discussion may be helpful for future device optimization.

5.2 Dynamic range

For the 3DoF resonator sensor in Figure 5.1, as shown in Figure 4.16, the frequency difference between the in-phase and out-of-phase mode is dependent on both γ_3 and $\Delta K/K$. Therefore, for a given quality factor and γ_3 value, due to the mode aliasing, the anti-aliasing condition (Equation 4.43) sets a boundary for the maximum stiffness perturbation. Perturbation values beyond the boundary potentially result in severe mode aliasing effects as shown in Figure 4.16(c).

It was also demonstrated in Figure 4.17 that, Equations 4.20 and 4.22 can still be regarded as accurate estimations of mode frequencies for $\Delta\omega \geq 2 \times \Delta\omega_{3\text{dB}}$, with relative errors less than 25ppm. Neglecting this small error, the difference between the in-phase and out-of-phase modes can be expressed as:

$$\Delta\omega = \omega_{\text{op}} - \omega_{\text{ip}} \approx \sqrt{\frac{K}{M}}\sqrt{\left(\frac{\Delta K}{2K}\right)^2 + \left(\frac{1}{\gamma_3}\right)^2} \tag{5.1}$$

The 3-dB bandwidth, for a given finite quality factor Q, is given as:

$$\Delta\omega_{3\text{dB}} = \frac{1}{Q}\sqrt{\frac{K}{M}} \tag{5.2}$$

Substituting Equations 5.1 and 5.2 into Equation 4.43, and rearranging:

$$\left(\frac{\Delta K}{K}\right)^2 > \left(\frac{4}{Q}\right)^2 - \left(\frac{2}{\gamma_3}\right)^2 \tag{5.3}$$

Therefore, for negative perturbations $\Delta K/K < 0$ (to either resonator 1 or 3), and for $\gamma_3 \geq Q/2$, the upper boundary of the dynamic range of the sensor is found to be:

$$\frac{\Delta K}{K} < -2\sqrt{\left(\frac{2}{Q}\right)^2 - \left(\frac{1}{\gamma_3}\right)^2} \tag{5.4}$$

This equation makes sure that all $\Delta K < 0$ satisfies the anti-aliasing condition (Equation 4.43), and the regions with undistinguishable modes (as shown in Figures 4.17(a)) can be avoided. For $\gamma_3 < Q/2$, any ΔK will satisfy the anti-aliasing condition. Thus in this situation, the dynamic range will not be limited by the mode aliasing effect.

Furthermore, the noise floor of the device and the interface circuitry sets the minimum detectable amplitude of the resonators; consequently a limitation of the maximum measurable amplitude ratio can be introduced. Thus, the lower boundary of the dynamic range of the device is determined as:

$$\frac{\Delta K}{K} > -\frac{\text{Max Amplitude Ratio}}{\gamma_3} \tag{5.5}$$

Therefore, it can be seen that the value of γ_3 should not be arbitrarily large due to its influence on the dynamic range of the sensor.

5.3 Output metrics

In Chapter 4, the vibrational amplitude ratio X_1/X_3 and mode frequencies change of a 3DoF device subject to a stiffness perturbation was demonstrated. It was shown that, for the same stiffness perturbation, the change in amplitude ratio was orders of magnitude more significant than that of mode frequencies. However, whether the amplitude ratio is the optimum output signal is still to be investigated. In this section, we shall compare different output metrics, namely mode frequency shift, amplitude ratio, eigenstate shift and amplitude difference, in terms of their linear sensitivity and linear range (nonlinearity error less than 5%).

For demonstration purposes, the stiffness perturbations ΔK were introduced to resonator 3 and $\Delta K < 0$. And the amplitudes of the out-of-phase mode were chosen due to the symmetry of the in-phase and out-of-phase modes.

Due to the complexity in calculating eigenstate shift and amplitude difference analytically, we shall extract the linear sensitivity and linear range from simulation results. The simulation was run using the equivalent electrical circuit model as shown in Figure 4.12. The values used for the simulation are listed in Table 5.1, so that they are close to the values used in the experiment. The motional current amplitudes were used in the simulations to represent the velocity amplitudes of each resonator.

Table 5.1: Values used in the simulation to verify theoretical estimations

Component	Value	Mechanical model equivalent
L	0.397MH	M
C	0.318fF	K
C_2	87.6aF	$K_2/K = 3.6$
C_c	-9.09fF	$K/K_c = -28.6$, $\gamma_3 = 2117$
R	0.57MΩ	$Q = 6000$
v_{ac}	8mV	Actuation voltage to match with experiment

5.3.1 Mode frequency

From the simulation values used, it can be seen that all $\Delta K \leq 0$ shall be within the dynamic range. Hence we are able to approximate the mode frequencies using Equations 4.20 and 4.22. From Figure 4.5, it can be seen that for negative stiffness perturbations to resonator 3, the frequency of the in-phase mode is more responsive than that of the out-of-phase mode. Hence here we shall only consider the mode frequency of the in-phase mode.

From fundamental mathematics, it can be seen that for large ΔK, the in-phase mode frequency is a linear function, and the linear scale function can be approximated as:

$$\frac{\Delta f_{\text{ip}}}{f_0} \approx \frac{1}{2}\frac{\Delta K}{K} \tag{5.6}$$

where,

$$f_0 = \frac{1}{2\pi}\sqrt{\frac{K}{M}} \tag{5.7}$$

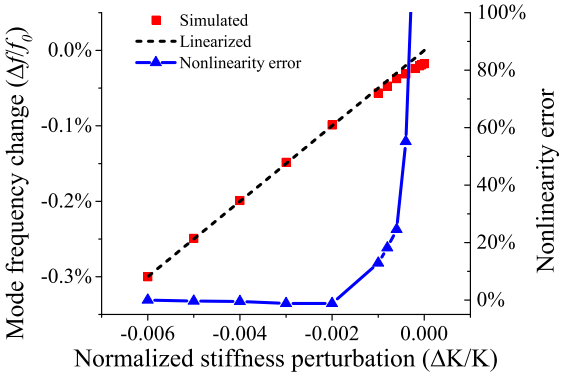

Figure 5.2: Linearized (black) and simulated (red) in-phase mode frequency, as well as the nonlinearity error, as a function of normalized stiffness perturbations. The nonlinearity error decreased as the normalized stiffness perturbation increased in absolute value.

It can be seen from Figure 2 that the nonlinearity error decreased as the normalized stiffness perturbation increased in absolute value. For $\Delta K/K < -0.002$, the nonlinearity error was less than 2%, which can be regarded as negligible. Hence, the linear sensitivity was -0.5 for normalized stiffness perturbations $\Delta K/K < -0.002$.

5.3.2 Vibration amplitude ratio

From the derivations in Appendix A, we are able to approximate the amplitude ratios of $|X_2|/|X_1|$ and $|X_2|/|X_3|$. The theoretical and simulated values are plotted in Figure 5.3.

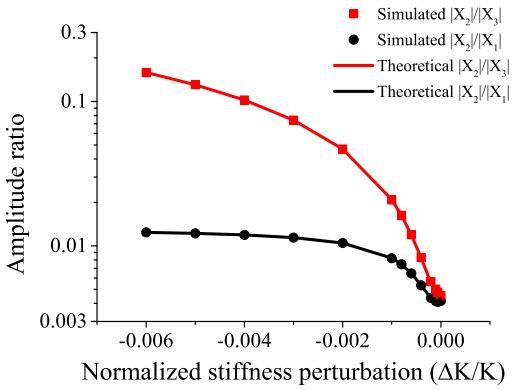

Figure 5.3: Simulated and theoretically estimated amplitude ratio of $|X_2|/|X_1|$ and $|X_2|/|X_3|$. It demonstrates that the vibration amplitude of resonator 2 is orders of magnitude lower than that of either resonator 1 or 3 at the out-of-phase mode frequency.

It can be seen from Figure 5.3 that the amplitude of resonator 2 is at least an order of magnitude lower than either resonator 1 or 3. It should be pointed out that, typically, the motional current of resonator 1 is in the sub-nA region [1]. Therefore, the amplitude of resonator 2 is in the 1pA range or less, thus is more difficult to detect in practice. Hence, the amplitude ratios involving resonator 2 are not practical in real applications, thus are neglected from the amplitude ratio analysis.

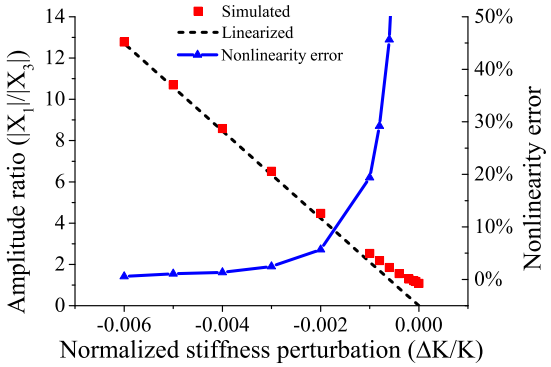

Figure 5.4: Linear (black) and simulated (red) amplitude ratios, $|X_1/X_3|$, as a function of normalized stiffness perturbations, as well as the nonlinearity error. It can be seen that the nonlinearity error decreased as the absolute value of $\Delta K/K$ increases.

[1] This is calculated by dividing the output voltage amplitude measured (as shown in Figure 6.12) by the current to voltage gain of the electrical circuit, which is $1.32G\Omega$

The expression of the amplitude ratio $|X_1|/|X_3|$ at the out-of-phase mode frequency was derived and given by Equation 4.44. For comparison purposes, the theoretical and simulated amplitude ratios for the same scenario as the previous simulations are plotted in Figure 5.4.

The linear sensitivity extracted from the simulated results was 2117, and the linear range for nonlinearity error smaller than 5% was $\Delta K/K < -0.002$.

5.3.3 Eigenstate shift

Eigenstate shift was used in [36, 39] as the output signal for a mode localized sensor. This was derived using a "classical perturbation method" [34]. Despite the fact that calculating the eigenstate shifts requires a larger amount of computation effort compared to simple vibration amplitude or mode frequency shifts, it was demonstrated that it was an accurate prediction of the mode localization effect [34]. Hence, we shall discuss the eigenstate shift as the output signal for a 3DoF weakly coupled resonant sensing device.

It can be seen from Figure 5.3 that the amplitude of resonator 2 is typically orders of magnitude lower than that of either resonator 1 or 3 at the out-of-phase mode frequency. Because of this reason, the vibration amplitude of resonator 2 would have negligible effect in calculating the magnitude of the eigenstates. If excluding the amplitude of resonator 2 completely from the eigenstate calculation, the normalized eigenstates $\mathbf{X}_n$, for a stiffness perturbation ΔK to resonator 3, can be approximated as:

$$\mathbf{X}_n \approx \begin{bmatrix} -\dfrac{\mathrm{AR}}{\sqrt{1+\mathrm{AR}^2}} \\ 0 \\ \dfrac{1}{\sqrt{1+\mathrm{AR}^2}} \end{bmatrix} \tag{5.8}$$

where AR is the amplitude ratio of X_1/X_3, which is defined by Equation 4.44.

Suppose the initial eigenstate without any stiffness perturbations is $\mathbf{X}_{n0}$ at the out-of-phase mode frequency. The eigenstate shift $\boldsymbol{\Delta}\mathbf{X}$ can be expressed as [34]:

$$\boldsymbol{\Delta}\mathbf{X} = \left| \frac{\mathbf{X}_n - \mathbf{X}_{n0}}{\mathbf{X}_{n0}} \right| \tag{5.9}$$

It can be seen from the simulation results that, excluding the amplitude of resonator 2, $|X_2|$, indeed has negligible effect on calculating the eigenstate shift. This is demonstrated by the simulated results shown in 5.5.

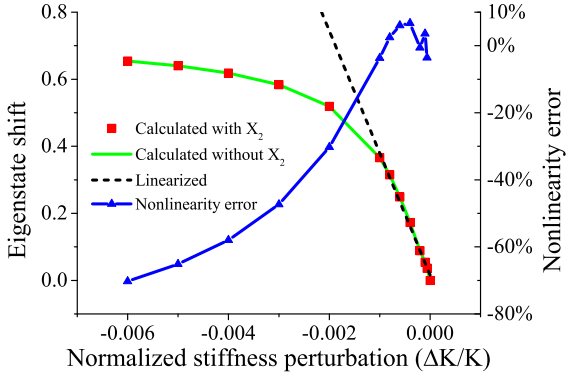

Figure 5.5: Figure showing calculated eigenstate shift from simulated mode amplitude values, as well as a linear fit and nonlinearity error. The eigenstate shifts were calculated including the amplitude of resonator 2, $|X_2|$, (green) and completely neglecting $|X_2|$ (red). No significant differences were noticed, indicating insignificant impact of resonator 2.

The linear sensitivity extracted from the simulated results was found to be 380.5, and the linear range with less than 5% nonlinearity error was $-0.001 < \Delta K/K < 0$.

5.3.4 Vibration amplitude difference

Due to the slopes of the curve of X_1 and X_3 having opposite signs for $\Delta K < 0$, as shown by Figures A.1 and A.2, the vibration amplitude difference can provide improved sensitivity. The simulated and linearized amplitude differences are plotted against normalized stiffness perturbations in Figure 5.6. Also plotted in the figure is the nonlinearity error of the amplitude difference as output signal.

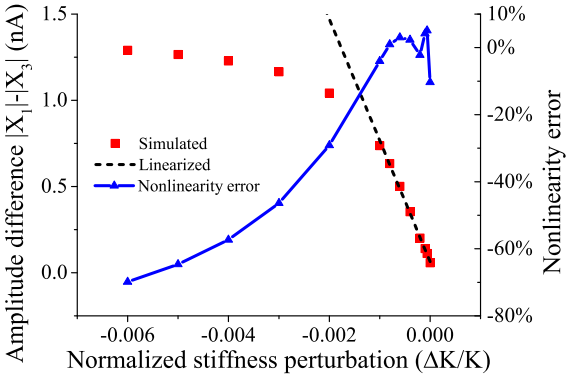

Figure 5.6: Theoretical calculated (black) and simulated (red) vibration amplitude differences between resonators 1 and 3 as a function of normalized stiffness perturbations. The theoretical estimations matched well with simulated values.

The extracted linear sensitivity from the simulation results was 703nA, and the linear range for less than 5% nonlinearity error was $-0.001 < \Delta K < 0$. For the circuit board

in our experiment with 13.2M transimpedance gain and a further 40dB voltage gain, the resulting theoretical linear sensitivity would be 928V.

5.3.5 Summary

Table 5.2: Output metrics summary from simulation results

Output	Linear sensitivity	Linear range (nonlinearity error $< 5\%$)
Frequency shift	0.5	$\Delta K/K < -0.002$
Amplitude ratio ($\lvert X_1\rvert/\lvert X_3\rvert$)	2117	$\Delta K/K < -0.002$
Eigenstate shift	380.5	$-0.001 < \Delta K/K < 0$
Amplitude difference ($\lvert X_1\rvert - \lvert X_3\rvert$)	928V	$-0.001 < \Delta K/K < 0$

To summarize, the linear sensitivity and the linear range of the four different output metrics are listed in Table 5.2. It can be seen from Table 5.2 that the amplitude ratio $|X_1|/|X_3|$ of the out-of-phase mode has the higher linear sensitivity for negative stiffness perturbations to resonator 3, compared to the other output metrics for the mode-localized sensor, such as frequency shift and eigenstate shift. In addition, the amplitude ratio $|X_1|/|X_3|$, as well as the frequency shift, has larger linear range compared to eigenstate shift and amplitude difference. Furthermore, the amplitude ratios are simpler to calculate than the eigenstate shifts, therefore, it requires less computational effort, thus leading to less complicated electronics.

It should be pointed out that amplitude difference $|X_1| - |X_3|$ is another interesting output signal, as it has high sensitivity at the expense of narrow linear range. Moreover, it is also easy to calculate, hence requiring simpler electronics.

To summarize, amplitude ratio $|X_1|/|X_3|$ was the optimum output metric in terms of linear sensitivity and linear range, thus was used in our research as the output signals of the 3DoF weakly coupled resonator sensor.

5.4 Linear sensitivity

For the example 3DoF resonator sensor for stiffness change sensing shown in Figure 5.1, within the dynamic range, assuming the device is perturbed with a negative stiffness perturbation ΔK to resonator 3 and driven from the actuation electrode, we shall restate the expression of amplitude ratio:

$$\begin{aligned}\left|\frac{U_1(j\omega_{\text{op}})}{U_3(j\omega_{\text{op}})}\right| &= \left|\frac{X_1(j\omega_{\text{op}})}{X_3(j\omega_{\text{op}})}\right| = \left|\frac{H_{11}(s)}{H_{31}(s)}\right| = \left|\frac{H_2(s)H_3(s) - K_c^2}{K_c^2}\right| \\ &\approx \left|\frac{\gamma_3(\Delta K/K) - \sqrt{\gamma_3^2(\Delta K/K)^2 + 4}}{2} + j\frac{\gamma_3}{Q}\right|\end{aligned} \tag{5.10}$$

From the electrical RLC simulations results (Figure 4.19), it can be seen that when $|\gamma_3 \Delta K/K| > 10$, the amplitude ratio can be regarded as a linear function of the normalized stiffness perturbations. Mathematically, we can approximate the linearised scale function as:

$$\left|\frac{U_1(j\omega_{\text{op}})}{U_3(j\omega_{\text{op}})}\right| = \left|\frac{X_1(j\omega_{\text{op}})}{X_3(j\omega_{\text{op}})}\right| \approx -\frac{\gamma_3 \Delta K}{K} \tag{5.11}$$

Equation 5.11 is the linearized scaling function of the sensor. The linear sensitivity of the sensor (the ratio of the change in amplitude ratio to the normalized stiffness change) can therefore be expressed by:

$$\mathcal{S}_{3DoF} = \partial \left|\frac{X_1(j\omega_{\text{op}})}{X_3(j\omega_{\text{op}})}\right| \Big/ \partial\left(\frac{\Delta K}{K}\right) = -\gamma_3 \tag{5.12}$$

Thus $-\gamma_3$ is the linear sensitivity of the device.

5.5 Theoretical sensitivity improvement

It is surmised that the linearized scale function, Equation 5.11, can be regarded as a good estimation of the amplitude ratio[2]. Therefore, neglecting the nonlinearity error, the linear sensitivity of the 3DoF resonant sensor, for negative $\Delta K/K$, can be approximated by:

$$\begin{aligned}\mathcal{S}_{3DoF} &= \frac{\partial(\text{Amplitude ratio})}{\partial(\Delta K/K)} = -\gamma_3 \\ &= -\frac{K(K_2 - K + K_c)}{K_c^2}\end{aligned} \tag{5.13}$$

This is the same expression as discussed in Section 2.2.1. The sensitivity to normalized stiffness change of a conventional resonant sensor (i.e. 1DoF) with frequency shift output is given by Equation 5.14 [61]:

[2]The a nonlinearity error is less than 10% for an amplitude ratio larger than 5 from the nonlinearity example simulations shown in later sections, i.e. Section 5.6

$$\mathcal{S}_{1DoF} = \frac{\partial(\text{Relative frequency shift})}{\partial(\Delta K/K)} = \frac{1}{2} \tag{5.14}$$

With the assumptions stated in Equation 4.5, the value for γ_3 is at least 100, thus the improvement in sensitivity is at least two orders of magnitude.

For a 2DoF resonant mode-localized sensor for stiffness change sensing applications, the sensitivity to a stiffness change can be approximated by [39]:

$$\mathcal{S}_{2DoF} = \frac{\partial(\text{Eigenstates shift})}{\partial(\Delta K/K)} \approx \frac{K}{4K_c} \tag{5.15}$$

Given identical K and K_c values, and with the assumption stated in Equation 4.5, comparing Equations 5.13 and 5.15, it is noticed that the sensitivity of a 3DoF resonator sensor is improved by $4(K_2 - K + K_c)/K_c$, which is found to be at least 40 times.

It can be seen from the comparison that the 3DoF mode-localized sensors has the highest sensitivity among the three. The sensitivity improvement is proportional to a key parameter γ_3, which is determined by the stiffness K, K_2 and K_c. The larger value of K/K_c and $(K_2 - K + K_c)/K_c$, the higher sensitivity compared to 1DoF and 2DoF resonant sensors can be achieved.

5.6 Nonlinearity

Despite the fact that the amplitude ratio can be approximated as a linear function of the stiffness change for large normalized stiffness perturbations, from Equation 5.10 it can be seen that the amplitude ratio is a non-linear function of the normalized stiffness perturbation $\Delta K/K$. It can also be seen that the nonlinearity is attributed to: a) the intrinsic nonlinearity of the expression even without the presence of damping; b) the damping due to the γ_3/Q term. Equation 5.10 can therefore be rewritten as:

$$\begin{aligned}\left|\frac{U_1(j\omega_{\text{op}})}{U_3(j\omega_{\text{op}})}\right| = \left|\frac{X_1(j\omega_{\text{op}})}{X_3(j\omega_{\text{op}})}\right| &= \left|-\frac{\sqrt{\gamma_3^2(\Delta K/K)^2+4}-\gamma_3(\Delta K/K)}{2} + j\frac{\gamma_3}{Q}\right| \\ &= -\frac{\gamma_3 \Delta K}{K}(1+\epsilon_1+\epsilon_2)\end{aligned} \tag{5.16}$$

where ϵ_1 is the intrinsic nonlinearity term and ϵ_2 is a second nonlinearity term introduced by damping.

5.6.1 Intrinsic nonlinearity

To theoretically estimate the intrinsic nonlinearity term ϵ_1, we shall assume zero damping and therefore infinite Q-factor. The Taylor expansion of the amplitude ratio without damping can be written as:

$$\begin{aligned}\left|\frac{X_1(j\omega_{\text{op}})}{X_3(j\omega_{\text{op}})}\right|_{Q\to\infty} &= \left|\frac{\gamma_3\Delta K}{K}+\frac{K}{\gamma_3\Delta K}-\left(\frac{K}{\gamma_3\Delta K}\right)^3+\cdots\right| \\ &= -\frac{\gamma_3\Delta K}{K}(1+\epsilon_1)\end{aligned} \tag{5.17}$$

Neglecting all higher order terms, ϵ_1 can be approximated by:

$$\epsilon_1 \approx \left(\frac{K}{\gamma_3\Delta K}\right)^2 \tag{5.18}$$

It can be seen from Equation 5.18 that the nonlinearity error ϵ_1 increases with decreasing value of $(\gamma_3\Delta K/K)^2$.

To demonstrate the influence of the nonlinearity, the same electrical equivalent simulation as in the previous section is run, with varying capacitance C_c, corresponding to K_c in the mechanical model, and thus resulting in different K/K_c and γ_3 values. All the values used in the simulation are listed in Table 4.5, except that $R = 0.44\text{M}\Omega$, resulting in a $Q = 100\text{k}$, which can be regarded as negligible. The results are presented in Figure 5.7.

It can be seen from Figure 5.7 that the amplitude ratio under the assumption of infinite quality factor can be approximated using the linearized scale function (Equation 5.11), with negligible nonlinearity errors (less than 1%) for amplitude ratio larger than 10; however, the nonlinearity error increases as the stiffness perturbation approaches zero. Figures 5.7(a) and 5.7(b) show the results for two exemplary values of γ_3; it can be seen that for the same stiffness perturbation, a larger γ_3 results in better linearity.

Figure 5.7 also indicates that Equation 5.18 can be regarded as an accurate estimation of the nonlinearity error.

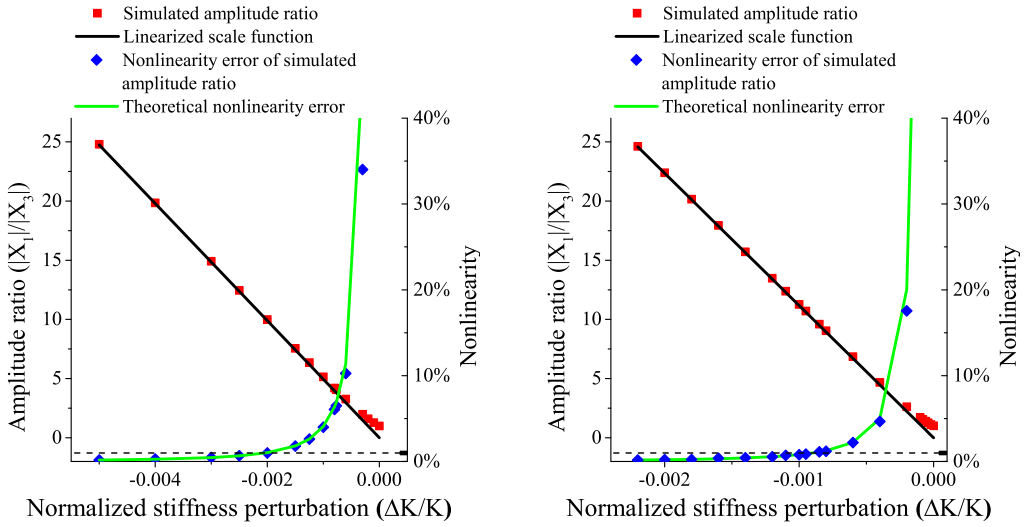

(a) γ_3=4950 (b) γ_3=11174

Figure 5.7: Simulated amplitude ratios for a) $\gamma_3 = 4950$ and b) $\gamma_3 = 11174$ showing the linearized scale function given by Equation 5.11, as well as the nonlinearity error. The nonlinearity error of the simulated amplitude ratio is calculated by comparing the simulated amplitude ratio to the linearized scale function, whereas the theoretical nonlinearity error is calculated using Equation 5.18. The dashed lines at the bottom of the diagram mark a nonlinearity error of 1%, which was regarded as negligible. The nonlinearity increases when the stiffness perturbation approaches zero. For the same stiffness perturbation, a larger γ_3 value results in a smaller nonlinearity error.

5.6.2 Nonlinearity by damping

To estimate the nonlinearity of the amplitude ratio, we assume the nonlinearity term ϵ_1 can be neglected, then Equation 5.16 can be rewritten as:

$$\begin{aligned}\left|\frac{X_1(j\omega_{\text{op}})}{X_3(j\omega_{\text{op}})}\right| &\approx \left|\frac{\gamma_3\Delta K}{K} + j\frac{\gamma_3}{Q}\right| \\ &\approx -\frac{\gamma_3\Delta K}{K}(1+\epsilon_2)\end{aligned} \tag{5.19}$$

If the normalized stiffness perturbation is $\Delta K/K > 2/Q$, ϵ_2 can be approximated as:

$$\epsilon_2 \approx \frac{1}{2}\left(\frac{1}{Q}\frac{K}{\Delta K}\right)^2 \tag{5.20}$$

To demonstrate the nonlinearity error with damping, the simulated amplitude ratios in section 4.3.2.2 were compared to the linearized scale function given by Equation 5.11.

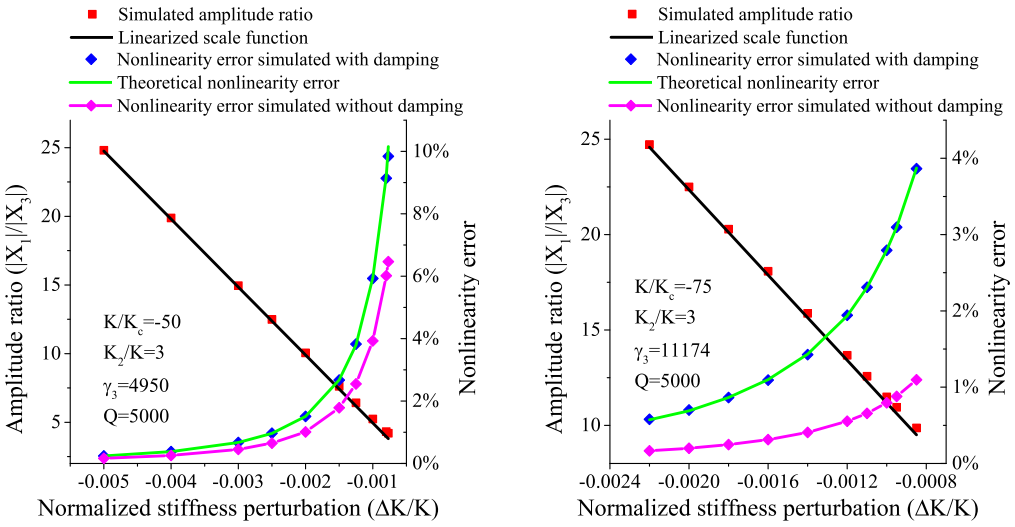

(a) $\gamma_3 = 4950$ (b) $\gamma_3 = 11174$

Figure 5.8: Simulated amplitude ratios compared to the linearized scale function given by Equation 5.11. The nonlinearity errors are also plotted for a) $\gamma_3 = 4950$ and b) $\gamma_3 = 11174$. The total theoretical nonlinearity error was estimated by calculating $\epsilon_1 + \epsilon_2$, where ϵ_1 and ϵ_2 are given by Equations 5.18 and 5.20, respectively. The nonlinearity errors determined by simulation match the theoretical predictions well. The difference between the nonlinearity error with and without damping is described by the term ϵ_2.

The total theoretical nonlinearity error was calculated as $\epsilon_1 + \epsilon_2$, where ϵ_1 and ϵ_2 are given by Equations 5.18 and 5.20, respectively. The results are plotted in Figure 5.8.

Due to the relatively large γ_3 value, the condition $\Delta K/K > 2/Q$ is satisfied within the dynamic range; therefore, the simulation results show a good agreement with the theoretical estimations. Furthermore, they show that even with damping, the linearized scale function can still be regarded as a good linear approximation, with a total nonlinearity error smaller than 1% when the amplitude ratio is larger than 20.

5.7 Noise floor

Assuming the noise of the sensing device is Gaussian and the noise of resonator 1 and 3 are not correlated, the output noise power of the 3DoF sensor, equivalent to the variance of the amplitude ratio $|X_1/X_3|$, can be derived according to [113]:

$$\begin{aligned}\left|\frac{X_1}{X_3}\right|^2_{\text{noise}} &= \sigma^2\left(\left|\frac{X_1}{X_3}\right|\right)\\ &= \left|\frac{X_1}{X_3}\right|^2\left[\left(\frac{\sigma(X_1)}{X_1}\right)^2+\left(\frac{\sigma(X_3)}{X_3}\right)^2\right]\\ &= \left|\frac{X_1}{X_3}\right|^2\left[\frac{X_{n,1}^2}{X_1^2}+\frac{X_{n,3}^2}{X_3^2}\right]\end{aligned} \tag{5.21}$$

where $\sigma^2(f)$ is the variance of function f, which by definition equals to the noise power; $X_{n,i}^2$ $(i = 1, 3)$ is the noise power of the ith resonator. Hence the signal-to-noise ratio (SNR) is:

$$\begin{aligned}\text{SNR} = \left|\frac{X_1}{X_3}\right|^2 \Bigg/ \left|\frac{X_1}{X_3}\right|^2_{\text{noise}} &= \left(\frac{X_{n,1}^2}{X_1^2}+\frac{X_{n,3}^2}{X_3^2}\right)^{-1}\\ &= \frac{\text{SNR}_1 \times \text{SNR}_3}{\text{SNR}_1 + \text{SNR}_3}\end{aligned} \tag{5.22}$$

It can be seen from Equation 5.22 that the output SNR increases as the SNR of resonator 1 and/or 3 improves.

The noise power of resonator 1 and 3 is dominated by two parts, mechanical-thermal noise of the resonators and the electrical-thermal noise of the interface electronics [114]. Therefore, the SNR of resonator 1 and 3 can be written as:

$$\text{SNR}_i = \frac{\text{SNR}_{m,i} \times \text{SNR}_{e,i}}{\text{SNR}_{m,i} + \text{SNR}_{e,i}}, \quad i = 1 \text{ or } 3 \tag{5.23}$$

where $\text{SNR}_{m,i}$ and $\text{SNR}_{e,i}$ are the mechanical and electrical SNR of the ith resonator, respectively. Therefore, to calculate the SNR, we shall analyze the mechanical and electrical noise floor, respectively.

5.7.1 Mechanical noise floor

To theoretically calculate the mechanical noise, the transfer function model of the 3DoF resonator sensor was used. There are three sources of mechanical noise forces, $F_{n,i}, i = 1, 2$ and 3. Thus the block diagram of the model with noise input is shown in Figure 5.9.

The noise power in terms of displacement near the out-of-phase mode of the rth resonator $X_{mn,i}$ $(i = 1$ to $3)$ can be evaluated as [64]:

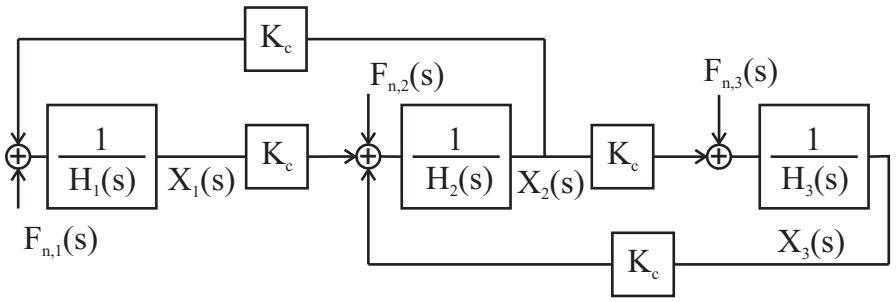

Figure 5.9: Block diagram of a 3DoF resonator sensing device

$$X_{mn,i}^2 = \frac{1}{2\pi}\int_{\omega_{op}-\Delta\omega}^{\omega_{op}+\Delta\omega}\sum_{r=1}^{3} F_{n,r}^2 H_{ir}^2 \mathrm{d}\omega \tag{5.24}$$

Where H_{ir} is the transfer function from rth input to ith output, which was expressed by Equations 4.38a to 4.38f, and the power spectral density of the thermal driving force is given by [114, 115]:

$$F_{n,r}^2 = 4k_B T C_r, \quad r = 1, 2, 3 \tag{5.25}$$

Where k_B, T and C_r are the Boltzmann constant, ambient temperature and damping coefficient of rth resonator, respectively.

Suppose $C_1 = C_2 = C_3 = C$, the noise power of the displacement of resonators 1 and 3, expressed as X_{n1}^2 and X_{n3}^2, respectively, are calculated as:

$$X_{n1}^2 = \frac{2k_B TC}{\pi}\int_{\omega_{\mathrm{op}}-\Delta\omega}^{\omega_{\mathrm{op}}+\Delta\omega}(H_{11}^2 + H_{12}^2 + H_{13}^2)\mathrm{d}\omega \tag{5.26a}$$

$$X_{n3}^2 = \frac{2k_B TC}{\pi}\int_{\omega_{\mathrm{op}}-\Delta\omega}^{\omega_{\mathrm{op}}+\Delta\omega}(H_{31}^2 + H_{32}^2 + H_{33}^2)\mathrm{d}\omega \tag{5.26b}$$

5.7.2 Electrical noise floor

For a standard transimpedance amplifier to convert the motional current to voltage, the input-referred current noise power spectral density can be expressed as [64]:

$$i_n^2 = i_{na}^2 + \left(\frac{R_m + R_f}{R_m R_f}\right)^2 e_{na}^2 + \left(\frac{4k_B T}{R_f}\right)^2 \tag{5.27}$$

where i_{na}, e_{na}, R_m and R_f are the current noise, voltage noise spectral density of the op-amp, equivalent motional resistance of the resonator and feedback resistance, respectively. Given the sensing transduction factor η_S [82] of the device and the 3dB bandwidth of the out-of-phase mode f_{3dB}, the electrical SNR of resonator 1 and 3 within the 3dB bandwidth can therefore be calculated as:

$$\mathrm{SNR}_{e,i} = \frac{X_i^2 \eta_S^2}{i_{n,i}^2 f_{3dB}}, \quad i = 1 \text{ or } 3 \tag{5.28}$$

As will be shown in the experimental results, for a biased 3DoF resonator sensor, within the 3dB bandwidth, for resonator 1 with larger vibration amplitude, the mechanical noise from the resonators is the dominant noise source, whereas outside of the bandwidth, the total noise was mainly attributed to the electronic noise. But for resonator 3 having a smaller vibration amplitude, the electrical noise dominated. The ultimate limit of the output noise power was imposed by electrical noise from the interface electronics.

5.8 Bias point

As discussed in this chapter, for practical sensors utilizing a 3DoF weakly coupled resonator system, a few practical issues limit the performance of the sensor. For instance, a trade-off exists between the linear sensitivity and the dynamic range, this can be shown by the mathematical expressions: from Equation 5.4, it can be seen that for a given Q-factor of the out-of-phase mode, a smaller γ_3 is desired for larger dynamic range; whereas from Equation 5.11, it was shown that a large γ_3 is preferred for enhanced linear sensitivity.

To relax this trade-off, we propose a bias approach. The theoretical foundation of this approach was demonstrated in Section 4.3.3. By intentionally applying a stiffness perturbation to resonator 3, the region with undistinguishable modes can be translated out of the desired dynamic range, thus relaxing the restrictions of the γ_3 values for higher sensitivity. Furthermore, by applying a negative bias point, the linearity can be improved, as shown in Figure 5.8.

However, the bias point cannot be arbitrarily chosen, as for the more optimum bias point in terms of dynamic range and linearity, the amplitude ratio is often large. This makes the smaller vibration amplitude difficult to detect. Moreover, as shown in the theoretical derivation of the noise floor, larger amplitude ratio also leads to higher noise floor, as shown by Equation 5.21.

5.9 Summary

To summarize, we have discussed some of the practical considerations for the actual sensors for stiffness change applications. Because of the mode aliasing effect and the noise floor, the dynamic range of the sensor would be limited by Equations 5.4 and 5.5 for stiffness perturbations $\Delta K < 0$ introduced to resonator 3.

Furthermore, we have compared some of the possible output metrics of the sensor, and came to a conclusion that amplitude ratio has the largest linear range, as well as improved sensitivity compared to conventional eigenstate shift as an output signal. Therefore, for this research, we shall use amplitude ratio as the output signal.

In what follows, we have theoretically estimated the linearity of amplitude ratio as a function of the stiffness perturbations, as well as nonlinearity errors and the sources.

In addition, we have identified that the noise comes from mechanical structures and electronic interface. Then we proposed formulas to calculate the mechanical and electrical noise floor of the sensor, which can be useful for future research.

Finally we have proposed a bias point approach to relax the trade-off between the linear sensitivity and dynamic range, while also improving the linearity of the sensor.

Chapter 6

Experimental Validation of Theorem

6.1 Introduction

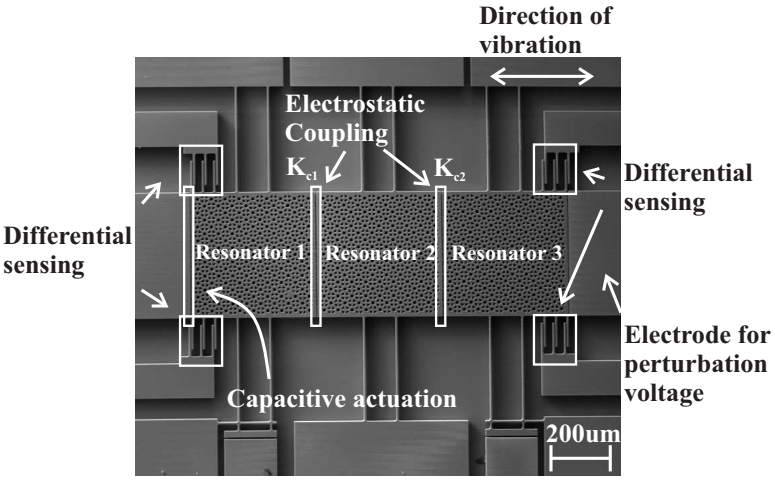

Figure 6.1: SEM image of a microfabricated prototype 3DoF resonator sensing device

To serve the purpose of verifying the theoretical predictions, proving the concept, and to demonstrate the sensitivity improvement of a 3DoF resonator device as a sensor, we have designed a batch of MEMS devices and tested them experimentally. Two different designs were fabricated and tested. However, due to the effect of anti-resonance caused by feedthrough capacitance (as discussed in Section 3.3.2.1) of one of the designs, which could lead to inaccurate measurements of the amplitudes, thus is not included in this chapter. The design discussed in this chapter, as shown in Figure 6.1, included differential capacitance measurement capabilities, which reduces the effect of feedthrough capacitance.

Since the devices were for proof-of-concept purposes, they were intended neither to achieve a certain sensitivity or resolution performance, nor for a particular application. Therefore the selection of design parameters for the devices was somewhat arbitrary and not optimized. However, some design considerations put into the device design may be helpful for future optimization of the sensor. Therefore they are still discussed in this chapter.

In what follows, the test of the devices were carried out electrically under vacuum environment, which was intended for high Q-factors, hence reducing the mode aliasing effect. The experimental results of two devices were also presented in this chapter to compare with the theoretical predictions. The experiments in this chapter included: a) the amplitude ratio with respect to normalized stiffness perturbation, to prove their relationship (Equation 4.44 and Figure 4.19), as well as the nonlinearity errors (Equation 5.16 and Figure 5.8); b) frequency response measurements, to demonstrate the effect of mode aliasing (Figure 4.16), as well as the dynamic range of stiffness perturbation limited by the mode aliasing effect (Section 5.2); c) noise calculations (Section 5.7); d) comparative investigations of different output metrics, to prove the simulations in Section 5.3.

6.2 Device design

6.2.1 Device structure

An SEM micrograph of a fabricated prototype chip of the 3DoF MEMS resonator device is shown in Figure 6.1. The system consists of three resonators, coupled to its neighbouring resonator through electrostatic springs.

6.2.1.1 Electrostatic coupling

Electrostatic coupling was used due to its good controllability of the coupling strength as discussed in previous sections. To realize the electrostatic spring, as shown in Figure 6.2, each resonator is placed next to its neighbour with an air gap in between. When a DC voltage was applied to resonators 1 and 3, whereas resonator 2 was grounded, electrostatic springs were created. The spring constants can be easily altered by changing the DC voltage value.

In addition to the electrostatic spring, a parallel-plate capacitive actuation was also used. The nominal gap of this parallel-plate transducer was designed to be identical to that of the electrostatic spring. This in essence created a symmetrical double sided capacitor structure as discussed in Section 3.2.4. Hence, the second order nonlinearity term that exists in the electrostatic springs can be significantly reduced, as demonstrated by Equation 3.24. However, the third order nonlinearity term still remains.

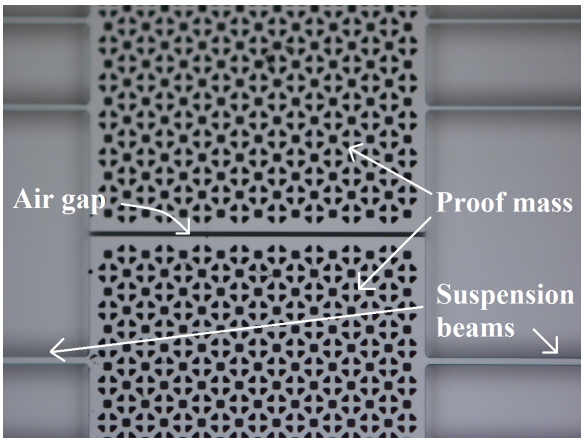

Figure 6.2: A zoomed-in image of the electrostatic coupling within the 3DoF resonator sensing device. The image was tilted 90 degrees from Figure 6.1 for better presentation. Therefore, the air gap shown here is horizontal.

As shown by Equation 3.24, a larger air gap d gives a smaller nonlinearity for a given displacement, thus a larger air gap is preferred for increasing the displacement range for linear electrostatic spring. However, a larger gap also means that a higher voltage is required to obtain the same coupling strength, as shown by Equation 3.23.

6.2.1.2 Resonator design

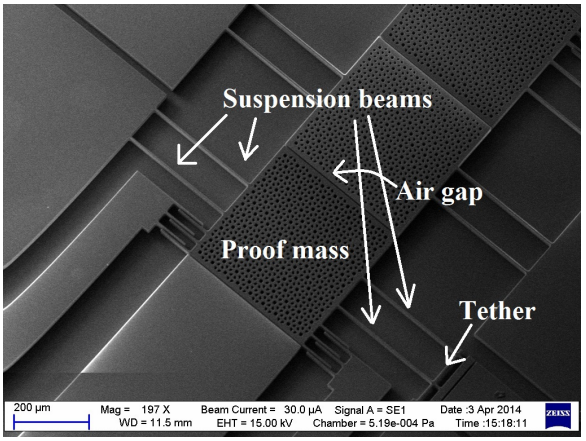

Figure 6.3: An SEM image of the resonators from angle. The suspension beams, proof mass, air gap for electrostatic coupling and tether structure have been indicated in the image.

Relatively large proof masses were used to obtain low resonant frequencies (in the kHz range), and to make the proof masses less prone to random fabrication variations, as an important assumption is that all masses are equal. An SEM image of the resonator structure is shown in Figure 6.3.

For each resonator, four suspension beams were attached to each proof mass so that out of plane tilting is minimized. The suspension beams have one end fixed, while the

other end moves perpendicular with respect to the beam length. This type of beam was used due to the moderate linear spring constant and nonlinearity, and more importantly the capability of integrating proof masses, compared to other types of suspension beams such as fixed-fixed beam and cantilever.

The effective linear spring constant of each beam is given by Equation 3.3b. Assuming that no axial force or residual stress, the effective mechanical spring constant of the resonators can be calculated as:

$$K_m = 4 \times \frac{Ew^3t}{L^3} \tag{6.1}$$

where E, w, t, L are Young's modulus, width, thickness and length of each supporting beam, respectively.

A low mechanical stiffness of the resonator was desired in our design, as a smaller K_m gives a lower resonant frequency (in the kHz range), simplifying the interface circuitry while retaining high sensitivity.

6.2.1.3 Tether

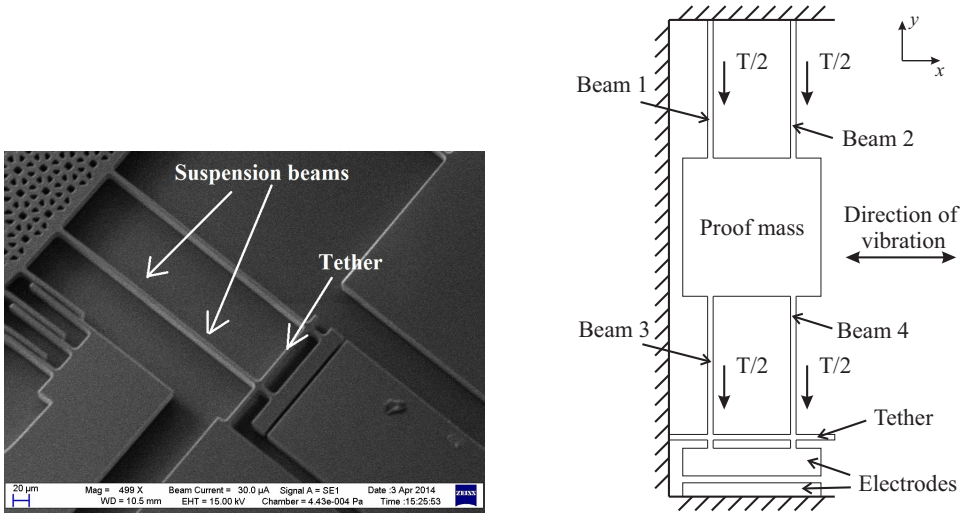

(a) Tether structure

(b) Schematic of a resonator with tether

Figure 6.4: Figures showing: a) a zoomed-in SEM image showing the tether structure; b) schematic of the resonator with tether.

Furthermore, to demonstrate the axial force sensing capability of the device, a tether structure [51] was used in our design to allow the transmission of an axial electrostatic force to the suspension beams (Figure 6.4). In addition, the tether should impede the movement of the electrode attached to the bottom of the suspension beams when the resonator is vibrating, so that the electrostatic force is kept as constant as possible. To

achieve these, the tether was made wide in the x-axis (170μm), but thin in the y-axis (5μm) in our design.

a) Thin tether: as for the force transmission, the tether was made thin in the y-axis. This is explained as follows. The tether, which is a cantilever beam in essence, has a stiffness of [82]:

$$K_{\text{tether}} = \frac{Etw_t^3}{4L_t^3} \tag{6.2}$$

where E, t, w_t, L_t are the Young's modulus, the thickness of the device, the width in the y-axis and effective length of tether, respectively. The longitudinal stiffness of the suspension beam is given by [82]:

$$K_{\text{long}} = \frac{Etw}{L} \tag{6.3}$$

where w and L are the width in the x-axis and the length of the suspension beam.

When testing the force sensing capability, two different DC voltages, with a voltage difference of ΔV, are applied to the resonator and the electrode below, generating an electrostatic force in the negative y-axis pulling the resonator:

$$T = \frac{\varepsilon_0 A_e \Delta V^2}{2d_e^2} \tag{6.4}$$

To applied forces in the negative y-direction, the tether and the suspension beams act similarly to two springs in parallel [51]. Ideally, the tether does not absorb any force applied in the y-axis, so that all the forces can be measured by the resonator. Hence, the tether was designed to be thin, ensuring that nearly all the force applied is absorbed by the suspension beams.

By making the tether thin, we are able to assume that the entire electrostatic force is transmitted to the resonators for measurement. For example, the shortest effective length of the tether is 60μm, with the width of the tether of 5μm, gives a maximum stiffness of the tether $K_{\text{tether}} = 538\text{N/m}$. Whereas in the y-axis, suspension beams 1 and 3 are in series, therefore the effective longitudinal stiffness is $K_{\text{long}} = 2.48 \times 10^4\text{N/m}$ for the parameters of device 2 (will be shown in Table 6.1). This indicates that more than 97.9% of the force applied is absorbed by the suspension beams, with less than 2.1% of the force exerting on the tether.

Moreover, as demonstrated in [96], the tether structure would act as an axial stress release element, which reduces the third order mechanical nonlinearity. Therefore, the tether should be thin, so that the stress relief is more efficient.

b) Long tether: long tether design ensures that the tether has a high mechanical stiffness in the x-direction, therefore, the movement of the junction of the tether and the suspension beams in the x-axis can be neglected. In addition, when the displacement of the resonator in the direction of vibration is small compared to the length of the beam, the movement of the resonator in the y-axis is also negligible. Consequently, the tether efficiently constraints the movement of the electrode attached to the suspension beams, and thus it can also be regarded as a fixed end for the two suspension beams attached.

6.2.1.4 Actuation and motion pick-up

An AC voltage, with a small amplitude compared to the fixed DC voltage on resonators 1 and 3, was applied to the electrode next to resonator 1. This created an alternating electrostatic force on resonator 1, driving the 3DoF resonator sensor with only one actuation force.

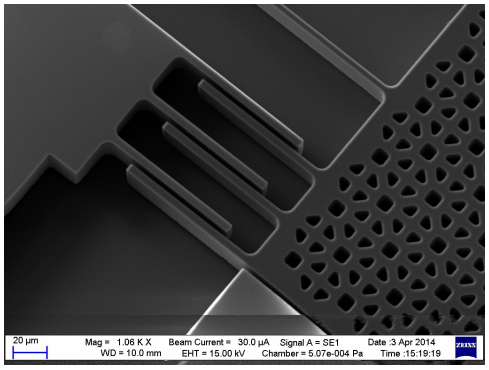

(a) Comb finger structure

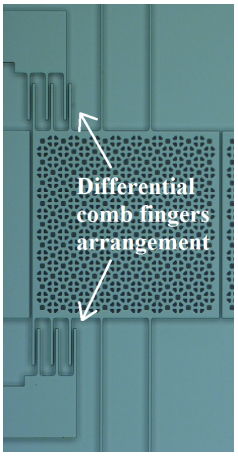

(b) Arrangement of differential comb fingers

Figure 6.5: Images showing: a) a zoomed-in SEM image showing the single comb finger structure; b) an optical image of one of three resonators with differential comb finger arrangements.

To sense the motions of resonators 1 and 3, two sets of comb fingers were attached to the resonators on either side. The SEM image of one set of comb fingers is shown in Figure 6.5(a) Differential capacitive sensing was realized through the arrangements of the comb fingers, shown in Figure 6.5(b). It can be seen that the two sets of comb fingers attached to the proof mass were on different side of those attached to the stator. Hence the movement in one direction results in opposite change of capacitance, thus realizing differential sensing. The length of the comb fingers were 90μm; this ensures

that the comb fingers will not vibrate. The overlap length was designed to be 70μm to get sufficient current to be measured with a standard transimpedance amplifier (TIA).

6.2.1.5 Design values

The design values of the two devices characterized are summarised in Table 6.1. To assist the understanding of the values, a schematic of the 3DoF prototype device with dimension notations is shown in Figure 6.6.

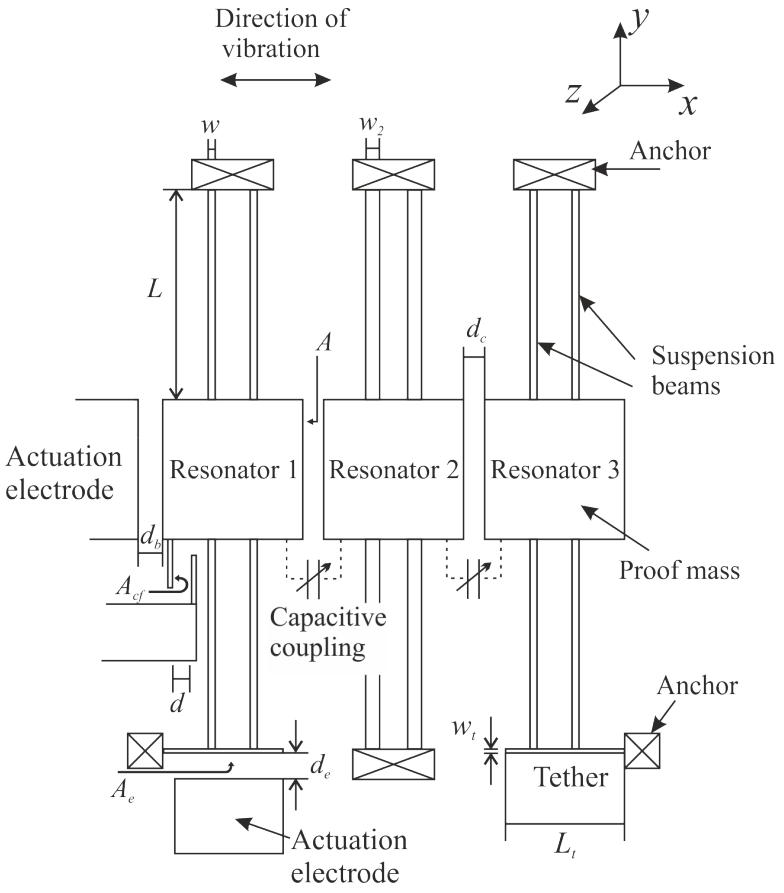

Figure 6.6: Schematic of the prototype of the 3DoF resonator sensing device with notations of the dimensions.

It should be pointed out that, the smallest beam width achievable with an acceptable yield in the fabrication process used was 5μm, the minimum aspect ratio was 1:70, resulting in a beam length of 350μm. Therefore, the beams were designed to achieve the minimum stiffness for device 1, which was desired for high sensitivity. As for device 2, it served the purpose of demonstrating the capability of the fabrication process, hence we have pushed the design parameters over the limit. It also showed that it is possible to fabricate compliant beams.

Table 6.1: Dimensions of the devices

Parameter	Design Value		Unit
	Device 1	Device 2	
Device layer thickness	30		μm
Suspension beam lengths (resonator 1, 2 and 3) (L)	350	300	μm
Suspension beam width (resonator 1 and 3) (w)	5	4	μm
Suspension beam width (resonator 2) (w_2)	7.5	5	μm
Comb finger length	90		μm
Tether length (L_t)	170		μm
Tether width (w_t)	5		μm
Gaps between resonators ($d = d_c$)	4.5	3.5	μm
Gaps between resonator and electrodes, between comb fingers ($d = d_b$)	4.5	3.5	μm
Gaps between resonator and force electrodes ($d = d_e$)	4.5		μm
Proof mass dimensions	360×360		$(\mu\text{m})^2$
Mass values (M)	6.94	6.87	nkg
Cross sectional area of electrostatic coupling and perturbation electrode $A = A_c = A_b$	360×22		$(\mu\text{m})^2$
Comb finger overlap cross sectional area A_{cf}	70×22		$(\mu\text{m})^2$
Cross sectional area of electrode for electrostatic force A_e	160×22		$(\mu\text{m})^2$

For other design values, as stated at the start of the chapter, the selections were rather arbitrary, since this is only a proof-of-concept design. Further optimization is required if the device were to be used for specific applications.

6.2.2 Perturbation design

6.2.2.1 Stiffness perturbation by spring softening

When DC voltages were applied to resonators 1 and 3, electrostatic springs were also created between the resonators and the driving electrodes, as well as the sensing electrodes. Neglecting the higher order terms of the electrical spring stiffness, the effective stiffness of resonator 3 can be approximated as:

$$K_{\text{eff}} = K_m + K_e \approx \frac{4Ew^3t}{L^3} - \frac{\varepsilon_0(AV_b^2 + 6 \times A_{\text{cf}}V_{cf}^2)}{d^3} \tag{6.5}$$

where K_m is the mechanical stiffness of the suspension beams, K_e is the total electrical spring stiffness arising when a bias voltage is applied on the resonator proof mass, A_{cf} is the cross-sectional area of the comb finger overlap, V_b is the voltage difference between the proof mass of resonator 3 and neighbouring electrode, and V_{cf} is the voltage difference between the resonator proof mass and stationary comb fingers.

It is noticed from Equation 6.5 that by altering the voltage on the electrode on the right, hence changing V_b, we can modify the effective stiffness of the resonator. Therefore, we are able to perturb the coupled resonator system with a stiffness change by altering V_b. This is effectively adding negative stiffness perturbations to resonator 3 by spring softening. Neglecting higher order terms, the perturbation in stiffness can be approximated as:

$$\Delta K \approx -\frac{\varepsilon_0 A}{d^3}\left[(V_b + \Delta V_b)^2 - V_b^2\right] \tag{6.6}$$

It should be pointed out that in presence of the perturbation voltage, the proof mass moves out of its rest position due to the electrostatic force, resulting in a small change in capacitive gap d. However, due to the relatively small perturbation voltages applied in the experiments, the calculated resultant displacement was negligible compared to the air gap. For instance, for device 1, the perturbation voltage was smaller than 12V, the DC displacement was below 40nm, which was less than 1% compared to the designed air gap of 4.5μm. Therefore Equation 6.6 serves as a good first order approximation of the introduced stiffness perturbations.

Random fabrication variances in dimensions lead to an intrinsic imbalance in the system. Because of the proof masses design, the mass variances were supposed to be negligible compared to the proof masses, therefore ignored in the analysis; only the effect of variances in stiffness is considered. The variances in dimensions lead to an offset in stiffness; neglecting higher order terms, the normalized stiffness perturbation is deduced as:

$$\frac{\Delta K}{K} \approx -\frac{\varepsilon_0 A}{d^3}\left[(V_b + \Delta V_b)^2 - V_b^2\right]/K_{\text{eff}} - \text{Offset} \tag{6.7}$$

where K_{eff} is the effective stiffness of the resonator given by Equation 6.5.

6.2.2.2 Stiffness perturbation by axial tensile force

For the other part of the experiment, the stiffness of resonator 1 was perturbed by an axial force along the length of the beams. This was achieved by the tether design as shown in Figure 6.4(b).

When two different DC voltages are applied to the resonator and the electrode below, an electrostatic force is generated in the negative y-axis pulling the resonator. Due to the relatively large length of the electrode in the x-axis of 160μm compared to the air gap of 4.5μm, the fringe field can be neglected. Assuming small displacements in the y-axis, the tensile force for the resonator T in terms of voltage difference ΔV between the resonator and the electrode, cross-sectional area of electrode A_e, air gap d_e and dielectric constant of vacuum ε_0 is given by [82]:

$$T = \frac{\varepsilon_0 A_e \Delta V^2}{2d_e^2} \tag{6.8}$$

For an applied force in the y-axis, the two identical suspension beams (beams 3 and 4 in Figure 6.4(b), are in parallel. Hence the tensile force T is evenly distributed to the two suspension beams. Furthermore, the suspension beams 1 and 3 are in series, so are suspension beams 2 and 4. Therefore, the tensile force applied on each suspension beam equals to $T/2$, thus introducing stiffness perturbations to the resonator, as shown by Equation 3.3b. Hence for each suspension beam, the effective spring constant is given by:

$$K_{\text{beam}} = \frac{Etw^3}{L^3} + \frac{0.6T}{L} \tag{6.9}$$

The stiffness perturbation introduced by the tensile force, normalized to the effective stiffness of the resonator K_{eff} (given by Equation 6.5), is therefore:

$$\frac{\Delta K_{\text{force}}}{K_{\text{eff}}} = \frac{2.4T}{LK_{\text{eff}}} \tag{6.10}$$

If V_c is the coupling voltage applied to resonator 1 and 3, V_e is the voltage applied to for electrostatic force perturbation, the tensile electrostatic force exerted to resonator 1 can be calculated from Equation 6.8:

$$\Delta T_1 = \frac{\varepsilon_0 A_e (V_c - V_e)^2}{2d_e^2} \tag{6.11}$$

It should be pointed out that $V_e = 0$ for resonator 3, hence this also introduces an tensile force to resonator 3, which can be calculated as:

$$\Delta T_3 = \frac{\varepsilon_0 A_e V_c^2}{2d_e^2} \tag{6.12}$$

As discussed in Section 4.3.3, for perturbations applied to both resonator 1 and 3, the effective perturbation is the difference. Therefore the effective perturbation force can be calculated as:

$$\begin{aligned} \Delta T &= \frac{\varepsilon_0 A_e [(V_c - V_e)^2 - V_c^2]}{2d_e^2} \\ &= \frac{\varepsilon_0 A_e (V_e^2 - 2V_c V_e)}{2d_e^2} \end{aligned} \tag{6.13}$$

The resulting perturbation is therefore:

$$\frac{\Delta K_{\text{force}}}{K_{\text{eff}}} = \frac{2.4\Delta T}{LK_{\text{eff}}} = \frac{1.2\varepsilon_0 A_e(V_e^2 - 2V_cV_e)}{K_{\text{eff}}Ld_e^2} \tag{6.14}$$

It should be pointed out that, due to the high longitudinal stiffness of the suspension beams, the elongation of the beams are trivial compared to the beam length L. The resulting stiffness perturbation by strain change is therefore neglected. Hence we can assume that the stiffness perturbation is caused solely by the electrostatic force.

6.3 Fabrication process

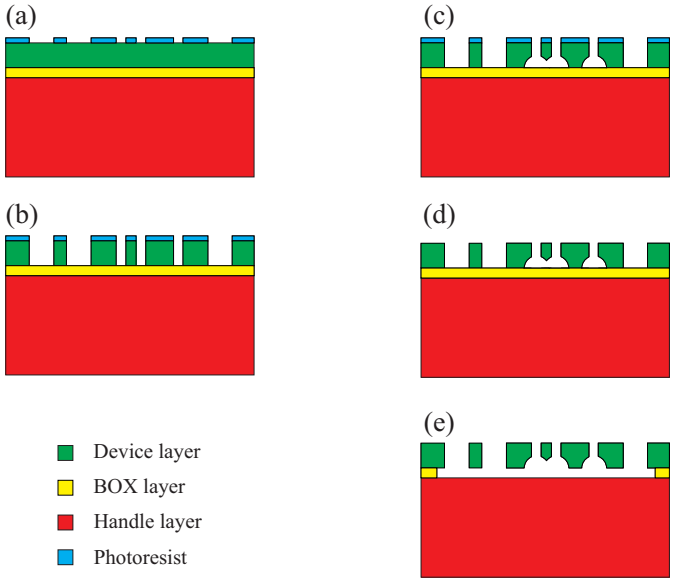

Figure 6.7: The process flow of the single mask SOI process: a) deposition and patterning of photoresist, b) DRIE etching, c) overetching, d) photoresist removal and dicing, e) HF solution release

The 3DoF resonator devices were fabricated using a single mask silicon on insulator (SOI) process with a structural layer of 30μm thickness. The process flow is briefly summarised here (a more detailed description is provided in [116]), it comprised the following main steps:

1. Spincoating of photoresist on the front side of the SOI wafer, and patterning of the photoresist using a photomask, Figure 6.7a.
2. Deep reactive ion etch (DRIE) to define the device layer structure, Figure 6.7b,
3. Overetch step by DRIE, utilizing the notching effect [117, 118], Figure 6.7c.

The notching only occurred when the trenches were narrower than a critical width, which was experimentally determined to be 16μm. The bottom of all trenches narrower than 16μm, including those between comb fingers, parallel plates and the majority of proof masses (due to release holes), were thus deliberately overetched and released. Structures with a larger area, such as the proof masses, were not completely released during this step; a small part on the edge of the proof masses was intentionally designed so that the proof masses and suspension beams were protected from shocks occurring during the dicing step.

To avoid the suspension beams from being overetched, the beams were placed well apart, much further away than the critical gap width of 16μm, from any other structures. Therefore, negligible notching occurred at the bottom of these beams, and thus were not released in this step.

Due to the overetch step, stiction of the proof mass and other structures to the handle wafer was avoided during a final wet release step removing the buried oxide (BOX) layer [119, 120].

4. Removing the photoresist, followed by dicing, Figure 6.7d. The BOX layer is retained in this step, so the fragile resonators structures will not be damaged during the dicing process.

5. Wet etching using HF solution to release the moving structures, including suspension beams and the edge of the proof masses, Figure 6.7e.

6.4 Experimental methodology

6.4.1 Device configuration

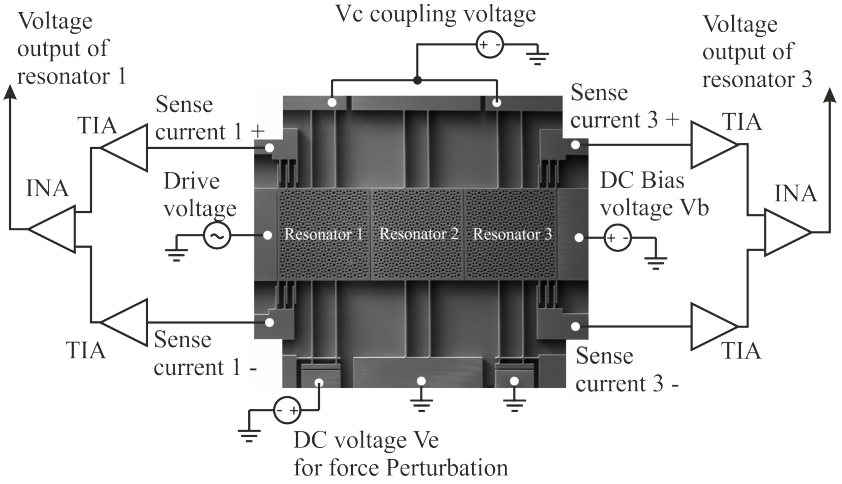

Figure 6.8: Test configuration of the prototype 3DoF resonator sensing device

A prototype 3DoF resonator sensor was fabricated and configured as shown in Fig. 6.8 for characterization. The same DC voltage was applied to both proof masses of resonators 1 and 3, to ensure identical coupling, thus $K_{c1} = K_{c2}$.

An AC drive voltage was applied to the actuation electrodes on the left, so only F_1 was applied to the system, thus satisfying $F_2 = F_3 = 0$.

A DC voltage was applied to the driving electrodes on the right. This created a DC voltage change in V_b, equivalent to the ΔV_b term in Equation 6.6.

Differential sense currents were obtained from the comb fingers dedicated for motion sensing, and then fed to the interface circuitry for further processing.

6.4.2 Electrical test set-up

To electrically test the chip, the chip was mounted on a chip carrier by normal double sided adhesive tape and wire bonded to the contacts. The details of wire bonding can be found in Appendix E. The chip carrier was then inserted into a socket on a printed circuit board (PCB). The design considerations of the PCB board will be discussed later. The circuit board was placed into a customized vacuum chamber with electrical feedthroughs. The ambient pressure was 20μTorr ensuring minimum air damping loss, so a high quality factor could be obtained. The experimental set-up is shown in Fig. 6.9.

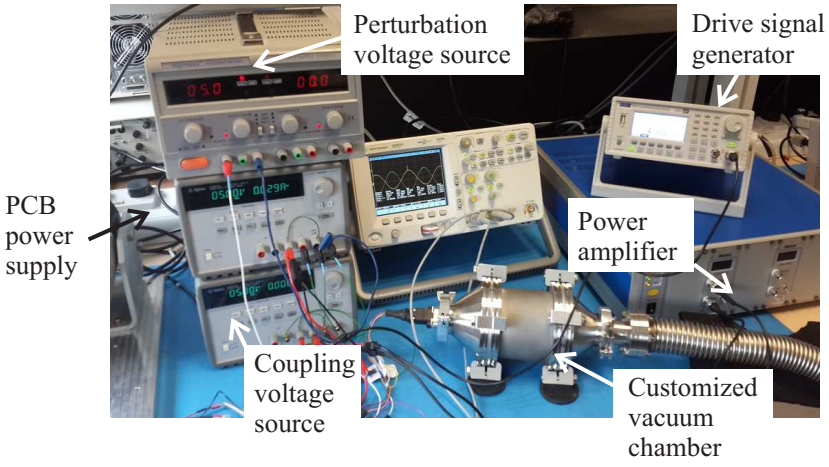

Figure 6.9: Experimental set up for 3DoF sensor characterization

To drive the resonators, a sinusoidal AC voltage with adjustable frequency was generated from the signal generator. The peak to peak value was altered for different DC voltages, to ensure driving the resonators in the linear region.

6.4.2.1 Circuit board design considerations

To pick up the motional currents of the resonators, standard transimpedance amplifiers (TIAs) were used to convert and amplify the differential motional currents to differential voltage signals. The reason why TIAs were used is that the input impedance of the TIA is inversely proportional to the open loop gain of the amplifier, thus is typically negligible. Therefore, it reduces the loading of the resonators to a minimum. The amplifier used for the TIAs are AD8065 from Analog Devices Inc, amplifying the sub-nano ampere motional currents from the resonators to μV voltages. The feedback network of the TIA consists of two resistors connected in series, while each resistor is parallel to a capacitor. The capacitors were used to prevent the TIA circuit from the self-oscillation because of the parasitic input capacitance C_{in}. A larger capacitance is favoured for stability, while reducing the bandwidth for a given feedback resistor. In addition, a larger feedback resistance value is preferred for larger gain and lower input-referred current noise. But this would result in a more harsh trade-off between the bandwidth and stability. For this reason, two resistors were placed in series, relaxing the trade-off as well as increasing the gain. The values of the resistors and capacitors were chosen to be 3.3MegΩ and 0.2pF, achieving enough bandwidth (>100kHz considering the resonant frequency of 20kHz of the resonators) and a 6.6MegV/A current gain.

The differential signals were further amplified by subsequent instrumentation amplifiers (INAs) (AD8421, Analog Devices Inc). By using the INAs, differential signals were amplified by 100 times, to a measurable level of hundreds of millivolts, whereas the common mode signals such as the feedthrough signals, were suppressed to the sub-millivolt range, which can be regarded as negligible. The detailed current amplifying circuit of one channel is presented in Figure 6.10.

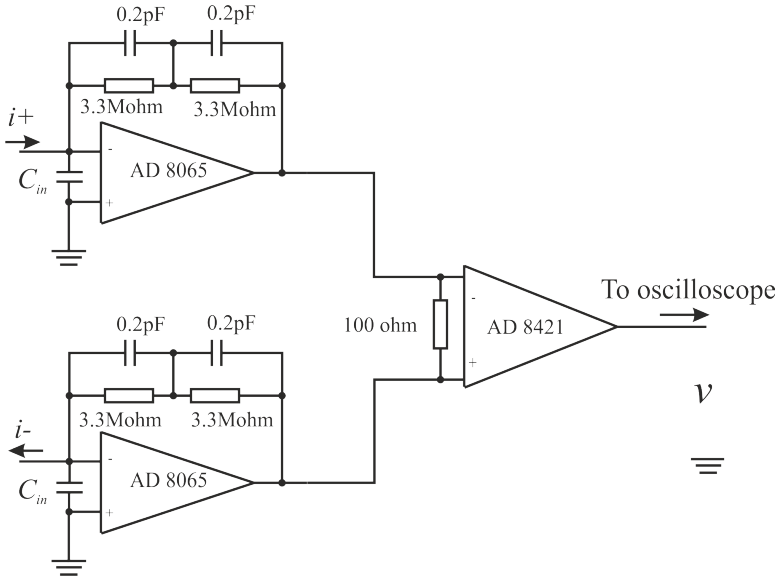

Figure 6.10: Detailed schematic of the current amplifying circuit of one channel. C_{in} is the input parasitic capacitance of the op-amp.

A D-sub connector was used as an I/O port for the electrical signals. Several switches were used to control the drive signals. The whole board is shown in Figure 6.11.

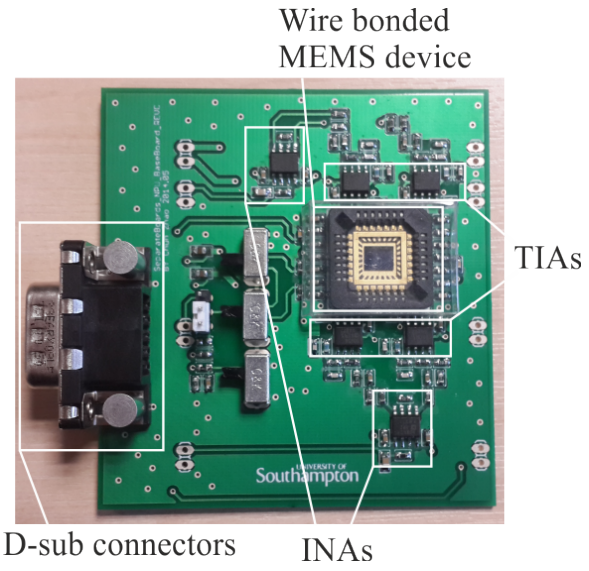

Figure 6.11: Demonstration of the prototype circuit board for measurement.

6.4.3 Experimental method

A real-time measurement method was employed in our work. Motional currents were used to measure the motion of resonators 1 and 3. With both resonators vibrating at the same frequency, the ratio of the motional currents equals the amplitude ratio.

A two-channel oscilloscope (DSO6032A from Agilent Technologies) was used for measuring the voltage amplitudes of the resonators simultaneously. By altering the frequency of the drive signal in 0.01Hz steps, two distinct peaks in the amplitudes could be found, i.e., the in-phase and out-of-phase modes. The out-of-phase mode could be identified by the phase difference between the resonators. Then, the applied frequency was maintained at the out-of-phase mode frequency for the oscilloscope to measure the amplitudes over 500 cycles. The oscilloscope computed the mean value of the amplitudes of both resonators, which were then used to calculate the amplitude ratios. Figure 6.12 shows the typical real-time response of the resonators 1 and 3 respectively (in this case, this shows the transient response of device 2). It can be clearly seen that, after changing the perturbation stiffness, the amplitude ratio changed dramatically.

Additionally, the mode frequencies were recorded as displayed by the signal generator. It is worth noting here that the third mode was neglected in the analysis due to the fact that, in the experiment, this mode could not be detected as the amplitudes of resonators 1 and 3 were below the noise level.

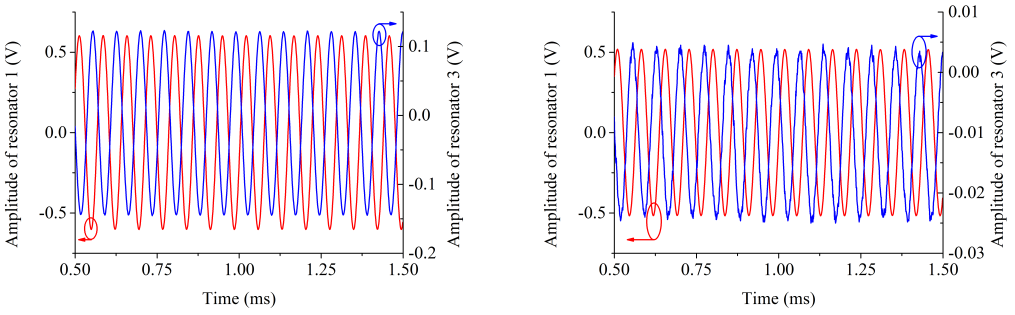

(a) 0.45V perturbation voltage

(b) -0.9V perturbation voltage

Figure 6.12: Typical transient response of the resonators 1 and 3 of device 2: a) 0.45V of perturbation voltage, b) -0.9V perturbation voltage was applied, respectively.

6.5 Experimental results

6.5.1 Experimental results of device 1

The testing of device 1 was intended to demonstrate the response of a 3DoF weakly coupled resonator sensor to stiffness changes caused by electrostatic spring softening. To demonstrate this, V_e was set to 0V, V_b was altered to introduce variable stiffness perturbations, and 5 different coupling voltages V_c were used and are listed in the following table. V_e, V_b and V_c were applied to the electrodes as shown in Figure 6.8.

Table 6.2: Coupling voltage applied and calculated K/K_c and γ_3 values

Coupling voltage (V)	K/K_c	γ_3
30	83.5	17073
34.5	62.4	9656
40	45.7	5250
45	35.7	3259
50	28.5	2117

6.5.1.1 γ_3 and offset values extraction

Before proceeding to illustrate the functionality of the sensor, it is important to quantify the γ_3 values, since the performance of the sensor, e.g. sensitivity (Equation 4.17a), depends critically on this parameter. In addition, the offset values in stiffness perturbations $\Delta K/K$ were characterized due to its importance in analysing the measurement results.

To approximate the γ_3 and offset values from the measurement data, the linearized scale function Equation 5.11 was utilized. Both the γ_3 and offset values were estimated by

fitting the measured data for amplitude ratios larger than 20 to a linear function. The slope of the line was expected to be a good approximation of $-\gamma_3$ and the intersection of the line to the horizontal axis was regarded as a good estimation of the offset value. The estimated γ_3 values and offset values are listed in Table 6.3. The $\Delta K/K$ values in the following sections were deduced using Equation 6.7 including the experimentally estimated offset values.

Table 6.3: Extracted values of γ_3 and offset

Coupling voltage (V)	Extracted γ_3	Extracted offset of $\Delta K/K$
30	13558	3.8×10^{-3}
34.5	9118	2.6×10^{-3}
40	5534	9.1×10^{-4}
45	3538	-5.7×10^{-4}
50	2512	-2.7×10^{-3}

6.5.1.2 Frequency response

Frequency sweep measurements were performed to find out the dynamic range and Q factor of the resonator structures. An example frequency response, for 30V coupling voltage, with strong mode aliasing (out of the dynamic range) and weak mode aliasing (in the dynamic range) is shown in Figure 6.13.

It can be seen that, for 4.85V perturbation voltage, the corresponding stiffness perturbation $\Delta K/K$ was calculated as -0.23×10^{-3} according to Equation 6.7. Two modes

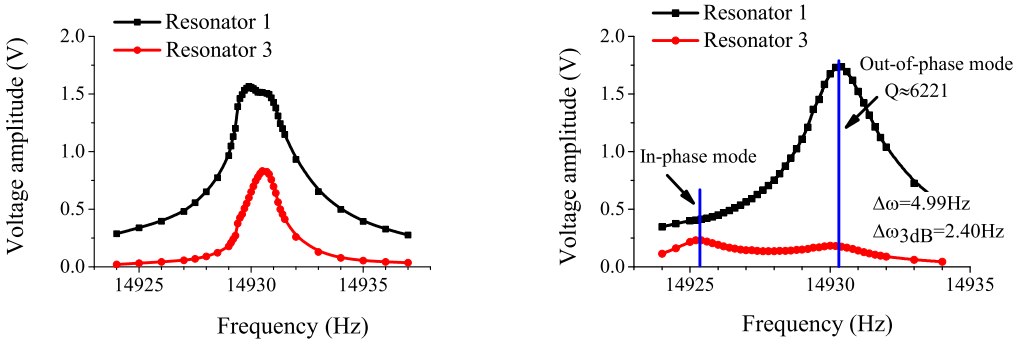

(a) Strong mode aliasing

(b) Weak mode aliasing

Figure 6.13: Measured frequency response of resonators 1 and 3, with 30V coupling voltage, corresponding to $K/K_c = 83.5$ and $\gamma_3 = 17073$. a) For a perturbation voltage of 4.85V, equivalent to $\Delta K/K = -0.23 \times 10^{-3}$, strong mode aliasing occurs and therefore the out-of-phase mode was difficult to identify; b) for a perturbation voltage of 4.15V, equivalent to $\Delta K/K = -0.69 \times 10^{-3}$, weak mode aliasing occurred and the out-of-phase mode could be identified.

were close to each other, thus a strong mode aliasing effect was observed, as shown in Fig. 6.13(a). When we changed the perturbation voltage to 4.15V, hence decreasing the value of $\Delta K/K$ to -0.69×10^{-3}, the frequency difference between the in-phase and out-of-phase modes became larger, as predicted by Equation 5.1, the mode aliasing effect became weaker, and the in-phase and out-of-phase modes could be identified, as shown in Fig. 6.13(b).

The frequencies of the in-phase and the out-of-phase modes were found to be 14925.42Hz and 14930.41Hz, respectively; while the calculated corresponding mode frequencies were 14414.76Hz and 14419.90Hz, respectively; hence there is good agreement between measured and theoretical values.

The measured 3dB bandwidth of the out-of-phase mode was 2.4Hz; from this, the quality factor could be calculated as approximately 6221 in vacuum, which was sufficiently close to the assumed quality factor of 5000 in the analytical derivations in Chapter 4.

6.5.1.3 Output metrics

First we shall compare the different output metrics. To demonstrate this, we have used 50V as the coupling voltage. This is to ensure that any $\Delta K/K \leq 0$, is within the dynamic range of the sensor, as discussed in Section 5.2.

The drive voltage was chosen to be 8mV, ensuring that the amplitudes are within the range for linear springs. The vibration amplitudes of resonators 1 and 3 at the out-of-phase mode frequency were recorded for calculating amplitude ratios, eigenstate shifts and amplitude differences. The in-phase mode frequencies were also recorded as an output signal. The measured mode frequencies, as well as calculated amplitude ratios, eigenstate shifts and amplitude differences from the measured amplitudes are plotted in Figures 6.14 to 6.17. Also plotted in the figures are the extracted linearized function and the nonlinearity errors.

From the measured results, we can summarize the linear sensitivity and linear range in Table 6.4. Comparing the results in Tables 6.4 and 5.2, it can be seen that the measured results agreed well with the theoretical and simulation results.

Table 6.4: Output metrics summary from measurement results

Output	Linear sensitivity	Linear range (nonlinearity error $< 5\%$)
Frequency shift	0.54	$\Delta K/K < -0.001$
Amplitude ratio ($\lvert X_1\rvert/\lvert X_3\rvert$)	2512	$\Delta K/K < -0.002$
Eigenstate shift	308	$-0.001 < \Delta K/K < 0$
Amplitude difference ($\lvert X_1\rvert - \lvert X_3\rvert$)	841V	$-0.001 < \Delta K/K < 0$

From the measurement results, it can also be seen that the amplitude ratio has the highest sensitivity, and second largest linear range, among the dimensionless output

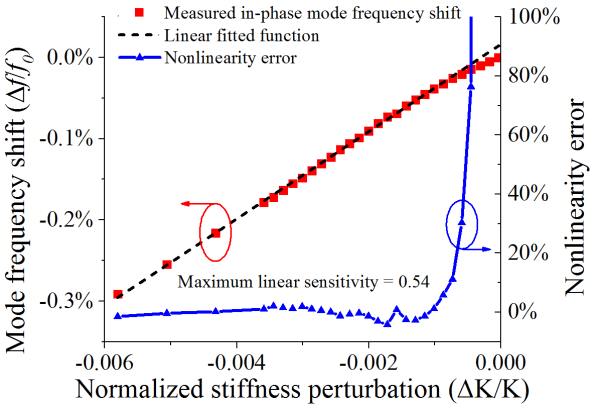

Figure 6.14: Measured in-phase mode frequency shift as a function of normalized stiffness perturbation, together with a linear fitted function and nonlinearity error. The linear sensitivity was 0.54.

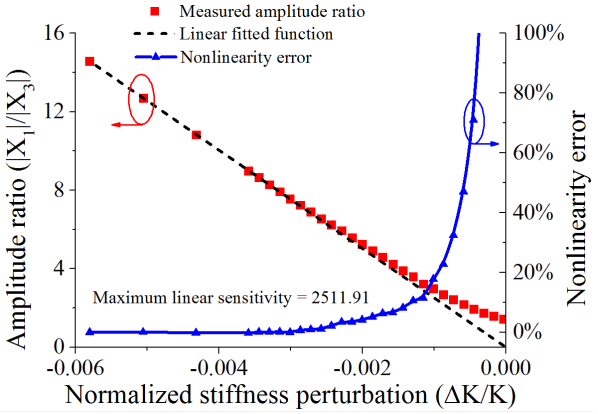

Figure 6.15: Measured amplitude ratio (quotient of vibration amplitudes of resonator 1 and 3) as a function of normalized stiffness perturbation. Also shown is a linear fitted function and the nonlinearity error. The linear linear sensitivity was 2511.91.

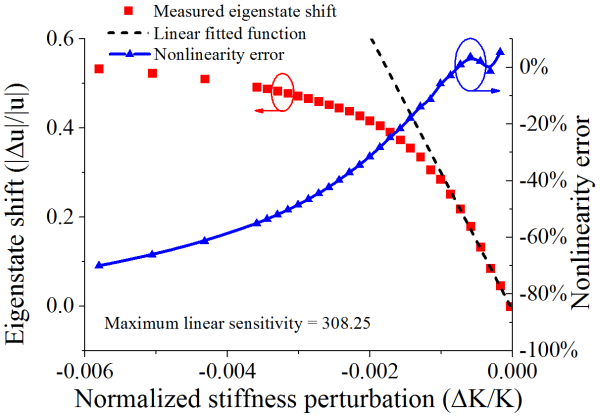

Figure 6.16: Measured eigenstate shift as a function of normalized stiffness perturbation, along with linear fitted function and nonlinearity error. The linear sensitivity was 308.25.

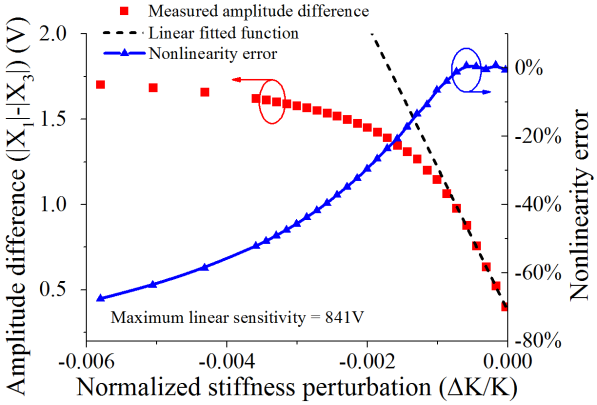

Figure 6.17: Measured amplitude difference of resonator 1 and 3 as a function of normalized stiffness perturbation, as well as a linear fitted function and nonlinearity error. The maximum linear sensitivity was 841V.

signals. Therefore it can be concluded that amplitude ratio is an optimum output for the 3DoF resonator sensor in terms of sensitivity and linearity. Whereas amplitude difference can be another attractive output as it gives a very high sensitivity, which is technically incomparable to the other three due to the different unit, at the expense of a smaller linear range.

Hence, we have used amplitude ratio as the output for the 3DoF weakly coupled resonator sensor.

6.5.1.4 Dynamic range

To avoid strong mode aliasing as shown in Figure 6.13(a), the anti-aliasing condition given by Equation 4.43 should be satisfied. For the bandwidth measured in the experiment, the minimum frequency difference required was:

$$\Delta\omega > 2 \times \Delta\omega_{3\text{dB}} = 4.8\text{Hz} \tag{6.15}$$

Mode frequency measurements were carried out for coupling voltages of 30V, 34.5V, 40V and 45V, to find the boundary of the perturbation values to satisfy Equation 6.15. The case with 50V coupling voltage was not analysed here since all negative stiffness perturbations satisfied Equation 6.15, hence were all in the dynamic range. The frequency differences versus stiffness perturbations are plotted in Figure 6.18, together with the theoretically calculated frequency differences Equation 5.1e using extracted γ_3 and offset values listed in Table 6.3. The measured frequencies matched well with the theoretical calculations.

The lower boundary of the dynamic range was limited by the noise of the resonator and the associated circuitry interface, as discussed in Section 5.2. In our experiment,

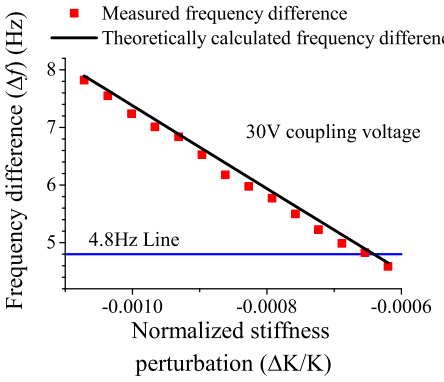

(a) Mode frequency difference with 30V coupling voltage

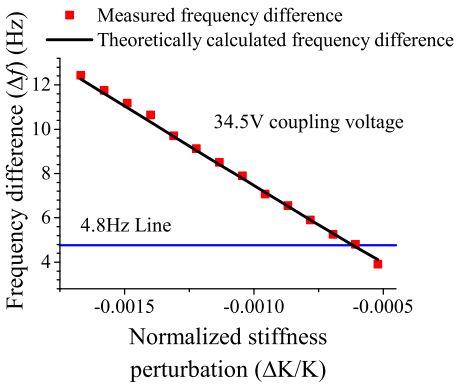

(b) Mode frequency difference with 34.5V coupling voltage

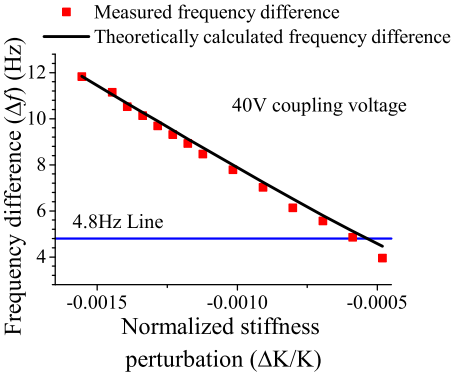

(c) Mode frequency difference with 40V coupling voltage

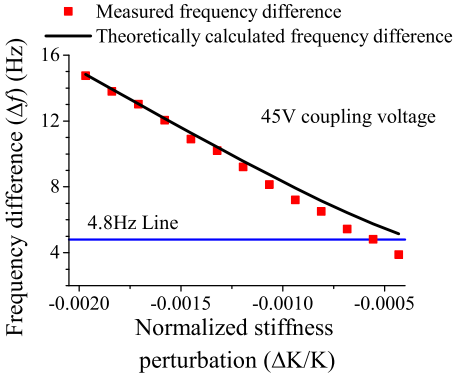

(d) Mode frequency difference with 45V coupling voltage

Figure 6.18: Measured and theoretically calculated frequency differences (Equation 5.1) with different coupling voltages: a) 30V coupling voltage, b) 34.5V coupling voltage, c) 40V coupling voltage, d) 45V coupling voltage. The measured frequency differences matched well with the theoretical calculations.

Table 6.5: Dynamic range in terms of normalized change in stiffness

Coupling voltage (V)	Extracted γ_3	Upper boundary of $\Delta K/K$	Lower boundary of $\Delta K/K$	dynamic range of $\Delta K/K$
30	13358	-6.54×10^{-4}	-3.78×10^{-3}	3.12×10^{-3}
34.5	9118	-6.07×10^{-4}	-5.49×10^{-3}	4.89×10^{-3}
40	5534	-5.89×10^{-4}	-9.05×10^{-3}	8.46×10^{-3}
45	3538	-5.58×10^{-4}	-14.77×10^{-3}	14.2×10^{-3}

for decreasing perturbations, the amplitude of resonator 3 became smaller, consequently limiting the maximum amplitude ratio that could be detected. The measured output noise for resonator 3 without driving signal was approximately 3mVrms. This was measured using the averaging acquirement function of the oscilloscope. To ensure a signal to noise ratio of at least 10dB, the minimum detectable voltage amplitude from resonator 3 was regarded as at least 30mV, resulting in maximum amplitude ratios between approximately 50 to 52 in four different measurement sets.

The boundaries of the dynamic range of the sensor for different coupling voltages are listed in Table 6.5.

6.5.1.5 Amplitude ratio and sensitivity analysis

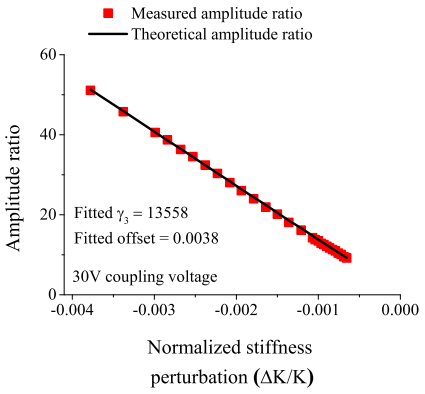

(a) Amplitude ratio with 30V coupling voltage

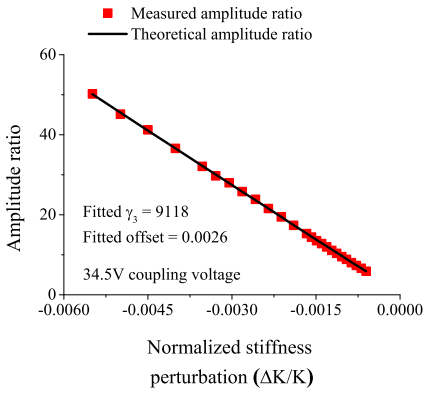

(b) Amplitude ratio with 34.5V coupling voltage

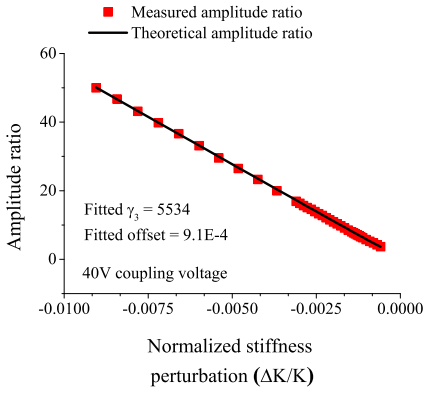

(c) Amplitude ratio with 40V coupling voltage

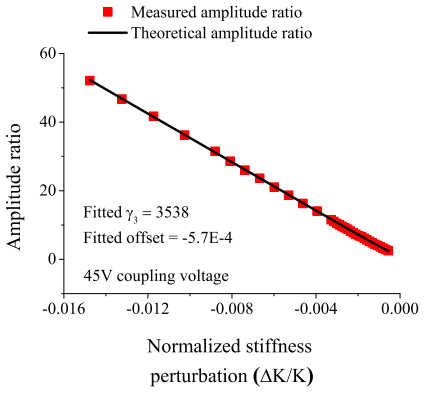

(d) Amplitude ratio with 45V coupling voltage

Figure 6.19: Measured and theoretically estimated amplitude ratio using Equation 4.44 with different coupling voltages: a) 30V coupling voltage, b) 34.5V coupling voltage, c) 40V coupling voltage, d) 45V coupling voltage. The measurement results matched well with theoretical predictions.

The estimated theoretical amplitude ratios using extracted γ_3 values, measured quality factor and Equation 4.44 are depicted in Figure 6.19, together with fitted offset values introduced by fabrication variances.

From Figure 6.19, it can be seen that the measured results matched well with the theoretical predictions, with a relative error smaller than 5% in all cases.

The measurement result also showed that a smaller coupling voltage lead to a higher amplitude ratio for a given perturbation stiffness, thus a higher sensitivity. The linear sensitivity of the sensor, extracted from the measurement data, together with the sensitivity calculated using design values are listed in Table 6.6.

Table 6.6: Sensitivity analysis

Coupling voltage (V)	Linear sensitivity extracted from measured data	Sensitivity calculated using design parameters	Relative error
30	−13558	−17073	−20.59%
34.5	−9118	−9656	−5.57%
40	−5534	−5250	5.40%
45	−3538	−3259	8.56%

The discrepancies between measured and ideal data were attributed to fabrication variances, and due to the high sensitivity of the device, small parameter variations were also amplified.

6.5.1.6 Nonlinearity

To calculate the total nonlinearity errors, the measured data was compared to the linearized scale function Equation 5.11. The results are plotted in Figure 6.20 (the next page).

From Figure 6.20, it is found that the theoretically estimated nonlinearity errors matched well with the measured errors. Also, as predicted by theory, the nonlinearity error tended to increase as the stiffness perturbation approached zero; and with decreasing γ_3 value, the maximum nonlinearity error in the dynamic range increased. Nonetheless, for a wide span of stiffness perturbations, the sensor provides good linearity, with a typical nonlinearity error smaller than $\pm 2\%$.

6.5.1.7 Discussion

From the measurement results, we obtained the linear sensitivity of the sensor (device 1). Comparing the measured linear sensitivity to the state-of-the-art resonator sensors reported in the literature, a significant improvement in sensitivity is noticed. A brief comparison of the sensitivity is shown in Table 6.7.

Table 6.7: Sensitivity comparison with the state-of-the-art resonator sensors for stiffness change

Reference	Sensitivity	Type
[61]	0.5	1DoF resonant sensor
[108]	~ 20	2DoF resonant sensor
[121]	~ 275	2DoF resonant sensor
Our work	~ 13558	3DoF resonant sensor

It is seen from Table 6.7 that the improvement in sensitivity was significant: compared to the conventional single resonator sensor with frequency shift output, the improvement

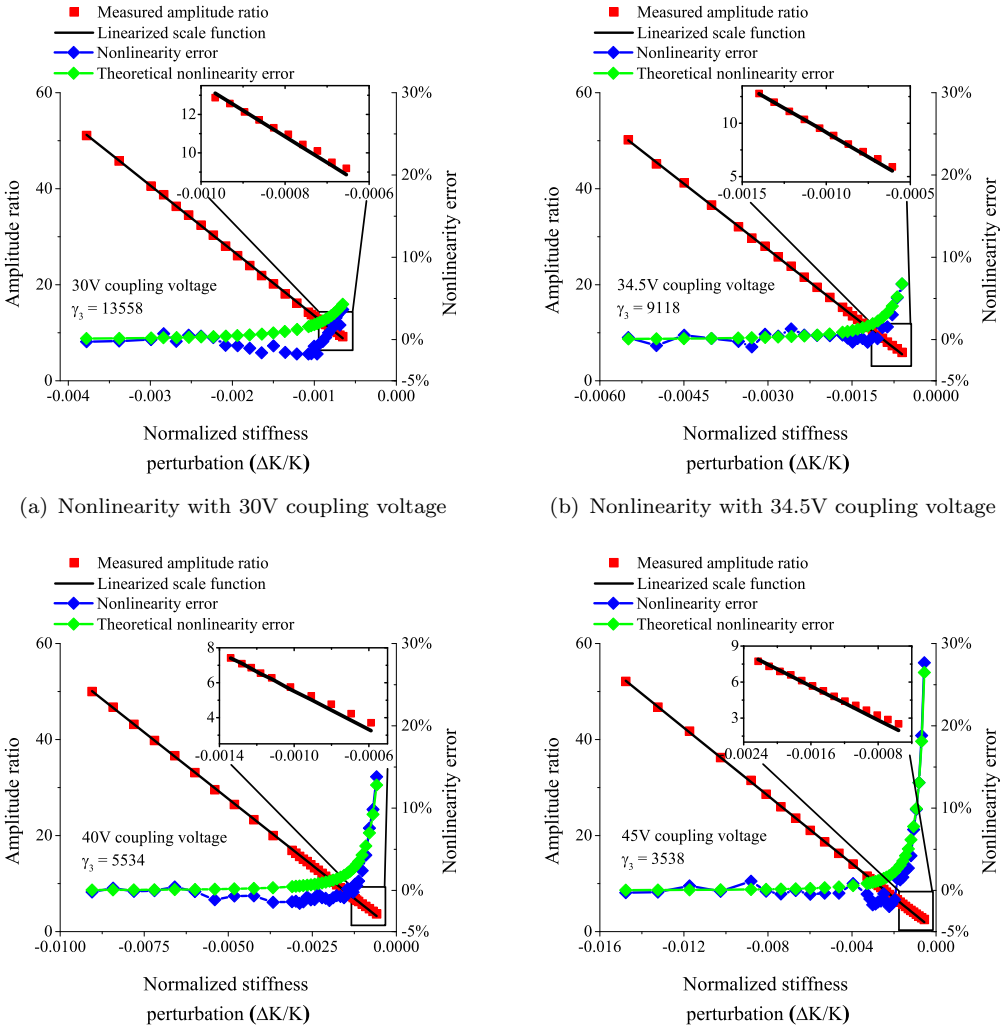

(a) Nonlinearity with 30V coupling voltage

(b) Nonlinearity with 34.5V coupling voltage

(c) Nonlinearity with 40V coupling voltage

(d) Nonlinearity with 45V coupling voltage

Figure 6.20: Comparison of measured amplitude ratio to linearized scale function (Equation 5.11) with different coupling voltages: a) 30V coupling voltage, b) 34.5V coupling voltage, c) 40V coupling voltage, d) 45V coupling voltage. The nonlinearity error was calculated by comparing the measured amplitude ratio to linearized scale function given by Equation 5.11 and displayed in blue. The theoretical nonlinearity error was calculated using, $\epsilon_1 + \epsilon_2$, where ϵ_1 and ϵ_2 were calculated using Equation 5.18 and Equation 5.20, respectively. The theoretically estimated nonlinearity errors matched well with measured errors.

was over four orders of magnitude; whereas the improvement in sensitivity compared to the 2DoF sensor utilizing mode localization was over 49 times.

It can be found from the measurement results that the dynamic range was not large (Table 6.5). This was due to a relatively high value of minimum detectable stiffness change. One way to enhance the dynamic range is to add a perturbation bias intentionally, so that any further perturbation in stiffness, will result in a total value of perturbation in stiffness larger than the minimum detectable level. Hence the minimum detectable

stiffness change is ultimately limited by the noise floor of the sensing system (e.g. device and interface electronics).

Another property of the sensor is that the nonlinearity of sensor is not trivial for a stiffness perturbation approaching zero. This could be alleviated by adding a stiffness perturbation bias intentionally to a point above which nonlinearity error is tolerable for the intended applications.

Combining these two reasons, bias stiffness perturbations can be a good strategy to improve both dynamic range and in range linearity. To demonstrate this, we tested the functionality of device 2.

6.5.2 Experimental results of device 2

To test device 2, three DC voltages were used in the experiment: a) a fixed coupling voltage of $V_c = 12\text{V}$ was applied to resonators 1 and 3, while resonator 2 was grounded, hence the resonators were electrostatically coupled; b) a variable voltage V_b, the value of which will be discussed later, was used to bias the 3DoF sensor to an appropriate operating point; c) a variable voltage $V_e < 0$ was used to apply a tensile force on resonator 1. This is shown in Figure 6.8.

6.5.2.1 γ_3 and offset values extraction

Before proceeding to demonstrate the force sensor, γ_3 and stiffness offset values were extracted due to their importance in analysing the experimental results as mentioned above. γ_3 indicates the sensitivity in particular, as shown by Equation 4.17a.

As shall be seen later in Figure 6.22, unlike device 1, the amplitude ratio bent downward from a linear function for amplitude ratios larger than 20, we were unable to use the same extraction approach as for device 1. Therefore, we used an alternative approach, that is to fit the amplitude ratios smaller than 20 to Equation 4.44. To do this, the Q-factor of the device 2 was measured from frequency responses. The 3dB bandwidth of the out-of-phase mode was found to be 0.48Hz, the quality factor was 28653, as shown in Figure 6.21.

While ensuring the mode aliasing effect was negligible and with V_e kept at 0V, the bias voltage V_b, as shown in Figure 6.8, was altered to change $\Delta K/K$ for γ_3 and offset extraction. The amplitude ratios were recorded for different $\Delta K/K$, and the amplitude ratio curve was fitted to Equation 4.44, as shown in Figure 6.22. The extracted values of γ_3 and the offset in normalized stiffness are 29119 and 5.16×10^{-4}, respectively. Compared to the theoretically calculated value of $\gamma_3 = 39557$ from the designed dimensions, the relative error is approximately 26%, this is due to the variances introduced during the fabrication process.

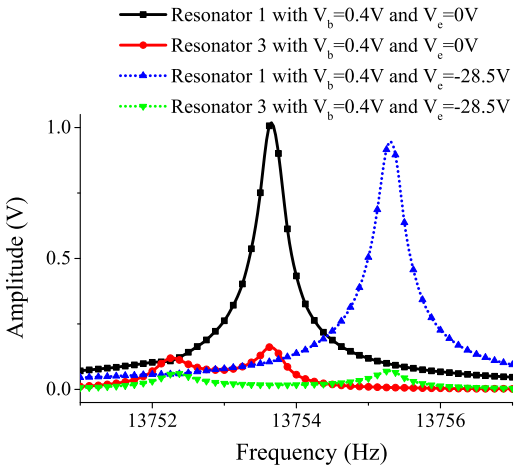

Figure 6.21: Measured frequency response of resonator 1 and 3 under two different perturbation conditions: a) $V_b = 0.4$V and $V_e = 0$V, shown in solid lines; b) $V_b = 0.4$V and $V_e = -28.5$V, shown in dotted lines. The quality factor was calculated to be 28653.

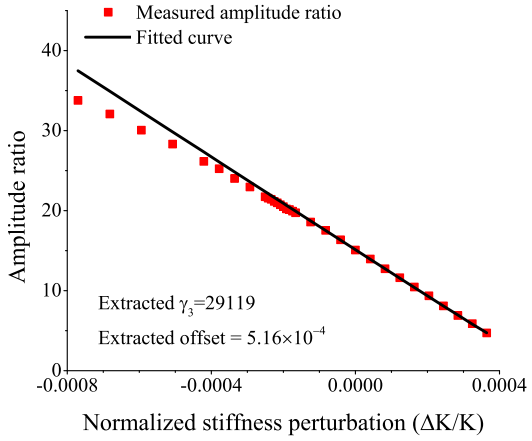

Figure 6.22: Measured amplitude ratios (in red dots) were fitted to Equation 4.44 to extract γ_3 and offset value in normalized stiffness perturbation. The fitted curve is shown in black. The extracted $\gamma_3 = 29119$ and offset $= 5.16 \times 10^{-4}$.

6.5.2.2 Bias point selection

A bias stiffness perturbation ΔK_{bias} was intentionally introduced in the experiment, in order to avoid the mode aliasing effect, thus to improve both dynamic range and in-range linearity. This was achieved by applying a fixed bias voltage V_b. To reduce the mode aliasing effect, the anti-aliasing condition Equation 4.43 should be satisfied.

A mode frequency measurement was carried out to find the range of perturbation voltage V_b that satisfies Equation 4.43. The results are shown in Figure 6.23. It is shown that a perturbation voltage of $V_b \leq 0.5$V satisfied the anti-aliasing condition.

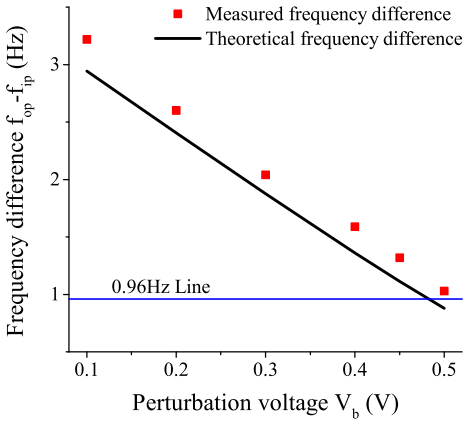

Figure 6.23: Measured (black) and theoretically calculated (red) frequency difference as a function of perturbation voltage V_b. The theoretical frequency differences were calculated using equation Equations 4.20 and 4.22 with γ_3, offset value extracted and the designed dimensions. $2f_{3dB} = 0.96$Hz is marked with a blue line in the figure. Measured frequency differences match well with theoretical calculated values.

Moreover, as shown by previous simulation results, a negative ΔK_{bias} with larger magnitude, therefore, a lower V_b, is desired for improved linearity. In the meantime, however, as shown in Equation 5.21, a larger $|\Delta K|$ leads to a larger $|X_1/X_3|$, hence leading to larger noise in the amplitude ratio. Therefore, to balance the trade-off, $V_b = 0.4$V was used for perturbation. The corresponding normalized stiffness perturbation $\Delta K_{\text{bias}}/K$ and amplitude ratio were 1.91×10^{-4} and 5.75, respectively.

6.5.2.3 Force measurement

The main purpose of testing device 2 was to demonstrate the functionality of the 3DoF weakly coupled resonator device for axial force sensing applications. To demonstrate this functionality, electrostatic forces along the beam length were created by applying V_e to the electrode for resonator 1.

With $V_e < 0$ applied, a tensile force was exerted on resonator 1, which added a positive stiffness perturbation to resonator 1. As discussed in Section 4.3.3, this in effect was equivalent to decreasing ΔK to resonator 3. Hence the frequency difference Δf increased and the mode aliasing effect could be neglected, as shown by the dotted curves in Figure 6.21. It can also be seen from Figure 6.21 that negligible spring nonlinearity was present; therefore the assumption of linear springs can be regarded as valid.

By varying V_e, we were able to measure the amplitude ratios. Using Equation 6.13, the effective tensile forces applied were calculated. Hence, we can obtain the theoretical

amplitude ratio using Equations 4.44 and 6.14. Figure 6.24 shows the measured amplitude ratios and linearized scale function, given by Equation 5.11, together with the nonlinearity error. It can be seen from Figure 6.24 that the measured amplitude ratio matched well with the linearized scale function, with a nonlinearity error smaller than 10% for all the data points. The linear force sensitivity was found to be 4.9×10^6/N. The theoretical force sensitivity is calculated to be 6.6×10^6/N. The relative error compared to theoretical prediction is -26%, which is attributed to fabrication tolerances.

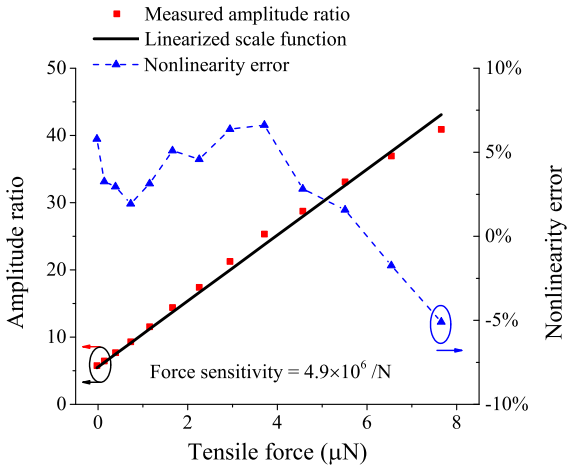

Figure 6.24: Measured amplitude ratios and the linearized scale function with respect to the applied tensile force. The measured amplitude ratios matched well with the linearized scale function, with nonlinearity error smaller than 10% for all the data points. The force sensitivity is found to be 4.9×10^6/N.

A comparison of sensitivity to other state-of-the-art resonant force sensors is listed in Table 6.8. It can be seen that significant improvement in sensitivity of at least two to three orders of magnitude was achieved.

Table 6.8: Sensitivity comparison with state-of-the-art resonant force sensors

Reference	Type	Sensitivity expression	Sensitivity (/N)
[31]	1DoF resonator with differential sensing and leverage	$\frac{\partial(\Delta f/f)}{\partial T}$	8995
[121]	2DoF resonant sensor	$\frac{\partial(\text{Eigenstates shift})}{\partial T}$	1478
Our work	3DoF resonator sensor	$\frac{\partial(\text{Amplitude ratio})}{\partial T}$	4.9×10^6

6.5.2.4 Force resolution and dynamic range

Since any motion caused by mechanical noise (as discussed in Section 5.7) went through the same amplification stages on the printed circuit board, the output mechanical SNR of the ith resonator is:

$$\mathrm{SNR}_{m,i} = \frac{V_i^2 K_{\mathrm{eff}}}{k_B T (2\omega_{op}\eta_s R_f G_{\mathrm{INA}})^2}, \quad i = 1 \text{ or } 3 \tag{6.16}$$

where V_i is the rms-value of the output voltage of the ith resonator and G_{INA} are the differential gain of the instrumentation amplifiers.

From Equations 5.27 and 5.28, the electrical SNR at the output can be computed as:

$$\mathrm{SNR}_{e,i} = \frac{V_i^2}{(\sqrt{2} i_{n,i} R_f G_{\mathrm{INA}})^2}, \quad i = 1 \text{ or } 3 \tag{6.17}$$

The noise spectral density was measured using a two channel dynamic signal analyser (35670A by Agilent Technologies) without any driving signal applied, while $V_c = 12$V, $V_b = 0.4$V and $V_e = 0$V were retained. Averaging of 50 measurement results were used to reduce the measurement variation, hence the peak caused by the mechanical noise could be found. The theoretical noise was calculated using Equations 6.16 and 6.17, together with the equations in section 5.7. It can be seen from Figure 6.25 that the measurement results and theoretical predictions agreed well. Therefore we were able to evaluate the noise power based on the theoretical noise.

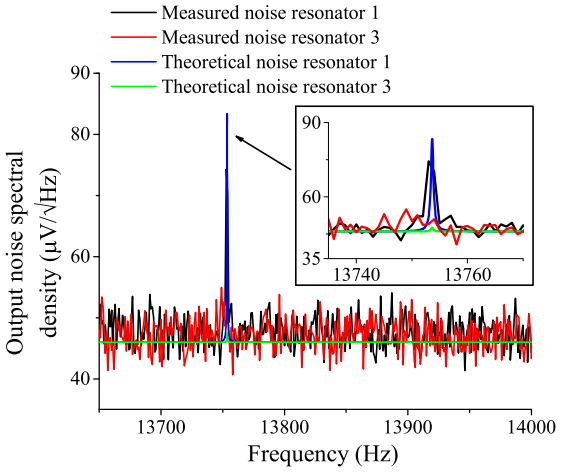

Figure 6.25: Output voltage noise spectral density of resonators 1 and 3 compared to the theoretically estimated noise density. The measured noise floor agreed well with theoretical calculations.

Assuming an ambient temperature of 290K, using the sensing transduction factor, $\eta_s = 4.01\times10^{-8}$A/(m·rad/s), calculated using the designed value from Table 6.1, $R_f = 6.6$MΩ and $G_{\mathrm{INA}} = 100$ as designed, when $V_b = 0.4$V and $V_e = 0$V, resulting in an amplitude ratio $|X_1/X_3| = 5.75$, the SNRs can be calculated from the noise power within 3dB bandwidth ($f_{3dB} = 0.48$Hz) using the measured output signal. The evaluated SNR and noise power are listed in Table 6.9.

Table 6.9: Theoretical noise evaluation of the 3DoF sensor

Noise type	Measured signal power	Evaluated SNR (dB)	Evaluated Noise power
Mechanical noise (resonator 1)	0.53 (V^2)	84.80	1.76×10^{-9} (V^2)
Mechanical noise (resonator 3)	1.60×10^{-2} (V^2)	84.80	5.30×10^{-11} (V^2)
Electrical noise (resonator 1)	0.53 (V^2)	87.18	1.02×10^{-9} (V^2)
Electrical noise (resonator 3)	1.60×10^{-2} (V^2)	71.98	1.02×10^{-9} (V^2)
Amplitude ratio noise	33.11	71.72	2.23×10^{-6}

It can be seen from Table 6.9 that the electrical noise of resonator 3 (the resonator with smaller amplitude) ultimately sets the noise floor of the amplitude ratio. Due to the fact that the thermal-electrical noise can be regarded as uniformly distributed in a wide frequency span, the amplitude ratio noise can also be regarded as white noise. Therefore, from Table 6.9, we can evaluate the minimum resolvable force of the sensor near the bias point as:

$$\begin{aligned} \langle T \rangle_{min} &= \frac{\langle \text{Amplitude ratio} \rangle_{min}}{\text{Force sensitivity}} \\ &= \frac{\sqrt{2.23 \times 10^{-6}/0.48}}{4.9 \times 10^{6}} \text{N}/\sqrt{\text{Hz}} \\ &= 4.40 \times 10^{-10} \text{N}/\sqrt{\text{Hz}} \end{aligned} \tag{6.18}$$

where $\langle \text{Amplitude ratio} \rangle_{min}$ is the evaluated noise power spectral density of the amplitude ratio.

To estimate the dynamic range of the 3DoF sensor, suppose a bandwidth of 10Hz, the minimum detectable force is 1.39nN. For a maximum force of 7.6μN in the experiment, a dynamic range of approximately 74.8dB can be achieved.

6.5.2.5 Nonlinearity

From the measurement results, it can be noticed that the nonlinearity error of the 3DoF device started off decreasing in value as the amplitude ratio increased, as shown in Figure 6.26, which was in agreement with the theoretical predictions.

However, the linearity of the 3DoF sensor tended to deteriorate as the amplitude ratio increased, as shown in Figures Figure 6.24 and 6.26. It should be noticed that this

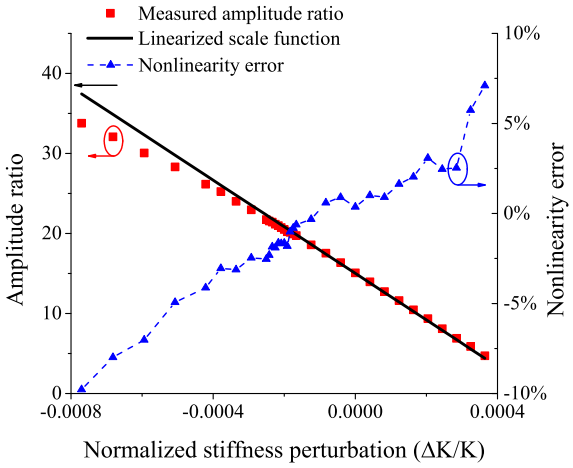

Figure 6.26: Measured amplitude ratio and the linearized scale function Equation 5.11 as a function of normalized stiffness perturbation. Nonlinearity error was also calculated and shown in the figure. Nonlinearity error decreased in value as the amplitude ratio increased.

nonlinearity was found to be insignificant for the device 1. One possible reason for this is that the air gap between the resonators was 3.5μm in this design, smaller compared to 4.5μm of device 1. For example, when amplitude of resonator 1 is significantly higher than resonator 3 (larger than 30 times), the nonlinearity of K_{c1} becomes larger than that of K_{c2}, making the assumption of $K_{c1} = K_{c2}$ invalid for larger amplitude ratios.

6.6 Summary

In this chapter, an experiment to verify the theoretical predictions of a 3DoF weakly coupled resonator device as a sensor for stiffness change applications, including tensile force sensing, is demonstrated. The design of a proof-of-concept device with 3DoF electrostatically coupled resonator structure is presented, along with the fabrication process and the electrical experimental set-up. The devices were for proof-of-concept. Despite so, some design considerations such as differential sensing, double parallel plate and L-shaped beam designs can be helpful for future optimization of the device.

The experimental results from two fabricated devices are also presented in this chapter. In general, the measurement results agreed well with our theoretical predictions. For instance, from the measurement results, it was demonstrated that the amplitude ratio $|X_1|/|X_3|$ was the optimum output signal in terms of linear sensitivity and linear range, when compared to other output metrics such as eigenstate shift and frequency shift.

The most significant discovery from the experimental results was that a 3DoF weakly coupled resonator device can provide much higher sensitivity than a conventional single DoF resonator sensor or a 2DoF weakly coupled mode-localized resonant sensors. At

least 49 times improvement in sensitivity for stiffness change applications (device 1) and two orders of magnitude enhancement in force sensitivity (device 2) were observed in the experiments. This makes the novel 3DoF weakly coupled resonator sensor an attractive alternative for ultra-high sensitivity applications.

From the measurement results, the feasibility of utilising a bias point was also demonstrated. This allows the manipulation of the working range for optimizing the performance of the sensor.

In addition, the noise level of the force sensor was also theoretically estimated based on the noise spectrum density measurement. Hence the dynamic range was also calculated based on the noise estimation. From the proof-of-concept design (device 2), a dynamic range of 74.8dB was achieved. This is also promising for future optimization.

However, one disadvantage of the device was the nonlinearity. From the measurement results of both device 1 and 2, it was shown that the nonlinearity of the device was not trivial in a wide range. This requires more optimization in the future.

Chapter 7

Self-oscillating Loop

Throughout this dissertation, it was repeatedly stated that this research is intended to lay the theoretical foundation of the 3DoF weakly coupled resonator as a stiffness change sensor. Some practical problems still remains unsolved to this point, e.g. no self-oscillating loop control circuit structure existed in the literature. Hence, in this chapter, we shall propose a feasible structure for constructing such a loop, potentially enabling automatic locking to the resonance mode of interest.

7.1 Introduction

For the experimental method in this research, one major problem exists currently, that is the observer has to adjust the frequency of the drive signal to the out-of-phase mode frequency, so that the amplitudes of resonators 1 and 3 at the out-of-phase mode frequency could be measured, when a stiffness perturbation is introduced. Since the tuning of the drive frequency to the exact mode frequency can be time consuming, this makes the device impractical for applications where fast changing stiffness change or force change should be monitored. Therefore, it is imperative to develop a self-oscillating loop or self-sustained oscillation loop, which automatically locks the resonator system to the out-of-phase mode, even when a stiffness perturbation is present.

In the literature, self-oscillating loop has been used for single DoF resonators [31, 81, 122, 123, 124], in order to keep the resonators always excited at the desired resonant frequencies. However, to the author's knowledge, there is no report on a self-oscillating loop design for a weakly coupled resonator system.

In what follows, we shall propose an approach to design the self-oscillating loop that automatically finds the out-of-phase mode frequency of a 3DoF weakly coupled resonator system, and discuss the feasibility of such a feedback loop.

7.2 Theory

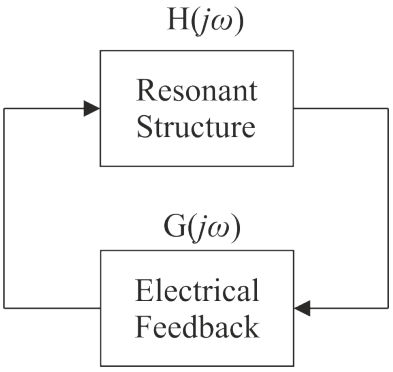

Figure 7.1: Typical structure of a self-oscillating loop, where $H(j\omega)$ and $G(j\omega)$ are the transfer functions of the resonant structure and electrical feedback, respectively.

For a self-sustained oscillator as shown in Figure 7.1, the oscillation start-up condition is derived from the Barkhausen criterion [125]:

$$\angle[H(j\omega_0)G(j\omega_0)] = 0 \tag{7.1a}$$

$$|H(j\omega_0)G(j\omega_0)| > 1 \tag{7.1b}$$

where ω_0 is the oscillator's desired angular frequency. However, as the oscillation grows, the maximum amplitude of the oscillation would be limited by either a nonlinearity or an amplitude limit set by the designer [81]. Since the nonlinearity of the resonant structure is not desired in our 3DoF resonator sensor, the amplitude of oscillation is intentionally limited to a level well within the linear region of the springs. This can be achieved by designing an automatic level controller circuit, i.e. the automatic gain control (AGC) [124]. With the AGC in effect, the feedback gain block $G(j\omega)$ is reduced as the amplitude of the oscillation grows. When the amplitude of oscillation reaches the desired value, the magnitude of the feedback loop gain $|H(j\omega_0)G(j\omega_0)| = 1$.

As opposed to the fact that the design of the AGC and the variable gain feedback is well documented in the literature, the self-oscillating loop has not yet been achieved for a coupled resonator system. This is because of that the transfer function of a coupled resonator system has not been discussed in the literature so far. For a 3DoF weakly coupled resonator system, when $|\gamma_3(\Delta K/K)| > 10$:

$$|\gamma_3(\Delta K/K)| \approx \sqrt{\gamma_3^2(\Delta K/K)^2 + 4} \tag{7.2}$$

From Equation B.2b in Appendix B, it can be seen that in this case, $U_1(j\omega_{op})$ has a phase difference of approximately 0 degrees compared to F_1. Hence, the motional current is in-phase with the AC drive voltage. Thus if we use the amplitude of the motional current of resonator 1, which is proportional to U_1 as the signal to feedback, the total phase shift of the electrical feedback should be 0 degrees.

7.3 Simulation to demonstrate the feasibility

7.3.1 Self-oscillating loop schematic

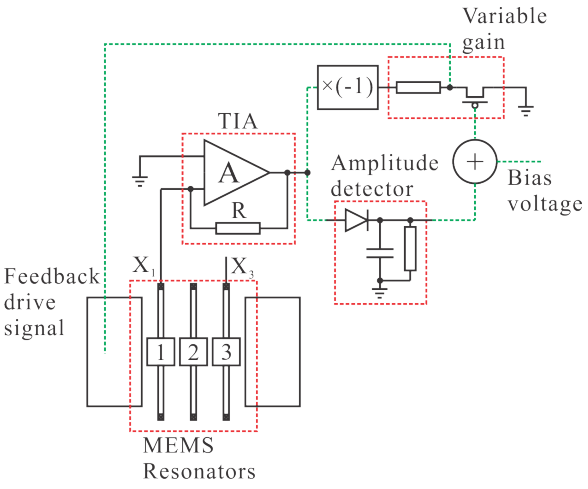

Figure 7.2: Simplified schematic of the self-oscillating loop, including the MEMS resonators.

The entire configuration of the self-oscillating loop, including the MEMS resonator, is shown in Figure 7.2.

The electrical feedback includes a standard transimpedance amplifier (TIA) and a variable gain structure in conjunction with an amplitude detector. The standard transimpedance amplifier was used to convert the motional currents into voltages.

The variable gain stage used the voltage converted from the motional current of the resonator 1 as the input, with the gain controlled by the amplitude of the same resonator, it reduces gain for the increasing amplitude, and increases the gain for the decreasing amplitude. Hence, the oscillation can be maintained. To realize this function, a structure based on the circuit proposed by [126] was used. An amplitude detector, shown as the amplitude detector in Figure 7.2 was employed to generate the control signal. A voltage controlled resistor, which is a MOSFET working in the triode region, as shown in Figure 7.2 was used to vary the gain.

7.3.2 Simulation results

The circuit diagram for the simulation is shown in three parts as in Figure 7.3.

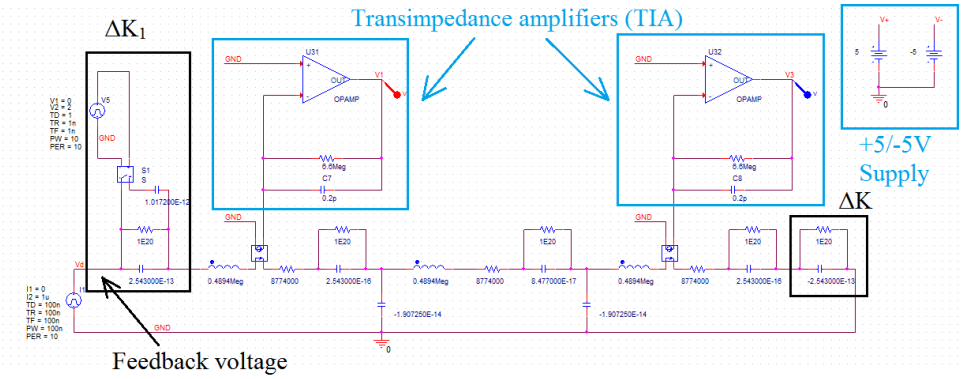

(a) MEMS resonator model

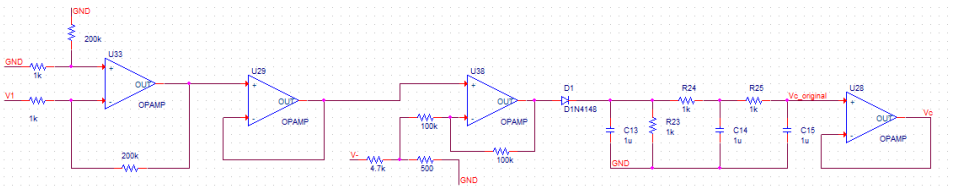

(b) Amplitude detection

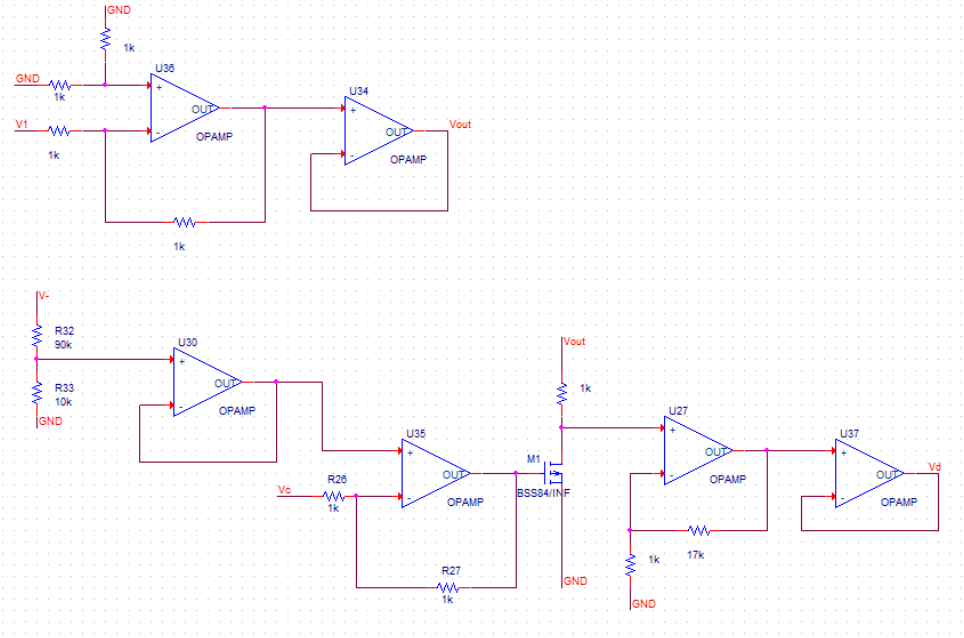

(c) Variable gain stage

Figure 7.3: Circuit diagram for the self-oscillating loop simulations: a) MEMS resonator model; b) amplitude detection for the loop gain control; c) variable gain stage to generate drive voltage.

The first part is the 3DoF RLC circuit model equivalent to MEMS resonator with both stiffness perturbations to resonators 1 and 3, as shown in Figure 7.3(a). The value for

the RLC components used for the simulations is listed in Table 4.4. A constant stiffness perturbation of $\Delta K/K = -0.001$ was introduced to the resonator 3. The normalized stiffness perturbations shown in the figures below are the stiffness perturbations to resonator 1. The TIAs were used to convert the motional currents to voltages V_1 and V_3, which is the amplitude of resonator 1 and 3, respectively.

The second part is the amplitude detection circuitry to generate the signal, V_c to control the loop gain. The control signal, V_c follows the trend of the amplitude change: it increases as the amplitude increases, decreases as the amplitude decreases. The voltage fed to the diode was forward biased so that it could detect any small amplitude change. The set up of this part of circuit is shown in Figure 7.3(b).

The third part is the variable gain stage, which was used to generate the drive voltage V_d. The gain control element was a P-channel MOSFET. To ensure that the MOSFET was always on, the gate voltage was biased to -1VDC. The small amplitude of V_{out} ensured that the transistor was always in the triode region, hence the transistor can be used as a variable resistor controlled by V_c. The r_{DS} of the transistor decreases as the voltage V_c increases, thereby decreasing the loop gain. The generated voltage V_d was then fed back to drive the MEMS resonators. The circuit schematic of this part is shown in Figure 7.3(c).

Without any drive signal, except for a short pulse current source to kick start the oscillation, the transient responses of the resonator 1 and 3 within the self-oscillating loop are shown in Figures 7.4(a) and 7.4(b), respectively. From the start of the simulation, $t = 0$, the normalized stiffness perturbation to resonator 1 was $\Delta K/K = 10^{-3}$. From $t = 1$, the normalized stiffness perturbation suddenly changed to $\Delta K/K = 2 \times 10^{-4}$. It can be seen from the figures that the amplitude of the resonator 1 was kept constant due to the automatic gain control, while the change in the amplitude of resonator 3 can be clearly seen.

The steady state transient responses of the resonators 1 and 3, under the two stiffness perturbations, are shown in Figures 7.5(a) and 7.5(b), respectively. It can be seen from Figures 7.5(a) and 7.5(b) that the phase differences between the amplitudes of resonators 1 and 3 are close to 180 degrees.

In addition to the transient response, we shall examine the oscillation frequencies of the self-oscillating loop, to see whether the feedback is able to track the out-of-phase mode frequencies when the perturbation is changed. The simulated period of one cycle for each stiffness perturbation was calculated by evaluating the time period for approximately 140 cycles (which is within a 0.01 second window) in the simulation, and dividing that time by the number of cycles. The oscillation frequencies were then calculated from the period of a cycle. The oscillation frequencies calculated from the simulations as a function of the stiffness perturbation is plotted and compared to theoretical out-of-phase mode frequencies (Equation 4.46b) in Figure 7.6.

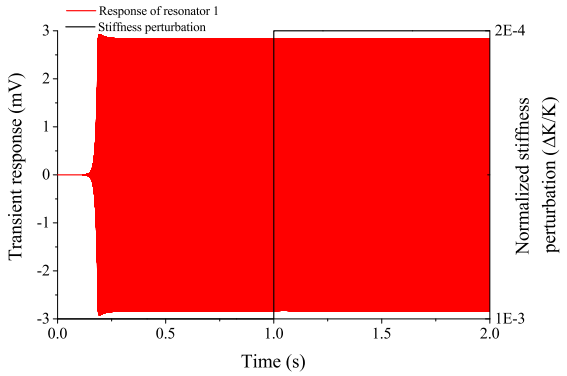

(a) Transient of resonator 1

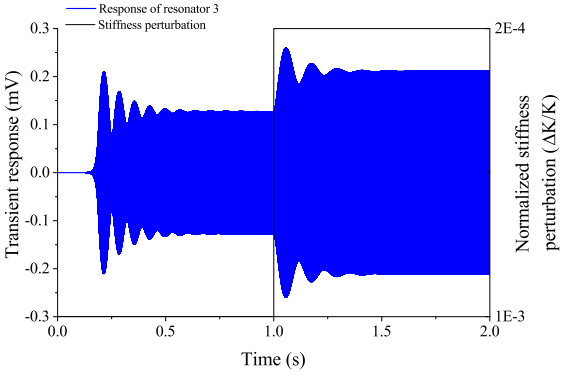

(b) Transient of resonator 3

Figure 7.4: Simulated transient responses of: a) resonator 1 and b) resonator 3, subject to changing stiffness perturbation to the resonator 1.

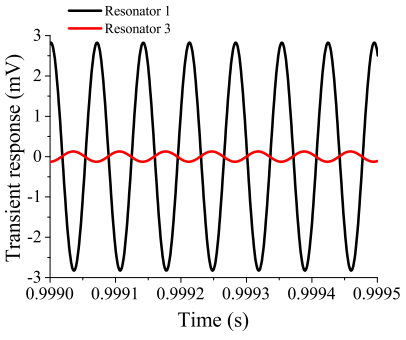

(a) $\Delta K/K = 10^{-3}$

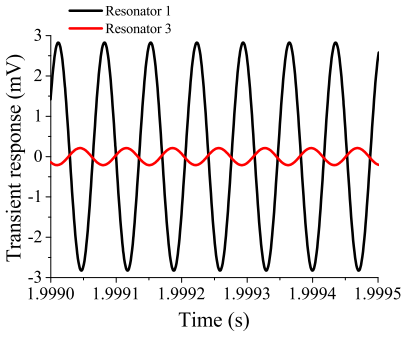

(b) $\Delta K/K = 2 \times 10^{-4}$

Figure 7.5: Simulated steady state transient responses of the resonators 1 and 3 with different stiffness perturbations to the resonator 1: a) $\Delta K/K = 10^{-3}$ and b) $\Delta K/K = 2 \times 10^{-4}$.

It can be seen from Figure 7.6 that the oscillation frequencies of the self-oscillating loop agreed well with the theoretical out-of-phase mode frequencies, with relative errors smaller than 0.003%. Hence, it can be concluded that the self-oscillating loop can track the out-of-phase mode frequency.

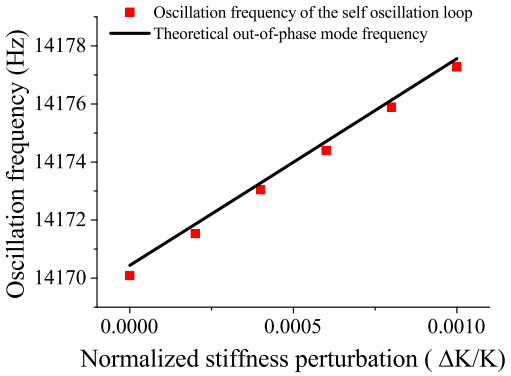

Figure 7.6: The oscillation frequencies of the self-oscillating loop calculated from the simulations compared to the out-of-phase mode frequencies of the 3DoF resonators (Equation 4.46b).

Furthermore, the amplitude ratios are also calculated from the simulation results. The steady state amplitude ratios from the self-oscillating loop as a function of the normalized stiffness perturbations were plotted and compared to the theoretical amplitude ratio (Equation 4.46c) in Figure 7.7.

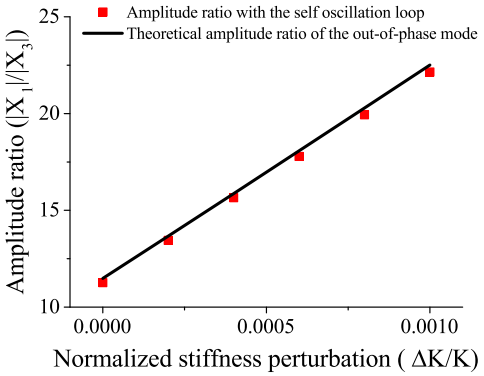

Figure 7.7: The steady state amplitude ratios from the self-oscillating loop calculated from the simulations compared to the theoretical amplitude ratios of the 3DoF resonators (Equation 4.46c).

It can be seen from Figure 7.7 that the simulated steady state amplitude ratios satisfied with the theoretical predictions, with relative error smaller than 2%. This demonstrates the feasibility of the self-oscillating loop while maintaining the functionality of the 3DoF weakly coupled resonators.

7.4 Discussions

The current structure successfully demonstrated the feasibility of the self-oscillating loop for a 3DoF weakly coupled resonator system, while maintaining the sensing capabilities

of the device. This would enable the real time sensing for a 3DoF coupled resonator device.

However, it should be pointed out that the amplitude ratios still have a relative error of approximately 2%, the reason for this could be the other modes that has not fully diminished at the "stead state". Hence, the future optimization of the self-oscillating loop can focus on approaches to damp the other modes.

Moreover, the time constant to reach a steady state, as well as the oscillation start up time, for the current configuration is quite long. For instance, it can be seen from Figure 7.4(b) that the time constant is larger than 0.1s, this would practically limit the bandwidth of the quantity to be measured to less than 10Hz. Therefore, it is important to decrease the time constant in the future.

Chapter 8

Conclusions and Future Work

8.1 Conclusions

In summary, compared to the objectives listed in Section 1.2, we have mainly achieved the following:

- Proposed a novel structure that is able to improved the sensitivity of the mode-localized sensors effectively. The resonant sensing device, which consists of three resonators, weakly coupled through electrostatic coupling to its neighbouring resonator(s), can improve the sensitivity of stiffness change or tensile force by orders of magnitude, namely 49 times for stiffness change sensors and 544 times for tensile force sensing. In terms of minimum detectable force, the calculated noise floor of the 3DoF mode-localized force sensor is $0.44\text{nN}/\sqrt{\text{Hz}}$. In addition, by adopting the bias method, a dynamic range of 74.8dB could be achieved.

  The key to improve the sensitivity for the 3DoF mode-localized sensor is to make the middle resonator at least two times stiffer, while tuning the stiffness of the coupling element at least 10 times weaker, than that of the outer resonator. In this way, a high γ_3 value can be achieved, as proposed by a key equation, Equation 4.17a.

- In this work, we have used a transfer function based approach in conjunction with an algebraic method. The algebraic method is used to solve the mode frequencies without damping. The transfer function based approach extends the theory to the practical case with damping. Using the transfer function model, we show that damping has an effect on the nonlinearity of the output of the sensor, as well as the dynamic range.

  The dynamic range and nonlinearity of the sensor were investigated. The expressions for dynamic range are given by Equations 5.3 and 5.5; the expressions for

nolinearity are estimated by Equations 5.18 and 5.20. From the expressions, it can be noticed that the sensitivity. γ_3, also affects the dynamic range and nonlinearity. Hence the value of γ_3 should be carefully designed. In addition, with the transfer functions, we were able to derive the signal-to-noise ratio of the sensor, as shown in Section 5.7. This approach can also be used on 2DoF mode-localized sensors, or for mass sensor analysis.

- Furthermore, in Sections 5.3 and 6.5.1.3, we have shown by theory and measurement results that the amplitude ratio is the optimum output signal for 3DoF mode-localized sensors, over eigenstates shift and mode frequency shift. Due to the similarities between 2DoF and 3DoF systems, we also believe that the amplitude ratios are the optimum output signal for 2DoF mode-localized sensors for stiffness changes. We have also shown that the amplitude difference can be an attractive output signal as well.
- Finally, in Chapter 7, based on the derivations using the transfer function model, we proposed a feasible self-oscillating loop structure that is capable of automatically locking to the out-of-phase mode frequency, hence enabling real-time measurements using the sensor.

However, there are other problems that need to be addressed for weakly coupled-mode localized sensors. First of all, we have demonstrated that from 1DoF to 2DoF and 3DoF resonant sensors, the sensitivity has been improved. However, would 4DoF sensor improve the sensitivity even further? Second, both 2DoF and 3DoF sensors are based on amplitude detections, which has inherently lower resolution to frequency shifts. Third, the high sensitivity of mode-localized sensors, including 2DoF and 3DoF, is based on high Q-factor of the resonant modes. It is important to improve the intrinsic Q-factor of the resonators without vacuum environment. Fourth, the common mode rejection capabilities of 3DoF has not been demonstrated, despite that it could be demonstrated in theory. These thoughts lead to the following future work beyond the thesis.

8.2 Future work

8.2.1 Extension of the theory

Due to the similarities of the 3DoF mode-localized sensors to other coupled resonant sensors, we believe that this mixed approach can be a universal approach for such systems. It can be extended and utilized in analysing other coupled resonant sensors as well, e.g. 4DoF mode-localized sensors. Since we have successfully shown that the sensitivity can be improved from 1DoF to 2DoF, then to 3DoF, it is natural to extend the number of resonators to 4 or more to achieve even higher sensitivity.

8.2.2 Resolution enhancement

For the mode-localized sensors, essentially an amplitude detection based approach is used as an output, instead of measuring the frequency shift. However, typically, the resolution of amplitude detection is orders of magnitude lower than that of the frequency shift detection. This is a drawback of the mode-localized sensors. Despite of orders of magnitude enhancement in sensitivity, the resolution of the sensor could still be the same or even lower than the conventional 1DoF sensor. Hence, it is important to optimize the resolution of amplitude detection for mode-localized sensors. One approach could be the noise shaping circuit using Sigma-Delta modulators, since the resonant frequency of the mode-localized sensor presented in this thesis is relatively low (less than 20kHz).

8.2.3 Optimization of the device design

As repeatedly stated throughout this dissertation, the design rationale of the device parameters is lacking in this research. Hence, future work should concentrate more on the optimization of the parameters. As discussed in the device design sections of this dissertation, a few trade-offs exists in the selection of parameters. Therefore, in the future, design should balance the trade-offs by prioritizing the specifications according to the applications.

Currently, there are a few limits to the performance of the device, a major one of which is the Q factor of the resonators. As discussed in the dissertation, the Q factor limits the sensitivity, linearity and dynamic range. However, for some applications where working in the atmosphere or a liquid is required, it is imperative to optimize the existing structure to lower the damping, or choose another structure that has low loss intrinsically, such as Lamé mode resonators [127].

Furthermore, another aspect that is lacking in this research is the frequency or amplitude stability of the resonators. The main reason is that this alone would require a long time to optimize. This process would involve the optimization of the fabrication process, structure, and even interface electronics for compensation.

8.2.4 Common mode rejection ability

It has been shown in previous studies [36, 41] that a 2DoF mode-localized sensor can provide improved common mode rejection compared to single DoF resonator sensor. The common mode interference to the sensing process studied included pressure and temperature changing. Based on the previous studies, it will be a very interesting topic to study the common mode rejection abilities of a 3DoF resonator sensing system. The sensitivity of the output amplitude ratio can be obtained for a known change in ambient temperature, pressure or humidity.

Appendix A

Vibration Amplitudes

A.1 Vibration amplitude of resonator 3

We consider the resonator device example in Figure 5.1, driven by an AC voltage on the actuation electrode, and the driving force bing F_1. In addition, we suppose a stiffness perturbation $\Delta K < 0$ is applied to resonator 3. From Equations 4.38a to 4.38f, we are able to obtain the vibrational amplitudes of resonators 1, 2 and 3.

Due to the symmetry of the in-phase mode and out-of-phase mode as shown in Figure 4.5, without loss of generality, only out-of-phase mode is discussed here. Assuming that the device is in the dynamic range, thus Equations 4.43 and 5.3 are satisfied, the frequency of the out-of-phase mode is given by Equation 4.20. Substituting Equation 4.20 into Equation 4.38f, we are able to approximate the vibrational displacement amplitude, X_3, and velocity amplitude, U_3, of resonator 3 at the out-of-phase mode, respectively:

$$|X_3|_{\text{op}} \approx \left| \frac{K}{Q} \left(-j\sqrt{\gamma_3^2(\Delta K/K)^2 + 4} - \frac{\gamma_3}{Q} \right) \right|^{-1} |F_1| \tag{A.1a}$$

$$|U_3|_{\text{op}} \approx \left| \frac{K}{Q} \left(-j\sqrt{\gamma_3^2(\Delta K/K)^2 + 4} - \frac{\gamma_3}{Q} \right) \right|^{-1} |\omega_{\text{op}} F_1| \tag{A.1b}$$

where α and γ_3 are defined in Equation 4.21 and Equation 4.17a, respectively.

To verify the mathematical estimations, a simulation is run using the equivalent electrical circuit model as shown in Figure 4.12. The values used for the simulation are listed in Table A.1. The motional current amplitudes were used in the simulations to represent the velocity amplitudes of each resonator.

The simulated vibration amplitudes of resonator 3 at the out-of-phase mode frequencies are plotted in Figure A.1. The theoretical values were calculated using Equation A.1b and compared to the simulated values. It can be seen from Figure A.1 that the theoretical

Table A.1: Values used in the simulation to verify theoretical estimations

Component	Value	Mechanical model equivalent
L	0.489 MH	M
C	0.254 fF	K
C_2	84.8 aF	$K_2/K = 3$
C_c	−19.07 fF	$K/K_c = -75$, $\gamma_3 = 11174$
R	0.88 MΩ	$Q = 50000$
v_{ac}	15 mV	Arbitrary actuation voltage

estimations agree well with the simulations, with relative errors less than 1.3% for all values.

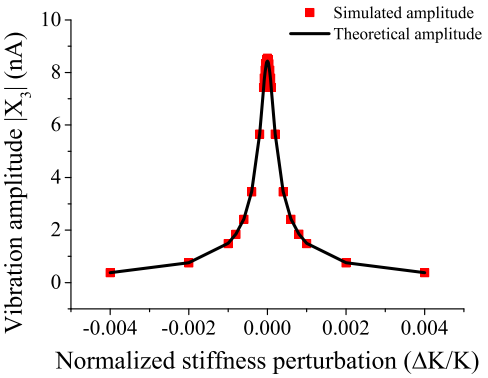

Figure A.1: Theoretical calculated vibration amplitudes of resonator 3 (black) and simulated vibration amplitudes by electrical equivalent model (red) as a function of normalized stiffness perturbations. The theoretical estimations match well with simulated values.

A.2 Vibration amplitude of resonator 1

Since the amplitude ratios are given by Equation 4.44, we are able to approximate the vibration amplitude of resonator 1, displacement amplitude X_1 and velocity amplitude U_1 as:

$$|X_1|_{\text{op}} \approx \left| \frac{\frac{\gamma_3(\Delta K/K) - \sqrt{\gamma_3^2(\Delta K/K)^2 + 4}}{2} + j\frac{\gamma_3}{Q}}{\frac{K}{Q}\left(-j\sqrt{\gamma_3^2(\Delta K/K)^2 + 4} - \frac{\gamma_3}{Q}\right)} \right| |F_1| \tag{A.2a}$$

$$|U_1|_{\text{op}} \approx \left| \frac{\frac{\gamma_3(\Delta K/K) - \sqrt{\gamma_3^2(\Delta K/K)^2 + 4}}{2} + j\frac{\gamma_3}{Q}}{\frac{K}{Q}\left(-j\sqrt{\gamma_3^2(\Delta K/K)^2 + 4} - \frac{\gamma_3}{Q}\right)} \right| |\omega_{\text{op}} F_1| \tag{A.2b}$$

To verify the mathematical expressions, the same simulation was run. The simulated results are plotted in Figure A.2, along with the theoretical estimations. The relative errors between the theoretical and simulated values is less than 2% for all stiffness perturbation values, indicating that the theoretical calculations can be regarded as accurate.

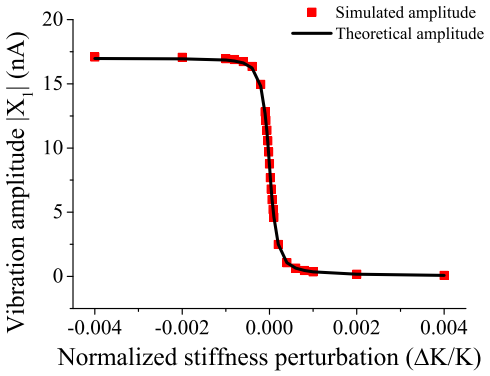

Figure A.2: Theoretical calculated vibration amplitudes of resonator 1 (black) and simulated vibration amplitudes by electrical equivalent model (red) as a function of normalized stiffness perturbations. The theoretical estimations match well with simulated values.

A.3 Vibration amplitude of resonator 2

In addition, the displacement and velocity amplitudes of resonator 2 can also be approximated at the out-of-phase mode frequency:

$$|X_2|_{\text{op}} \approx \left| \frac{\frac{\Delta K + \alpha - \sqrt{\Delta K^2 + \alpha^2}}{2K_c} - j\frac{K}{K_c Q}}{\frac{K}{Q}\left(-j\sqrt{\gamma_3^2(\Delta K/K)^2 + 4} - \frac{\gamma_3}{Q}\right)} \right| |F_1| \tag{A.3a}$$

$$|U_2|_{\text{op}} \approx \left| \frac{\frac{\Delta K + \alpha - \sqrt{\Delta K^2 + \alpha^2}}{2K_c} - j\frac{K}{K_c Q}}{\frac{K}{Q}\left(-j\sqrt{\gamma_3^2(\Delta K/K)^2 + 4} - \frac{\gamma_3}{Q}\right)} \right| |\omega_{\text{op}} F_1| \tag{A.3b}$$

The results from the same simulation as above are plotted alongside the theoretically calculated results in Figure A.3. It can be seen that the theoretical values are very close to the simulated errors, with typical relative errors less than 8%. However, the maximum relative error was approximately 8% when the simulated normalized stiffness perturbation was $\Delta K/K = 4 \times 10^{-3}$. The larger errors compared to the previous results was caused by the low values in the amplitude. This error was reduced to less than 1.5% when simulated with an AC driving voltage that was 10 times larger. Therefore, we are able to conclude that the theoretical estimations can be regarded accurate.

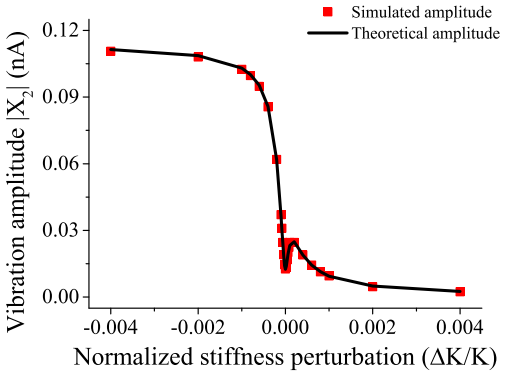

Figure A.3: Theoretical calculated vibration amplitudes of resonator 2 (black) and simulated vibration amplitudes by electrical equivalent model (red) as a function of normalized stiffness perturbations. The theoretical estimations match well with simulated values.

Appendix B

Phase Delays

B.1 Phase delay of resonator 3

We consider the resonator device example in Figure 5.1, driven by an AC voltage on the actuation electrode, and the driving force bing F_1. In addition, we suppose a stiffness perturbation $\Delta K < 0$ is applied to resonator 3. From Equations 4.38a to 4.38f, we are able to obtain the phase delays of resonators 1, 2 and 3.

Due to the symmetry of the in-phase mode and out-of-phase mode as shown in Figure 4.5, without loss of generality, only out-of-phase mode is discussed here. Assuming that the device is in the dynamic range, thus Equations 4.43 and 5.3 are satisfied, the frequency of the out-of-phase mode is given by Equation 4.20. Substituting Equation 4.20 into Equation 4.38f, we are able to approximate the phase delay of the displacement, X_3, and velocity, U_3, of resonator 3 at the out-of-phase mode, compared to the drive signal, respectively:

$$\angle |X_3|_{\text{op}} \approx -\arctan\left(\frac{-\sqrt{\gamma_3^2(\Delta K/K)^2+4}}{-\gamma_3/Q}\right) \tag{B.1a}$$

$$\angle |U_3|_{\text{op}} \approx -\arctan\left(\frac{-\sqrt{\gamma_3^2(\Delta K/K)^2+4}}{-\gamma_3/Q}\right) + 90^\circ \tag{B.1b}$$

The simulated phase delays of the motional current of the resonator 3 at the out-of-phase mode frequencies are plotted in Figure B.1. The theoretical values were calculated using Equation B.1b and compared to the simulated values. It can be seen from Figure B.1 that the theoretical estimations agree well with the simulations, with absolute errors less than 1.1° for all values.

Table B.1: Values used in the simulation to verify theoretical estimations

Component	Value	Mechanical model equivalent
L	0.489 MH	M
C	0.254 fF	K
C_2	84.8 aF	$K_2/K = 3$
C_c	−19.07 fF	$K/K_c = -75$, $\gamma_3 = 11174$
R	8.77 MΩ	$Q = 50000$
v_{ac}	15 mV	Arbitrary actuation voltage

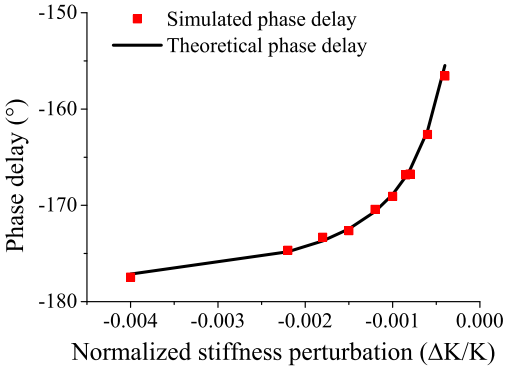

Figure B.1: Theoretical calculated phase delays of the resonator 3 motional current (black) and simulated values by electrical equivalent model (red) as a function of normalized stiffness perturbations. The theoretical estimations match well with simulated values.

B.2 Phase delay of resonator 1

We are also able to approximate the phase delays of the displacement of resonator 1, X_1 and velocity of resonator 1, U_1 as:

$$\begin{aligned}\angle|X_1|_{\text{op}} \approx \arctan&\left(\frac{2\gamma_3/Q}{\gamma_3(\Delta K/K) - \sqrt{\gamma_3^2(\Delta K/K)^2+4}}\right)\\ &-\arctan\left(\frac{-\sqrt{\gamma_3^2(\Delta K/K)^2+4}}{-\gamma_3/Q}\right)\end{aligned} \tag{B.2a}$$

$$\begin{aligned}\angle|U_1|_{\text{op}} \approx \arctan&\left(\frac{2\gamma_3/Q}{\gamma_3(\Delta K/K) - \sqrt{\gamma_3^2(\Delta K/K)^2+4}}\right)\\ &-\arctan\left(\frac{-\sqrt{\gamma_3^2(\Delta K/K)^2+4}}{-\gamma_3/Q}\right)+90^\circ\end{aligned} \tag{B.2b}$$

To verify the mathematical expressions, the same simulation was run. The simulated results are plotted in Figure B.2, along with the theoretical estimations. It can be seen

from Figure B.2 that the absolute differences between the simulated values and the theoretical values were smaller than 0.8°, which can be regarded as accurate.

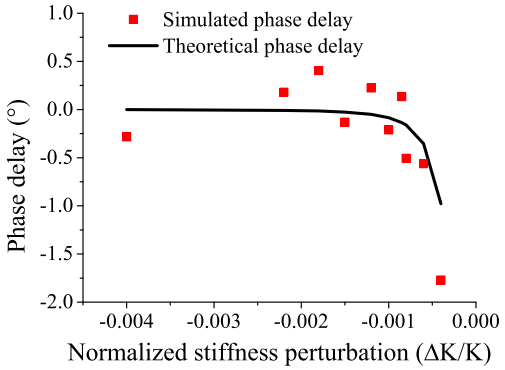

Figure B.2: Theoretical calculated phase delays of the resonator 1 motional current (black) and simulated values by electrical equivalent model (red) as a function of normalized stiffness perturbations. The theoretical estimations match well with simulated values.

It should be noticed that, when $\gamma_3(\Delta K/K) < -10$, the following can be approximated:

$$\gamma_3(\Delta K/K) - \sqrt{\gamma_3^2(\Delta K/K)^2 + 4} \approx -2\sqrt{\gamma_3^2(\Delta K/K)^2 + 4} \tag{B.3}$$

Therefore, for $\Delta K/K$ values that satisfies $\gamma_3(\Delta K/K) < -10$, Equation B.2b can be approximated to be 0°. Hence, the phase delay of the motional current of the resonator 1, is approximately in-phase with the drive signal. This conclusion is particularly important in designing the self-oscillating loop.

B.3 Phase delay of resonator 2

In addition, the displacement and velocity phase delays of the resonator 2 can also be approximated at the out-of-phase mode frequency:

$$\begin{aligned} \angle |X_2|_{\text{op}} \approx \arctan &\left(\frac{-2K/Q}{\Delta K + \alpha - \sqrt{\Delta K^2 + \alpha^2}} \right) \\ - \arctan &\left(\frac{-\sqrt{\gamma_3^2(\Delta K/K)^2 + 4}}{-\gamma_3/Q} \right) \end{aligned} \tag{B.4a}$$

$$\begin{aligned}\angle|U_2|_{\text{op}} \approx \arctan\left(\frac{-2K/Q}{\Delta K+\alpha-\sqrt{\Delta K^2+\alpha^2}}\right)\\ -\arctan\left(\frac{-\sqrt{\gamma_3^2(\Delta K/K)^2+4}}{-\gamma_3/Q}\right)+90^\circ\end{aligned} \tag{B.4b}$$

The results from the same simulation as above are plotted alongside the theoretically calculated results in Figure B.3. It can be seen that the theoretical values are very close to the simulated errors, with absolute errors less than 1.1° for all stiffness perturbations. Therefore, we are able to conclude that the theoretical estimations can be regarded accurate.

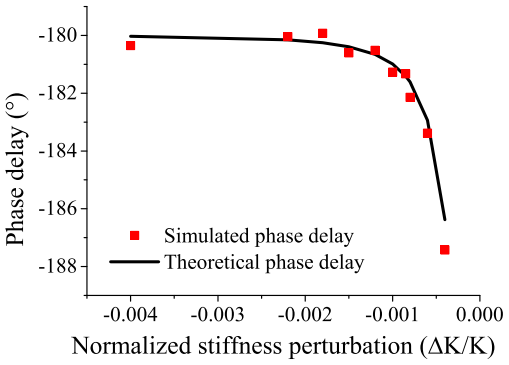

Figure B.3: Theoretical calculated phase delays of the resonator 2 motional current (black) and simulated values by electrical equivalent model (red) as a function of normalized stiffness perturbations. The theoretical estimations match well with simulated values.

Appendix C

Matlab Code for Solving Eigenvalues and Eigenstates

The following Matlab code is used to solve eigenvalues and eigenstates for 3DoF resonators with perturbations only to resonator 3. The values used in the code are the same as listed in Table 4.1. The Matlab code for the other cases can be easily derived from this code. Please note that this may not be the optimum code for this purpose.

```
% ------------------------------%
%       Matlab code
% ------------------------------%
k=57.6233;      % Stiffness of outer resonator
kc=-0.6904;     % Stiffness of coupling
km=199.5481;    % Stiffness of middle resonator
m=6.9351E-09;   % Masses of all resonators
dk=-0.17287:0.0069148:0.17287;  % Stiffness perturbations

for i=1:51
Dk=dk(i);  % Stiffness perturbation element
alpha=2*kc^2/(km-k+kc);   % Alpha value for calculating frequencies

% ------------------------------%
%  Matlab calculation of amplitude ratios and mode frequencies
% ------------------------------%
A=[k+kc,-kc,0;-kc,km+2*kc,-kc;0,-kc,k+kc+Dk]/m;
% Matrix define
[v,d]=eig(A); % Solving the eigenstates and eigenvalues
% v is the eigenstate, d is the eigenvalue
ratioinphase(i)=v(1,1)/v(3,1);  % In-phase mode amplitude ratio
ratiooutphase(i)=abs(v(1,2)/v(3,2));   % Out-of-phase mode amplitude ratio
finphase(i)=sqrt(d(1,1))/2/pi;  % In-phase mode frequency
foutphase(i)=sqrt(d(2,2))/2/pi;   % Out-of-phase mode frequency

% ------------------------------%
%  Theoretical estimations of amplitude ratios and mode frequencies
% ------------------------------%
theoreticaloutphase(i)
=abs(((km-k+kc)/(kc^2)*Dk-sqrt(((km-k+kc)/(kc^2))^2*(Dk^2)+4))/2);
% Theoretical out-of-phase mode amplitude ratio
```

```
theoreticalinphase(i)
=((km-k+kc)/(kc^2)*Dk+sqrt(((km-k+kc)/(kc^2))^2*(Dk^2)+4))/2;
% Theoretical in-phase mode amplitude ratio
fthoutphase(i)=sqrt([k+kc+1/2*(Dk-alpha+sqrt(Dk^2+alpha^2))]/m)/2/pi;
% Theoretical out-of-phase mode frequency
fthinphase(i)=sqrt([k+kc+1/2*(Dk-alpha-sqrt(Dk^2+alpha^2))]/m)/2/pi;
% Theoretical in-phase mode frequency

% ------------------------------%
%  Calculating the relative errors
% ------------------------------%
e1(i)=(theoreticaloutphase(i)-ratiooutphase(i))/ratiooutphase(i);
e2(i)=(theoreticalinphase(i)-ratioinphase(i))/ratioinphase(i);
e3(i)=(fthoutphase(i)-foutphase(i))/foutphase(i);
e4(i)=(fthinphase(i)-finphase(i))/finphase(i);

end
```

Appendix D

Construction Guide for Customized Vacuum Chamber

In this work, we have used a customized vacuum chamber to provide an ambient pressure as low as 20μTorr. This customized vacuum chamber has advantages such as low cost and portability. The following brief steps and Figure D.1 and Figure D.2 can be a guide on how to build a such vacuum chamber.

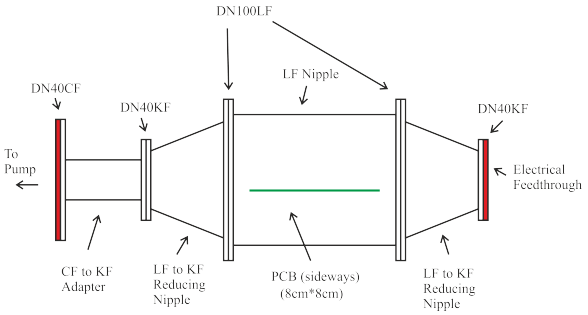

Figure D.1: Schematic drawing of the customized vacuum chamber.

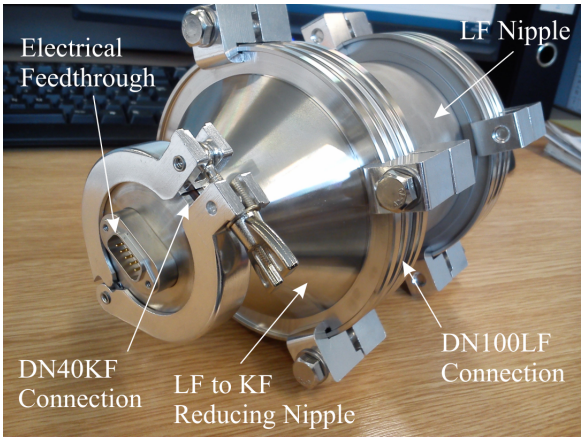

Figure D.2: Photo of the customized vacuum chamber.

First of all, the main body of the vacuum chamber should be big enough to hold the interface circuit board inside. In our case, the maximum size of the PCB board is 80mm $\times$ 80mm, therefore, a nipple with an ID of 100mm and a length of 100mm, as well as two LF-type of mechanical connection interface was used as the main body of the vacuum chamber.

After choosing the main body, the next task is to find out the number of I/O pins required for the PCB board. Then the part of the electrical feedthrough can be determined from the suppliers catalogue. In our case, a maximum number of 9 I/O pins were required. Hence we have chosen a 9-pin D-sub as the electrical feedthrough. We then found the cheapest part with the 9-pin D-sub connector. However, the diameter of the vacuum flange was 40mm, with a KF-type mechanical connection interface.

To connect the main body to the electrical feedthough, an adapter was needed because of different types of mechanical connection interface and different diameters. In our case, LF to KF reducing nipple was used.

As for the connection to the pump, two types of vacuum pump were used in our study, one with a 40cm diameter, KF-type of connection interface; and the other one with a 40cm diameter, CF-type of connection interface. Therefore, we implemented two adapters for each interface. To connect to the DN40KF pump, the LF to KF reducing nipple was used; to connect to the DN40CF pump, a further CF to KF adapter was used.

For the parts, we have used Lewvac (http://www.lewvac.co.uk/) as our supplier. More information of the parts can be found on the website.

Appendix E

Wire Bonding

The chips were wire bonded to a 28-pin J-lead ceramic chip carrier (JLCCC), and the bonding diagram is shown in Figure E.1. Since in our design, one single chip contains two devices, therefore the wire bonding diagram were split into two halves: the top and bottom halves. The top half represent devices without electrode for force sensing, whereas the bottom half shows the bonding diagram for a device with electrode for force sensing function, hence there was a slight difference in the bonding diagram.

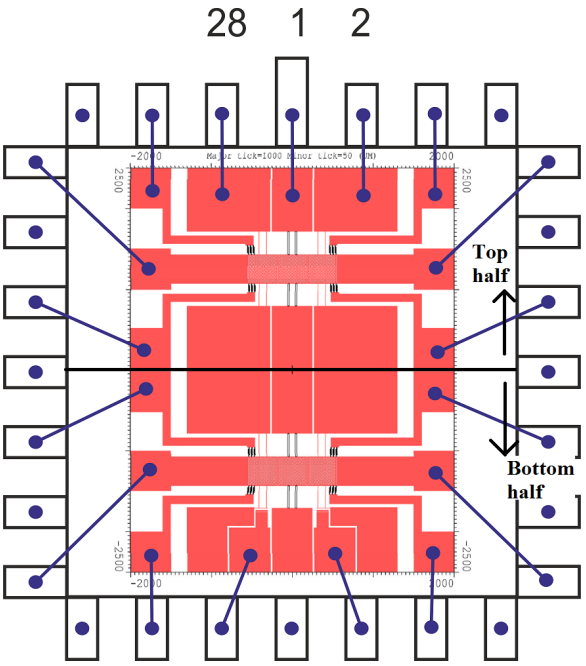

Figure E.1: Wire bonding diagram of a typical chip fabricated by Northeastern Polytechnical University (NPU), showing the bonding diagram of two different chip designs: top half without electrode for force sensing; bottom half with electrode for force sensing.

To illustrate this further, the electrical connections for two devices with or without electrode for force sensing are shown in Figure E.2. The electrical connections show

a typical configuration. However, thanks to the symmetry of the devices, the actual configuration can be mirrored.

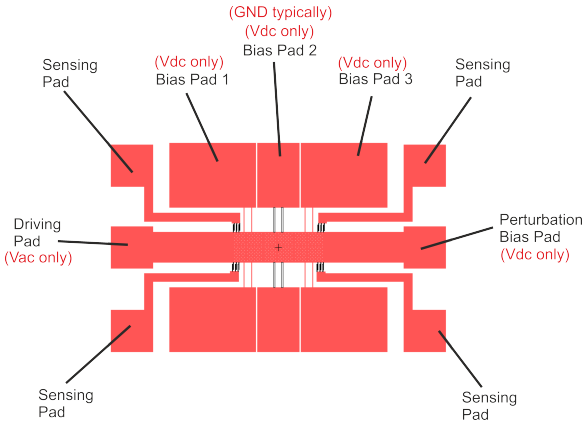

(a) Without electrode for force sensing

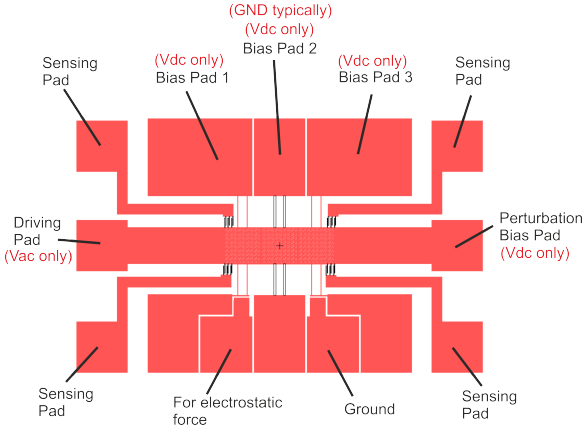

(b) With electrode for force sensing

Figure E.2: Diagrams of electrical connections of NPU devices: a) device without electrode for force sensing; b) device with electrode for force sensing.

References

[1] C. Zhao, G. S. Wood, S. H. Pu, and M. Kraft, "Design of an ultra-sensitive MEMS force sensor utilizing mode localization in weakly coupled resonators," in *23rd Micromechanics and Microsystems Europe Workshop*, 2012.

[2] C. Zhao, G. S. Wood, J. B. Xie, H. L. Chang, S. H. Pu, H. M. H. Chong, and M. Kraft, "A sensor for stiffness change sensing based on three weakly coupled resonators with enhanced sensitivity," in *Micro Electro Mechanical Systems, 2015. 28th IEEE International Conference on*, 2015.

[3] C. Zhao, G. S. Wood, J. B. Xie, H. L. Chang, S. H. Pu, and M. Kraft, "Comparative study of different output metrics for a three weakly coupled resonator sensor," in *Solid-State Sensors, Actuators and Microsystems, Transducers, 18th IEEE International Conference on*, 2015.

[4] C. Zhao, G. S. Wood, J. Xie, H. Chang, S. H. Pu, and M. Kraft, "A force sensor based on three weakly coupled resonators with ultrahigh sensitivity," *Sensors and Actuators A: Physical*, vol. 232, pp. 151–162, 2015.

[5] C. Zhao, G. S. Wood, S. H. Pu, and M. Kraft, "A feasibility study for a self-oscillating loop for a three degree-of-freedom coupled MEMS resonator force sensor," *Procedia Engineering*, vol. 120, pp. 887–891, 2015.

[6] C. Zhao, G. Wood, J. Xie, H. Chang, S. Pu, and M. Kraft, "A three degree-of-freedom weakly coupled resonator sensor with enhanced stiffness sensitivity," *Microelectromechanical Systems, Journal of*, vol. PP, no. 99, pp. 1–14, 2015.

[7] H. C. Nathanson, W. E. Newell, R. Wickstrom, and J. R. Davis Jr, "The resonant gate transistor," *Electron Devices, IEEE Transactions on*, vol. 14, no. 3, pp. 117–133, 1967.

[8] S. S. Li, Y. W. Lin, Y. Xie, Z. Ren, and C. Nguyen, "Micromechanical "hollow-disk" ring resonators," in *Micro Electro Mechanical Systems, 2004. 17th IEEE International Conference on.* IEEE, 2004.

[9] W. Hsu and C. Nguyen, "Stiffness-compensated temperature-insensitive micromechanical resonators," in *Micro Electro Mechanical Systems, 2002. 15th IEEE International Conference on.* IEEE, 2002.

[10] B. Kim, R. N. Candler, M. A. Hopcroft, M. Agarwal, W.-T. Park, and T. W. Kenny, "Frequency stability of wafer-scale film encapsulated silicon based MEMS resonators," *Sensors and Actuators A: Physical*, vol. 136, no. 1, pp. 125–131, 2007.

[11] K. Wang and C. Nguyen, "High-order medium frequency micromechanical electronic filters," *Microelectromechanical Systems, Journal of*, vol. 8, no. 4, pp. 534–556, 1999.

[12] K. Entesari and G. M. Rebeiz, "A 12–18GHz three-pole RF MEMS tunable filter," *Microwave Theory and Techniques, IEEE Transactions on*, vol. 53, no. 8, pp. 2566–2571, 2005.

[13] C. Nguyen, "MEMS technology for timing and frequency control," *Ultrasonics, Ferroelectrics and Frequency Control, IEEE Transactions on*, vol. 54, no. 2, pp. 251–270, 2007.

[14] M. A. Schmidt and R. T. Howe, "Silicon resonant microsensors," in *14th Automotive Materials Conference: Ceramic Engineering and Science Proceedings, Volume 8, Issue 9/10*. Wiley Online Library, 1987.

[15] H. Zhang and E. S. Kim, "Micromachined acoustic resonant mass sensor," *Microelectromechanical Systems, Journal of*, vol. 14, no. 4, pp. 699–706, 2005.

[16] M. Villarroya, J. Verd, J. Teva, G. Abadal, E. Forsen, F. P. Murano, A. Uranga, E. Figueras, J. Montserrat, and J. Esteve, "System on chip mass sensor based on polysilicon cantilevers arrays for multiple detection," *Sensors and Actuators A: Physical*, vol. 132, no. 1, pp. 154–164, 2006.

[17] T. P. Burg, A. R. Mirza, N. Milovic, C. H. Tsau, G. Popescu, J. S. Foster, and S. R. Manalis, "Vacuum-packaged suspended microchannel resonant mass sensor for biomolecular detection," *Microelectromechanical Systems, Journal of*, vol. 15, no. 6, pp. 1466–1476, 2006.

[18] T. Ikehara, J. Lu, M. Konno, R. Maeda, and T. Mihara, "A high quality-factor silicon cantilever for a low detection-limit resonant mass sensor operated in air," *Journal of Micromechanics and Microengineering*, vol. 17, no. 12, p. 2491, 2007.

[19] S. P. Beeby, G. Ensell, B. R. Baker, M. J. Tudor, and N. M. White, "Micromachined silicon resonant strain gauges fabricated using SOI wafer technology," *Microelectromechanical Systems, Journal of*, vol. 9, no. 1, pp. 104–111, 2000.

[20] K. E. Wojciechowski, B. E. Boser, and A. P. Pisano, "A MEMS resonant strain sensor operated in air," in *Micro Electro Mechanical Systems, 2004. 17th IEEE International Conference on.* IEEE, 2004.

[21] R. Azevedo, D. Jones, A. Jog, B. Jamshidi, D. Myers, L. Chen, X.-A. Fu, M. Mehregany, M. Wijesundara, and A. Pisano, "A SiC MEMS resonant strain

sensor for harsh environment applications," *Sensors Journal, IEEE*, vol. 7, no. 4, pp. 568–576, April 2007.

[22] E. Stemme and G. Stemme, "A balanced resonant pressure sensor," *Sensors and Actuators A: Physical*, vol. 21, no. 1, pp. 336–341, 1990.

[23] K. Petersen, F. Pourahmadi, J. Brown, P. Parsons, M. Skinner, and J. Tudor, "Resonant beam pressure sensor fabricated with silicon fusion bonding," in *Solid-State Sensors and Actuators, 1991 IEEE International Conference on*, 1991.

[24] C. J. Welham, J. W. Gardner, and J. Greenwood, "A laterally driven micromachined resonant pressure sensor," *Sensors and Actuators A: Physical*, vol. 52, no. 1, pp. 86–91, 1996.

[25] G. Binnig, C. F. Quate, and C. Gerber, "Atomic force microscope," *Physical Review Letters*, vol. 56, no. 9, p. 930, 1986.

[26] U. Dürig, J. Gimzewski, and D. Pohl, "Experimental observation of forces acting during scanning tunneling microscopy," *Physical Review Letters*, vol. 57, no. 19, p. 2403, 1986.

[27] T. Albrecht, P. Grütter, D. Horne, and D. Rugar, "Frequency modulation detection using high-Q cantilevers for enhanced force microscope sensitivity," *Journal of Applied Physics*, vol. 69, no. 2, pp. 668–673, 1991.

[28] R. Sunier, T. Vancura, Y. Li, K.-U. Kirstein, H. Baltes, and O. Brand, "Resonant magnetic field sensor with frequency output," *Microelectromechanical Systems, Journal of*, vol. 15, no. 5, pp. 1098–1107, Oct 2006.

[29] B. Bahreyni and C. Shafai, "A resonant micromachined magnetic field sensor," *Sensors Journal, IEEE*, vol. 7, no. 9, pp. 1326–1334, 2007.

[30] T. A. Roessig, R. T. Howe, A. P. Pisano, and J. H. Smith, "Surface-micromachined resonant accelerometer," in *Solid-State Sensors and Actuators, 1997 IEEE International Conference on*. IEEE, 1997.

[31] A. Seshia, M. Palaniapan, T. Roessig, R. T. Howe, R. W. Gooch, T. R. Schimert, S. Montague *et al.*, "A vacuum packaged surface micromachined resonant accelerometer," *Microelectromechanical Systems, Journal of*, vol. 11, no. 6, pp. 784–793, 2002.

[32] A. N. Cleland and M. L. Roukes, "A nanometre-scale mechanical electrometer," *Nature*, vol. 392, no. 6672, pp. 160–162, 1998.

[33] Y. Zhu, J. E. Lee, A. Seshia *et al.*, "A resonant micromachined electrostatic charge sensor," *Sensors Journal, IEEE*, vol. 8, no. 9, pp. 1499–1505, 2008.

[34] P. Thiruvenkatanathan, "Mode-localized sensing in micromechanical resonator arrays," Ph.D. dissertation, University of Cambridge, 2010.

[35] C. T. Nguyen, "Frequency-selective MEMS for miniaturized low-power communication devices," *Microwave Theory and Techniques, IEEE Transactions on*, vol. 47, no. 8, pp. 1486–1503, 1999.

[36] M. Spletzer, A. Raman, A. Q. Wu, X. Xu, and R. Reifenberger, "Ultrasensitive mass sensing using mode localization in coupled microcantilevers," *Applied Physics Letters*, vol. 88, no. 25, p. 254102, 2006.

[37] N. H. Saad, C. J. Anthony, R. Al-Dadah, and M. C. Ward, "Exploitation of multiple sensor arrays in electronic nose," in *Sensors, 2009 IEEE Conference on*. IEEE, 2009.

[38] E. Gil-Santos, D. Ramos, A. Jana, M. Calleja, A. Raman, and J. Tamayo, "Mass sensing based on deterministic and stochastic responses of elastically coupled nanocantilevers," *Nano Letters*, vol. 9, no. 12, pp. 4122–4127, 2009.

[39] P. Thiruvenkatanathan, J. Yan, J. Woodhouse, and A. Seshia, "Enhancing parametric sensitivity in electrically coupled MEMS resonators," *Microelectromechanical Systems, Journal of*, vol. 18, no. 5, pp. 1077–1086, 2009.

[40] R. Tabrizian and F. Ayazi, "Dual-mode vertical membrane resonant pressure sensor," in *Micro Electro Mechanical Systems, 2014. 27th IEEE International Conference on*. IEEE, 2014.

[41] P. Thiruvenkatanathan, J. Yan, and A. Seshia, "Common mode rejection in electrically coupled mems resonators utilizing mode localization for sensor applications," in *Frequency Control Symposium, 2009 Joint with the 22nd European Frequency and Time forum. IEEE International*. IEEE, 2009.

[42] P. W. Anderson, "Absence of diffusion in certain random lattices," *Physical Review*, vol. 109, no. 5, p. 1492, 1958.

[43] M. Spletzer, A. Raman, H. Sumali, and J. P. Sullivan, "Highly sensitive mass detection and identification using vibration localization in coupled microcantilever arrays," *Applied Physics Letters*, vol. 92, no. 11, p. 114102, 2008.

[44] Y. Martin, C. Williams, and H. K. Wickramasinghe, "Atomic force microscope–force mapping and profiling on a sub 100-Å scale," *Journal of Applied Physics*, vol. 61, no. 10, pp. 4723–4729, 1987.

[45] K. Y. Yasumura, T. D. Stowe, E. M. Chow, T. Pfafman, T. W. Kenny, B. C. Stipe, and D. Rugar, "Quality factors in micron-and submicron-thick cantilevers," *Microelectromechanical Systems, Journal of*, vol. 9, no. 1, pp. 117–125, 2000.

[46] G. Stemme, "Resonant silicon sensors," *Journal of Micromechanics and Microengineering*, vol. 1, no. 2, p. 113, 1991.

[47] J. Lee, B. Bahreyni, Y. Zhu, and A. Seshia, "Ultrasensitive mass balance based on a bulk acoustic mode single-crystal silicon resonator," *Applied Physics Letters*, vol. 91, no. 23, p. 234103, 2007.

[48] J. Yan, A. Seshia, K. L. Phan, P. G. Steeneken, and J. T. van Beek, "Narrow bandwidth single-resonator mems tuning fork filter," in *Frequency Control Symposium, 2007 Joint with the 21st European Frequency and Time Forum. IEEE International*. IEEE, 2007.

[49] F. J. Giessibl, S. Hembacher, H. Bielefeldt, and J. Mannhart, "Subatomic features on the silicon (111)-(7× 7) surface observed by atomic force microscopy," *Science*, vol. 289, no. 5478, pp. 422–425, 2000.

[50] K. Jensen, K. Kim, and A. Zettl, "An atomic-resolution nanomechanical mass sensor," *Nature Nanotechnology*, vol. 3, no. 9, pp. 533–537, 2008.

[51] J. Harley and T. W. Kenny, "A high-stiffness axial resonant probe for atomic force microscopy," *Microelectromechanical Systems, Journal of*, vol. 10, no. 3, pp. 434–441, 2001.

[52] B. Terris, J. Stern, D. Rugar, and H. Mamin, "Contact electrification using force microscopy," *Physical Review Letters*, vol. 63, no. 24, p. 2669, 1989.

[53] D. Rugar, H. Mamin, P. Guethner, S. Lambert, J. Stern, I. McFadyen, and T. Yogi, "Magnetic force microscopy: General principles and application to longitudinal recording media," *Journal of Applied Physics*, vol. 68, no. 3, pp. 1169–1183, 1990.

[54] R. McKendry, J. Zhang, Y. Arntz, T. Strunz, M. Hegner, H. P. Lang, M. K. Baller, U. Certa, E. Meyer, and H.-J. Güntherodt, "Multiple label-free biodetection and quantitative dna-binding assays on a nanomechanical cantilever array," *Proceedings of the National Academy of Sciences*, vol. 99, no. 15, pp. 9783–9788, 2002.

[55] H. P. Lang, M. Hegner, and C. Gerber, "Cantilever array sensors," *Materials Today*, vol. 8, no. 4, pp. 30–36, 2005.

[56] B. Choubey, C. Anthony, N. H. Saad, M. Ward, R. Turnbull, and S. Collins, "Characterization of coupled micro/nanoresonators using inverse eigenvalue analysis," *Applied Physics Letters*, vol. 97, no. 13, p. 133114, 2010.

[57] B. E. DeMartini, J. F. Rhoads, M. A. Zielke, K. G. Owen, S. W. Shaw, and K. L. Turner, "A single input-single output coupled microresonator array for the detection and identification of multiple analytes," *Applied Physics Letters*, vol. 93, no. 5, p. 054102, 2008.

[58] M. S. Hajhashemi and B. Bahreyni, "Characterization of disturbances in systems of coupled micro-resonator arrays," *Sensors Journal, IEEE*, vol. 12, no. 7, pp. 2510–2516, 2012.

[59] J. Fritz, M. Baller, H. Lang, H. Rothuizen, P. Vettiger, E. Meyer, H.-J. Güntherodt, C. Gerber, and J. Gimzewski, "Translating biomolecular recognition into nanomechanics," *Science*, vol. 288, no. 5464, pp. 316–318, 2000.

[60] F. Golnaraghi and B. C. Kuo, *Automatic control systems*, 9th ed. John Wiley & Sons, 2010.

[61] F. J. Giessibl, "A direct method to calculate tip–sample forces from frequency shifts in frequency-modulation atomic force microscopy," *Applied Physics Letters*, vol. 78, no. 1, pp. 123–125, 2001.

[62] C. Pierre, "Mode localization and eigenvalue loci veering phenomena in disordered structures," *Journal of Sound and Vibration*, vol. 126, no. 3, pp. 485–502, 1988.

[63] S. Pourkamali and F. Ayazi, "Electrically coupled MEMS bandpass filters: Part II. without coupling element," *Sensors and Actuators A: Physical*, vol. 122, no. 2, pp. 317–325, 2005.

[64] P. Thiruvenkatanathan, J. Woodhouse, J. Yan, and A. A. Seshia, "Limits to mode-localized sensing using micro- and nanomechanical resonator arrays," *Journal of Applied Physics*, vol. 109, no. 10, pp. 1 – 11, 2011.

[65] K. Tanaka, Y. Mochida, M. Sugimoto, K. Moriya, T. Hasegawa, K. Atsuchi, and K. Ohwada, "A micromachined vibrating gyroscope," *Sensors and Actuators A: Physical*, vol. 50, no. 1, pp. 111–115, 1995.

[66] Y. Oh, B. Lee, S. Baek, H. Kim, J. Kim, S. Kang, and C. Song, "A surface-micromachined tunable vibratory gyroscope," in *Micro Electro Mechanical Systems, 1997. 10th IEEE Annual International Workshop on.* IEEE, 1997.

[67] X. Jiang, J. I. Seeger, M. Kraft, and B. E. Boser, "A monolithic surface micromachined z-axis gyroscope with digital output," in *VLSI Circuits, 2000. Digest of Technical Papers. 2000 Symposium on.* IEEE, 2000.

[68] A. A. Seshia, R. T. Howe, and S. Montague, "An integrated microelectromechanical resonant output gyroscope," in *Micro Electro Mechanical Systems, 2002. 15th IEEE International Conference on.* IEEE, 2002.

[69] A. Sharma, M. F. Zaman, and F. Ayazi, "A 104-dB dynamic range transimpedance-based CMOS ASIC for tuning fork microgyroscopes," *Solid-State Circuits, IEEE Journal of*, vol. 42, no. 8, pp. 1790–1802, 2007.

[70] W. Pang, L. Yan, H. Zhang, H. Yu, E. S. Kim, and W. C. Tang, "Femtogram mass sensing platform based on lateral extensional mode piezoelectric resonator," *Applied Physics Letters*, vol. 88, no. 24, p. 243503, 2006.

[71] B. Walter, M. Faucher, E. Algré, B. Legrand, R. Boisgard, J.-P. Aimé, and L. Buchaillot, "Design and operation of a silicon ring resonator for force sensing applications above 1MHz," *Journal of Micromechanics and Microengineering*, vol. 19, no. 11, p. 115009, 2009.

[72] M. Suter, O. Ergeneman, J. Zürcher, S. Schmid, A. Camenzind, B. Nelson, and C. Hierold, "Superparamagnetic photocurable nanocomposite for the fabrication of microcantilevers," *Journal of Micromechanics and Microengineering*, vol. 21, no. 2, p. 025023, 2011.

[73] S. Dohn, R. Sandberg, W. Svendsen, and A. Boisen, "Enhanced functionality of cantilever based mass sensors using higher modes," *Applied Physics Letters*, vol. 86, no. 23, p. 233501, 2005.

[74] J. Verd, A. Uranga, G. Abadal, J. Teva, F. Torres, F. Perez-Murano, J. Fraxedas, J. Esteve, and N. Barniol, "Monolithic mass sensor fabricated using a conventional technology with attogram resolution in air conditions," *Applied Physics Letters*, vol. 91, no. 1, pp. 013 501–013 501, 2007.

[75] T. Lalinskỳ, E. Burian, M. Drzik, S. Hascík, Z. Mozolová, and J. Kuzmík, "Thermal actuation of a GaAs cantilever beam," *Journal of Micromechanics and Microengineering*, vol. 10, no. 2, p. 293, 2000.

[76] S. Minne, S. Manalis, and C. Quate, "Parallel atomic force microscopy using cantilevers with integrated piezoresistive sensors and integrated piezoelectric actuators," *Applied Physics Letters*, vol. 67, no. 26, pp. 3918–3920, 1995.

[77] A. Uranga, J. Verd, J. Lopez, J. Teva, G. Abadal, F. Torres, J. Esteve, F. Perez-Murano, and N. Barniol, "Fully integrated MIXLER based on VHF CMOS-MEMS clamped-clamped beam resonator," *Electronics Letters*, vol. 43, no. 8, pp. 452–454, 2007.

[78] J. E.-Y. Lee, B. Bahreyni, and A. A. Seshia, "An axial strain modulated double-ended tuning fork electrometer," *Sensors and Actuators A: Physical*, vol. 148, no. 2, pp. 395–400, 2008.

[79] A. Stalder and U. Dürig, "Nanoguitar: oscillating string as force sensor," *Review of Scientific Instruments*, vol. 66, no. 6, pp. 3576–3579, 1995.

[80] J. Wang, D. Chen, L. Liu, and Z. Wu, "A micromachined resonant pressure sensor with DETFs resonator and differential structure," in *Sensors, 2009 IEEE Conference on*. IEEE, 2009.

[81] C. T.-C. Nguyen and R. T. Howe, "An integrated CMOS micromechanical resonator high-Q oscillator," *Solid-State Circuits, IEEE Journal of*, vol. 34, no. 4, pp. 440–455, 1999.

[82] V. Kaajakari, *Practical MEMS*, 1st ed. Small Gear Publishing, Las Vegas, NV, 2009.

[83] G. Piazza, P. J. Stephanou, and A. P. Pisano, "Single-chip multiple-frequency ALN MEMS filters based on contour-mode piezoelectric resonators," *Microelectromechanical Systems, Journal of*, vol. 16, no. 2, pp. 319–328, 2007.

[84] R. Hickey, D. Sameoto, T. Hubbard, and M. Kujath, "Time and frequency response of two-arm micromachined thermal actuators," *Journal of Micromechanics and Microengineering*, vol. 13, no. 1, p. 40, 2003.

[85] J. I. Seeger and B. E. Boser, "Charge control of parallel-plate, electrostatic actuators and the tip-in instability," *Microelectromechanical Systems, Journal of*, vol. 12, no. 5, pp. 656–671, 2003.

[86] C. J. Welham, J. W. Gardner, and J. Greenwood, "A laterally driven micromachined resonant pressure sensor," *Sensors and Actuators A: Physical*, vol. 52, no. 1, pp. 86–91, 1996.

[87] J. D. Grade, H. Jerman, and T. W. Kenny, "Design of large deflection electrostatic actuators," *Microelectromechanical Systems, Journal of*, vol. 12, no. 3, pp. 335–343, 2003.

[88] B. Puers, E. Peeters, A. Van Den Bossche, and W. Sansen, "A capacitive pressure sensor with low impedance output and active suppression of parasitic effects," *Sensors and Actuators A: Physical*, vol. 21, no. 1, pp. 108–114, 1990.

[89] F. J. Giessibl, "Forces and frequency shifts in atomic-resolution dynamic-force microscopy," *Physical Review B*, vol. 56, no. 24, p. 16010, 1997.

[90] S. Pamidighantam, R. Puers, K. Baert, and H. A. Tilmans, "Pull-in voltage analysis of electrostatically actuated beam structures with fixed–fixed and fixed–free end conditions," *Journal of Micromechanics and Microengineering*, vol. 12, no. 4, p. 458, 2002.

[91] V. Kaajakari, T. Mattila, A. Oja, and H. Seppa, "Nonlinear limits for single-crystal silicon microresonators," *Microelectromechanical Systems, Journal of*, vol. 13, no. 5, pp. 715–724, 2004.

[92] K. Tanaka, R. Kihara, A. Sánchez-Amores, J. Montserrat, and J. Esteve, "Parasitic effect on silicon mems resonator model parameters," *Microelectronic Engineering*, vol. 84, no. 5, pp. 1363–1368, 2007.

[93] R. W. Carpick and M. Salmeron, "Scratching the surface: fundamental investigations of tribology with atomic force microscopy," *Chemical Reviews*, vol. 97, no. 4, pp. 1163–1194, 1997.

[94] A. DiCarlo, M. Scheinfein, and R. Chamberlin, "Magnetic force microscope utilizing an ultra-small-spring-constant vertically cantilevered tip," *Ultramicroscopy*, vol. 47, no. 4, pp. 383–392, 1992.

[95] T. Stowe, K. Yasumura, T. Kenny, D. Botkin, K. Wago, and D. Rugar, "Attonewton force detection using ultrathin silicon cantilevers," *Applied Physics Letters*, vol. 71, pp. 288–290, 1997.

[96] A. Tocchio, C. Comi, G. Langfelder, A. Corigliano, and A. Longoni, "Enhancing the linear range of MEMS resonators for sensing applications," *Sensors Journal, IEEE*, vol. 11, no. 12, pp. 3202–3210, 2011.

[97] J. F. Rhoads, S. W. Shaw, and K. L. Turner, "The nonlinear response of resonant microbeam systems with purely-parametric electrostatic actuation," *Journal of Micromechanics and Microengineering*, vol. 16, no. 5, p. 890, 2006.

[98] J. Lee and A. Seshia, "Parasitic feedthrough cancellation techniques for enhanced electrical characterization of electrostatic microresonators," *Sensors and Actuators A: Physical*, vol. 156, no. 1, pp. 36–42, 2009.

[99] B. P. Otis and J. M. Rabaey, "A 300μW 1.9GHz CMOS oscillator utilizing micromachined resonators," *Solid-State Circuits, IEEE Journal of*, vol. 38, no. 7, pp. 1271–1274, 2003.

[100] K. Wojciechowski, R. Olsson, M. Tuck, E. Roherty-Osmun, and T. Hill, "Single-chip precision oscillators based on multi-frequency, high-q aluminum nitride mems resonators," in *Solid-State Sensors, Actuators and Microsystems, Transducers, 15th IEEE International Conference on*. IEEE, 2009.

[101] T. Wang and B. Erhman, "Compensate transimpedance amplifiers intuitively," in *Texas Instruments application report SBOA055A*, 2005.

[102] A. A. Seshia, "Integrated micromechanical resonant sensors for inertial measurement systems," Ph.D. dissertation, University of California, Berkeley, 2002.

[103] L. Meirovitch, *Fundamentals of vibrations*. McGraw-Hill Higher Education, 2001.

[104] T. A. W. Roessig, "Integrated MEMS tuning fork oscillations for sensor applications," Ph.D. dissertation, University of California, Berkeley, 1998.

[105] S. Timoshenko, *Vibration problems in engineering*, 4th ed. Wiley, New York, 1974.

[106] T. Mattila, J. Kiihamäki, T. Lamminmäki, O. Jaakkola, P. Rantakari, A. Oja, H. Seppä, H. Kattelus, and I. Tittonen, "A 12MHz micromechanical bulk acoustic mode oscillator," *Sensors and Actuators A: Physical*, vol. 101, no. 1, pp. 1–9, 2002.

[107] E. P. Quévy, S. A. Bhave, H. Takeuchi, T.-J. King, and R. T. Howe, "Poly-SiGe high frequency resonators based on lithographic definition of nano-gap lateral transducers," in *Hilton Head Workshop*, 2004.

[108] M. Manav, G. Reynen, M. Sharma, E. Cretu, and A. Phani, "Ultrasensitive resonant mems transducers with tuneable coupling," *Journal of Micromechanics and Microengineering*, vol. 24, no. 5, p. 055005, 2014.

[109] M. Bao, H. Yang, H. Yin, and S. Shen, "Effects of electrostatic forces generated by the driving signal on capacitive sensing devices," *Sensors and Actuators A: Physical*, vol. 84, no. 3, pp. 213–219, 2000.

[110] O. Katsuhiko, *Modern control engineering*, 5th ed. Pearson, 2010.

[111] S. J. Mason, "Feedback theory-some properties of signal flow graphs," *Proceedings of the IRE*, vol. 41, no. 9, pp. 1144–1156, 1953.

[112] K. Wang and C. T. Nguyen, "High-order micromechanical electronic filters," in *Micro Electro Mechanical Systems, 1997. 10th IEEE Annual International Workshop on*. IEEE, 1997.

[113] R. C. Elandt-Johnson, *Survival models and data analysis*. John Wiley & Sons, 1980, vol. 110.

[114] T. B. Gabrielson, "Mechanical-thermal noise in micromachined acoustic and vibration sensors," *Electron Devices, IEEE Transactions on*, vol. 40, no. 5, pp. 903–909, 1993.

[115] P. R. Saulson, "Thermal noise in mechanical experiments," *Physical Review D*, vol. 42, no. 8, p. 2437, 1990.

[116] J. B. Xie, Y. C. Hao, H. L. Chang, and W. Z. Yuan, "Single mask selective release process for complex SOI MEMS device," *Key Engineering Materials*, vol. 562, pp. 1116–1121, 2013.

[117] P. T. Docker, P. Kinnell, and M. C. Ward, "A dry single-step process for the manufacture of released MEMS structures," *Journal of Micromechanics and Microengineering*, vol. 13, no. 5, p. 790, 2003.

[118] L. Haobing and F. Chollet, "Layout controlled one-step dry etch and release of MEMS using deep RIE on SOI wafer," *Microelectromechanical Systems, Journal of*, vol. 15, no. 3, pp. 541–547, June 2006.

[119] I. Sari, I. Zeimpekis, and M. Kraft, "A dicing free SOI process for MEMS devices," *Microelectronic Engineering*, vol. 95, pp. 121–129, 2012.

[120] O. Raccurt, F. Tardif, F. A. d'Avitaya, and T. Vareine, "Influence of liquid surface tension on stiction of SOI MEMS," *Journal of Micromechanics and Microengineering*, vol. 14, no. 7, p. 1083, 2004.

[121] P. Thiruvenkatanathan, J. Yan, and A. A. Seshia, "Ultrasensitive Mode-Localized Micromechanical Electrometer," *Frequency Control Symposium (FCS), 2010 IEEE International*, vol. 9, 2010.

[122] S. Sung, J. G. Lee, B. Lee, and T. Kang, "Design and performance test of an oscillation loop for a mems resonant accelerometer," *Journal of Micromechanics and Microengineering*, vol. 13, no. 2, p. 246, 2003.

[123] X. Feng, C. White, A. Hajimiri, and M. L. Roukes, "A self-sustaining ultrahigh-frequency nanoelectromechanical oscillator," *Nature Nanotechnology*, vol. 3, no. 6, pp. 342–346, 2008.

[124] T. K. Tang, R. C. Gutierrez, C. B. Stell, V. Vorperian, G. A. Arakaki, J. T. Rice, W. J. Li, I. Chakraborty, K. Shcheglov, and J. Z. Wilcox, "A packaged silicon MEMS vibratory gyroscope for microspacecraft," in *Micro Electro Mechanical Systems, 1997. 10th IEEE Annual International Workshop on.* IEEE, 1997.

[125] F. He, R. Ribas, C. Lahuec, and M. Jézéquel, "Discussion on the general oscillation startup condition and the barkhausen criterion," *Analog Integrated Circuits and Signal Processing*, vol. 59, no. 2, pp. 215–221, 2009.

[126] L. He, Y. P. Xu, and M. Palaniapan, "A CMOS readout circuit for SOI resonant accelerometer with 4μg bias stability and 20$\mu g/\sqrt{Hz}$ resolution," *Solid-State Circuits, IEEE Journal of*, vol. 43, no. 6, pp. 1480–1490, 2008.

[127] S. A. Bhave, D. Gao, R. Maboudian, and R. T. Howe, "Fully-differential poly-sic lame mode resonator and checkerboard filter," in *Micro Electro Mechanical Systems, 2005. 18th IEEE International Conference on.* IEEE, 2005.